UNIVERSITÀ
DEGLI STUDI
FIRENZE

DOTTORATO DI RICERCA IN
Scienze della Terra

CICLO XXVI

COORDINATORE Prof. Lorenzo Rook

Crystal chemistry of phlogopites from ultrapotassic rocks with lamproitic affinity from the Western Mediterranean Region.

Settore Scientifico Disciplinare GEO/06

Dottorando
Dott. Giovanni Orazio Lepore

_____

Tutore
Prof.ssa Paola Bonazzi

_____

Coordinatore
Prof. Lorenzo Rook

_____

Anni 2011/2014

Table of Contents

1 Introduction

1.1 Micas in lamproites

Trioctahedral micas belonging to the phlogopite-annite join are common rock-forming minerals in a wide range of petrogenic conditions; their importance as petrogenetic indicators is widely accepted and many works have shown the existing correlation of crystal-chemical features of these phases with their crystallization conditions (e.g., Brigatti et al., 1996b, 2000a and 2000b; Benincasa et al., 2003; Lacalamita et al., 2011; Schingaro et al., 2014).

In order to asses this kind of information, a deep knowledge of the structural details and their variation as a function of the physicochemical variables of the genetic system is crucial. Phlogopite is important for the understanding of the genesis of alkaline magmas that produce the existing wide spectrum of ultrapotassic rocks (e.g., Edgar and Arima, 1983; Trønnes et al., 1985, Foley, 1989, 1990; Mitchell and Bergman, 1991; Conticelli et al., 1992; Edgar et al., 1992; Conticelli, 1998; Fritschle et al., 2013). Few studies of comparative crystal-chemical characterization of micas from alkaline and carbonatitic rocks are available. They report data of brown micas from ultramafic alkaline rocks belonging to carbonatite-bearing complexes (e.g., Brigatti et al., 1996b, 2001; Schingaro et al., 2011), from within-plate kamafugitic igneous rocks (e.g., Lacalamita et al., 2012; Scordari et al., 2012a), from Na to K alkaline rocks (e.g., Schingaro et al., 2001; Scordari et al., 2006, 2008, 2010; Lacalamita et al., 2011), from leucite-bearing ultrapotassic rocks (e.g., Brigatti et al., 2005; Laurora et al., 2009), and from Mica-Rich Enclaves (MRE) in silicic rocks (e.g. Laurora et al., 2007). Among ultrapotassic rocks only few studies concerning the crystal chemistry of phlogopite from lamproite-like rocks are available (Brigatti et al. 1991; Brigatti and Poppi, 1993; Cruciani and Zanazzi, 1994; Babushkina et al., 2011; Schingaro et al., 2014).

Lamproites are an important group of Al- and Ca-poor ultrapotassic rocks derived by partial melting of metasomatised lithopspheric upper mantle (e.g., Foley et al., 1987; Foley and Venturelli, 1989; Mitchell and Bergman, 1991; Conticelli et al., 1992, 2007, 2009; Peccerillo, 1999; Peccerillo and Martinotti, 2006; Prelević and Foley, 2007). Lamproitic magmas have been generated in a wide spectrum of tectonic settings from within-plate to destructive plate margins (e.g., Peccerillo et al., 1988; Conticelli and Peccerillo, 1992; Conticelli, 1998; Murphy et al., 2002; Davies et al., 2006; Guo et al., 2006, 2013, 2014; Owen, 2008; Tommasini et al., 2011).

Micas crystallized from lamproitic magmas exhibit a phlogopitic composition, with significant contents of annite component and large but variable amounts of titanium, barium

and fluorine. Together with olivine, clinopyroxene and sanidine, phlogopite is ubiquitously present in lamproites, and its presence could even be a prerequisite for the generation of ultrapotassic melts (Jaques et al., 1986; Foley, 1993; Sato, 1997). Thus, phlogopite could provide information on the early fractionation history of ultrapotassic rocks. These phases are indeed characterized by a remarkable chemical complexity and, in order to understand the processes involved in their formation, the role played by each substitutional mechanism should be deeply examined.

An accurate knowledge of cation and anion populations of natural phlogopite represents a challenge given the difficulty to obtain reliable and complete data. In the last years, the availability of modern techniques to obtain chemical data, especially the quantification of H by secondary ion mass spectrometry (SIMS) and the determination of $Fe^{3+}/\Sigma Fe$ by Mössbauer spectroscopy, allowed, in many cases, a complete determination of the chemical composition of these minerals. This advance gave the possibility to note that phlogopite is often characterized by marked H deficiencies, which correlate with octahedral cations such as Fe^{3+}, Cr, Ti, and Al (e.g., Virgo and Popp, 2000; Sassi et al., 2008; Ottolini et al., 2010; Scordari et al., 2010). To shed light on the complex crystal-chemical mechanisms occurring in these minerals, however, a knowledge of the structural details is essential (e.g., Cesare et al., 2003, 2008; Brigatti et al., 2005; Scordari et al., 2006; Schingaro et al., 2007; Matarrese et al., 2008; Sassi et al., 2008; Lacalamita, 2009). Therefore a detailed structural analysis is crucial, along with the chemical characterization, to evaluate the extensive chemical disorder that affects the cation sites of micas, because homo- and hetero-valent substitutions occur at interlayer (K, Ba, Ca, Na, NH_4^+, H_2O, H_3O^+, , where stands for vacancy), octahedral (Mg, Mn, Fe^{2+}, Fe^{3+}, $Ti^{3+,4+}$, Al, Cr, Li,), and tetrahedral (Si, Al, Fe^{3+}, Ti^{4+}) sites. Tri- and tetra-valent cations can indeed be incorporated in trioctahedral micas via multiple substitution schemes as well as through a combination of these: the most common and studied processes affecting the chemistry of both octahedral and tetrahedral sites are $M^{3,4+}$-Tschermak's substitutions, i.e., the Al, Fe^{3+}-Tschermak, and the Ti-Tschermak (Robert, 1976; Dymek, 1983; Abrecht and Hewitt, 1988; Waters and Charnley, 2002; Cesare et al., 2003; Mesto et al., 2006; Scordari et al., 2006, 2008; Matarrese et al., 2008); those affecting only the chemistry of the octahedral sites are Ti-vacancy substitutions or trivalent cation-vacancy; those involving octahedral and anion sites are *oxy*-type, i.e., the Ti-*oxy* and the Al-, Fe^{3+}-*oxy* substitution (Dyar et al. 1993; Feldstein et al., 1996; Righter et al. 2002; Schingaro et al., 2005, 2007; Scordari et al., 2006, 2008, 2010; Matarrese et al., 2008; Ventruti et al., 2008). The tetrahedral site may also be affected by Fe^{3+} for Al^{3+} substitution, known as the

tetraferriphlogopite substitution (Rancourt et al., 1992; Cruciani et al., 1995; Brigatti et al., 1996a, 1996b, 2001).

The aim of this study is to investigate the crystal chemistry of phlogopite from lamproites of the western Mediterranean area by means of single-crystal X-ray diffraction (SCXRD), electron microprobe analysis (EMPA), Secondary Ion Mass Spectrometry (SIMS) and, when feasible, Mössbauer spectroscopy (MS). Specifically, rock samples from three magmatic provinces were collected and analyzed: Western Alps (Northwestern Italy), Corsica (France), and Central Italy (Southern Tuscany and Northern Latium). Moreover, this work presents the results of an investigation carried out on two new micas from Cerchiara mine and characterized by very peculiar chemical compositions. Details on the provenance of the studied material, as well as experimental methods and results are reported in chapter 5.

1.2 Geological background

Lamproites are mafic to intermediate ultrapotassic rocks of mantle origin characterized by variable silica contents which may reach intermediate to high silica values in high-MgO rocks at equilibrium conditions with their mantle source (e.g., Foley and Venturelli, 1989; Foley, 1992, 1994; Conticelli, 1998). The strong enrichment in K is thought to be a primary mantle characteristic related with metasomatic enrichment due to either deep sub-continental mantle degassing or to recycling of sediments during continental collision after oceanic crust complete consumption (e.g., Peccerillo, 1985; Conticelli and Peccerillo, 1992; Murphy et al., 2002; Davies et al., 2006; Mirnejad and Bell, 2006; Conticelli et al. 2007, 2009; Prelević and Foley, 2007; Owen, 2008; Tommasini et al., 2011).

In the Western Mediterranean area lamproitic rocks occur along orogenic belts, mainly in post-collisional extensional tectonic setting from Eocene to Pleistocene (e.g., Tommasini et al., 2011). Lamproitic to calc-alkaline rocks are then found in four areas (Fig. 1) and represent different magmatic events at the active continental plate margin (e.g., Conticelli et al., 2009). These events occurred at different stages of the tectonic evolution of this region: during Oligocene in the Western Alps, Italy; during Mio–Pliocene in Corsica, France, and nearby Capraia Island, Italy; during Miocene in Murcia and Almeria, South-Eastern Spain; during Plio–Pleistocene in Southern Tuscany, Central Italy (Avanzinelli et al., 2009).

In Western Alps igneous mantle-derived activity occurred between 33 and 29 Ma with hypoabissal intrusions (i.e., dykes) of calc-alkaline, shoshonitic, and lamproite-like rocks (e.g.,

Dal Piaz and Ernst, 1978; Venturelli et al., 1984a; Peccerillo and Martinotti, 2006; Owen, 2008; Conticelli et al., 2009, 2010). The dikes are found in a region that had undergone extensional collapse following crustal thickening associated with Alpine orogeny (Mitchell and Bergman, 1991).

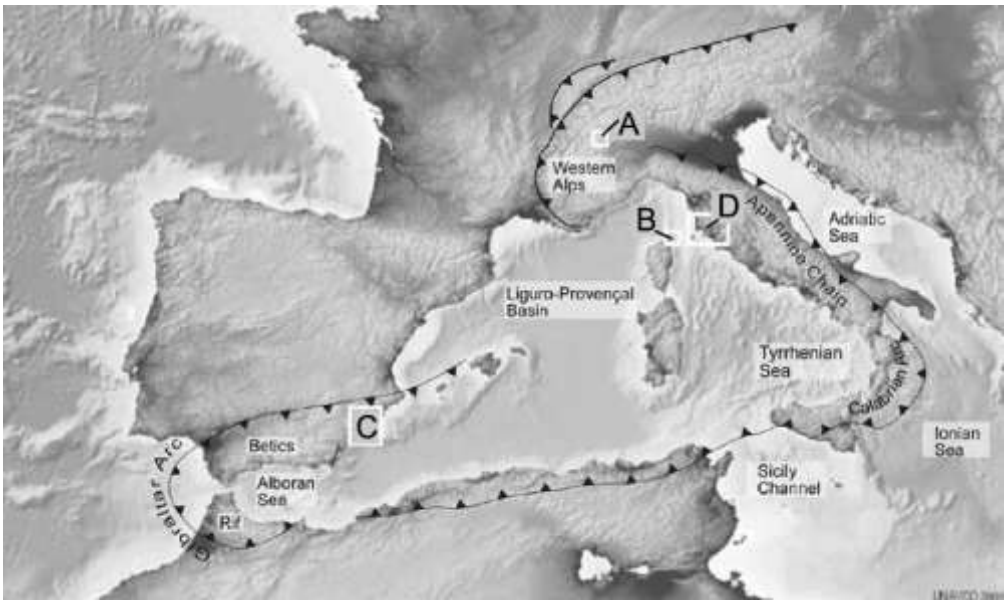

Figure 1. Map of the Western Mediterranean region with reported major tectonic features and areas of occurrence of ultrapotassic to calc-alkaline orogenic rocks. A) Western Alps, Oligocene magmatism. B) Corsica, Miocene–Pliocene. C) Murcia-Almeria, Miocene–Pliocene Magmatism. D) Tuscany, Pliocene–Pleistocene Magmatism. From Conticelli et al. (2009).

In Corsica and western Tyrrhenian basin, igneous rocks were intruded and emplaced as dykes and volcanic bodies, between 14 and 4 Ma respectively (i.e., Civetta et al., 1978; Conticelli et al., 2001; Mascle et al., 2001; Gasparon et al., 2009). High-K calc-alkaline and shoshonites are associated with lamproites, with occurrences at Sisco (NE Corsica), Cornacya (Sardinia channel), Capraia Island, and Elba Island.

In South-Eastern Spain, calc-alkaline rocks, shoshonites and lamproites are intimately associated in the Murcia-Almeria provinces emplaced as submarine igneous activity between 13 and 6 Ma (e.g., Venturelli et al., 1984b, 1991; Benito et al., 1999; Turner et al., 1999; Duggen et al., 2004, 2005, 2008; Mattei et al., 2014). The igneous activity of the Cabo de Gata-Murcia region is a part of Neogene volcanic activity, which is thought to be related with extensional collapse of the Betic-Alboran orogen through low-angle detachment systems involving convective removal of the majority of the lithospheric mantle (e.g., Doblas and Oyarzun, 1989; Oyarzun et al., 1995; Turner et al.,1999), but it has also been attributed to the eastward subduction of Tethyan oceanic lithosphere, still active in the Gibraltar (e.g., Gutscher et al., 2002; Duggen et al., 2004, 2005).

In Tuscany, Central Italy, the onset of igneous activity is Pliocene in age and lasted till the lower Pleistocene (Calabrian) with emplacement of dykes, stocks, and small monogenetic volcanoes from 4.1 to 0.9 Ma (e.g., Avanzinelli et al., 2009; Conticelli et al., 2009, 2010). In this area the magmatism developed at a destructive plate margin where a westward-dipping subduction zone had been active since the Oligocene (e.g., Royden and Karner, 1984; Doglioni et al., 1999; Peccerillo, 1999, 2005).

1.3 Samples description

A total of 18 crystals of phlogopite were selected for the crystal-chemical characterization. Samples studied here come from five different areas: Val d'Albard (Val d'Aosta, Western Alps, Italy), Sisco (Corsica, France), Torre Alfina (Northern Latium, Italy), Orciatico and Montecatini Val di Cecina (Southern Tuscany, Italy). For each locality a total of two crystals has been selected except for VS29 sample from Torre Alfina and ORC1 sample from Orciatico, from which 5 and 3 crystals were respectively analyzed. All the crystals, except ORC1_03 were subjected to X-ray intensity data collection, EMPA and SIMS analyses. Mössbauer spectroscopy was possible for only two samples. An outlook on host-rock characteristics and mineral associations, based on studies from the literature is reported below.

1.3.1 *Western Alps*

Post-orogenic (Oligocene) dykes with lamproitic, shoshonitic and high-K calc-alkaline natures are found within a restricted area in the internal zone of the North-Western Alps. These rocks are found mostly within the Sesia-Lanzo and Combin Units North of the Canavese Line (Owen, 2008).

Lamproitic-like plagioclase-free ultrapotassic dykes (minette) have a micaceous appearance. They are characterized by intersertal textures with phlogopite, clinopyroxene, and K-feldspar, accompanied by minor altered olivine, and riebckite–arfvedsonite amphibole; accessory apatite, sphene, and Fe–Ti oxides are also present.

From a strict classification view-point, lamproite-like rocks are better defined as lamprophyres (Owen, 2008), but, according to Conticelli et al. (2009), the resemblance terminology suggested by Foley et al. (1987) is preferable. The lamproite-like samples have consistently high MgO contents (8.64–13.6 wt.%; Venturelli et al., 1984a). In the SiO_2–K_2O diagram these samples plot close to the lamproitic samples from Corsica and Murcia-Almeria.

1.3.2 Southern Tuscany

Orciatico and Montecatini Val di Cecina bodies are located on the western edge of Val d'Era graben. According to Conticelli et al. (2009), lamproite-like rocks from Tuscany display a large MgO range from 0.98 to 9.58 wt.% but lower K2O at comparable SiO2 contents with respect to other lamproite-like rocks. They are variable in texture and composition (Peccerillo et al., 1988).

Orciatico rocks range from porphyritic to microgranular; the porphyritic rocks contain phenocrysts of olivine, brown phlogopite and clinopyroxene (ranging from diopside to augite) set in a groundmass containing the same phases plus sanidine, variable amounts of glass, and some K-richteritic amphibole (Wagner and Velde 1986).

Montecatini Val di Cecina rocks come from the Q facies described by Conticelli et al. (1992), which shows a porphyritic hypidiomorphic texture with abundant phlogopite and sanidine and minor clinopiroxene and apatite. Micas in the Q facies have a fabric that resembles a primary linear fluidability, due to crystallization and orientation parallel to the flow direction (Conticelli et al., 1992).

1.3.3 Corsica

Dykes, lava flows, and pyroclastic rocks of Mio–Pliocene ages are found closely associated in the north easternmost sector of Corsica Island (France). Sisco lamproitic dykes are situated on the northeastern edge of Corsica Island; according to Conticelli et al. (2009) they show slightly lower MgO contents (6.38–7.13 wt.%,Peccerillo et al., 1987, 1988) with low contents of MgO-rich phenocryst with respect to other Mediterranean lamproites. The body, according to Poli and Peccerillo (2003) is constituted mainly by phlogopite, amphibole and K-pheldspar with microcrystalline groundmass mainly containing sanidine and phlogopite.

1.3.4 Torre Alfina

Samples come from Type-A lavas described by Conticelli et al. (1998). Texture varies from almost aphyric to slightly seriate porphyritic. The only present phenocryst is olivine; the ground mass has an interstitial microcrystalline texture constituted of microphenocrysts of olivine, biotite and colorless clinopyroxene, surrounded by smaller sanidine, olivine, phlogopite, ilmenite and magnetite. On the basis of their major elements, the Torre Alfina lavas closely resemble ultrapotassic rocks with lamproitic affinity from South Tuscany (Peccerillo et al., 1987; 1988) although they show some characteristics transitional to those of Roman potassic rocks.

2 Experimental Methods

2.1 X-ray diffraction data

The choice of crystals suitable for a single crystal X-ray analysis can be a true challenge. Indeed, even if a crystal appears clear and not kinked with no optical anomalies, the thicker is the crystal the highest is the probability it presents a grade of mosaicity so high to make diffraction measurements vain. In order to find a suitable material, dozens of crystals were then checked through a preliminary X-ray diffraction study. The selected crystals were mounted on a carbon fiber and examined on a Bruker MACH3 single-crystal diffractometer with a Mo$K\alpha$ radiation. Unit-cell dimensions were determined by least squares refinement from the setting angles of 24 reflections ($12°<\theta<20°$), by four-position centering (SET4 routine). All crystals analyzed were 1*M* polytypes or $2M_1$ polytypes. Unit-cell parameters and crystal dimensions are reported in Table 2.1.

X-ray data collections were performed on an Oxford Diffraction Xcalibur 3 diffractometer equipped with a Sapphire 2 CCD detector. Intensity data were collected with a monochromatized Mo$K\alpha$ radiation. Intensity integration and standard Lorentz-polarization correction were performed with the *CrysAlis* RED (Oxford Diffraction, 2006) software package. The program ABSPACK in *CrysAlis* RED (Oxford Diffraction, 2006) was used for the absorption correction. Details on experimental conditions and structure refinements are shown in Table 2.1. Structure refinements were performed using the full matrix least-squares program SHELXL-97 (Sheldrick, 2008). The starting model used the coordinates given by Cruciani and Zanazzi (1994) in the *C*2/*m* space group for samples of the 1*M* polytype while, for crystals belonging to the $2M_1$ polytype, coordinates from Scordari et al. (2012a) were initially used. Scattering curves for neutral atoms were taken from the International Tables for X-ray Crystallography (Ibers and Hamilton, 1974).

Crystals SIS50_02, SIS50_07, VS90_01 and VS90_04 showed two high residual density peaks at the end of the refinement. The highest residual was located between the O4 and the interlayer sites, almost at the center of the ditrigonal ring; the other one was found between the basal oxygen planes of two "back-facing" tetrahedral sheets. These residual peaks are commonly reported in micas (e.g. Oberti et al., 1993; Cesare et al., 2003; Nazareni et al., 2008) and, following Oberti et al., (1993), they are due to both [310] twinning and/or the coexistence of mixed 1*M* and $2M_1$ stacking sequences. Indeed, according to Oberti et al. (1993), the displacement of b/3 of consecutive layers along the stacking sequence (corresponding to a 120° rotation), produces twinning about the [310] axis. Furthermore, the $2M_1$ polytype can be derived

from the 1*M* through a stacking error of 120° rotation. The effects of such stacking anomalies are therefore superimposed on $k = 3n$ reflections while they affect reflections with $k \neq 3n$. As suggested by Oberti et al. (1993), a separate rescaling of reflections with $k \neq 3n$, which are systematically underestimated, was adopted and successfully led to the elimination of the spurious peaks. Final atomic coordinates and isotropic displacement parameters are listed in Table 2.2.

2.2 Chemical data

2.2.1 Electron microprobe analysis (EMPA)

The same crystals used in the X-ray diffraction experiments were embedded in epoxy resin and polished; in order to obtain quantitative chemical data, analyses were performed using a JEOL JXA-8200 electron microprobe working in wavelength-dispersion mode, at the laboratories of the Department of Earth Sciences, University of Milan. Analyses were performed using a 3 μm beam at 15 kV and 5 nA beam current. Natural (wollastonite for Si, K-feldspar for K, olivine for Mg, anorthite for Al and Ca, fayalite for Fe, ilmenite for Ti, hornblende for F, omphacite for Na, sanbornite for Ba, rhodonite for Mn and scapolite for Cl) and synthetic (pure V and Cr) phases were used as standards. Raw data were corrected for matrix effects using the ΦρZ method from the JEOL series of programs.

2.2.2 Secondary ion mass spectrometry (SIMS)

Quantification of H and Li was performed with the Cameca IMS 1270 ion microprobe at the Centre de Recherches Pétrographiques et Géochimiques of Nancy, with a O^- primary ion beam of 5nA projected on a 15 μm diameter area. Carbon coating was removed from the polished thin sections that were then coated with Au and kept under vacuum at about $3 \cdot 10^{-8}$ mbar for at least two days prior to the analyses. Two amphiboles (Kipawa and IlimaussaqA) and two phlogopites (*CO1a* and *CO2)* were used as standards (Deloule et al., 1991). The positive secondary ions $^{1}H^{+}$; $^{7}Li^{+}$, $^{29}Si^{+}$ and $^{30}Si^{+}$ were measured with a mass resolution of 3000 (M/ΔM) and an energy offset of 60 ±10eV, to minimize the matrix effect. Before each measurement, the sample was pre-sputtered for 120 seconds with a beam rastering, to clean up the sample surface; the beam position and the magnetic field were centered. Measurements were made by ion counting in monocollection mode by peak switching with counting time and waiting time of 4s and 1s for each peak respectively. The background was measured at each cycle at the mass 0.9 for 4s. 12 successive acquisition cycles are accumulated for each measurement for 9 minutes. The H_2O and

Li concentrations were calculated using the $H^+/^{30}Si^+$ and $Li^+/^{30}Si^+$, with the relative useful yield relative to Si being determined on known natural minerals (Deloule et al., 1991). Analyses of the standards, repeated throughout the whole analytical session, indicate that the error for H_2O and Li contents doesn't exceed 10%.

2.3 Mössbauer spectroscopy

Due to the paucity of material, it was possible to obtain a proper amount of powder only for two samples. The powder was obtained by crushing hand-picked mica crystals under acetone to minimize oxidation by atmospheric oxygen. A powder of 22 and 19 mg was obtained respectively from VDA3 and MVC100 samples. Transmission ^{57}Fe Mössbauer spectra were recorded at room temperature using a conventional Mössbauer apparatus with a 57Co/Rh single-line thin-source. The spectrometer operated in constant acceleration mode over a Doppler velocity range of ±4 mm/s. Data were recorded over 512 channels and folded to give a flat background and a zero-velocity position corresponding to the center shift of metallic α-Fe at RT. Spectra were fitted using the Voigt-based quadrupole splitting distribution (QSD) method developed by Rancourt and Ping (1991) and implemented in the software RECOIL (Lagarec and Rancourt 1997, 1998).

Table 2.1 Experimental details for the selected crystals

	VDA3_X	VDA3_XI	MVC100_02	MVC100_04	ORC1_01	ORC1_02	SIS50_02	SIS50_07	VS29_10
Crystal data									
a (Å)	5.301(1)	5.306(1)	5.302(2)	5.301(1)	5.313(2)	5.324(1)	5.320(2)	5.316(1)	5.314(1)
b (Å)	9.190(1)	9.187(1)	9.185(1)	9.1843(9)	9.202(1)	9.233(1)	9.219(2)	9.206(1)	9.203(1)
c (Å)	10.221(2)	10.227(2)	10.167(2)	10.158(1)	10.105(2)	10.136(1)	10.211(3)	10.217(1)	10.201(2)
β (°)	100.02(1)	100.00(1)	100.08(1)	100.057(9)	100.23(1)	100.28(1)	100.10(2)	100.217(1)	100.06(2)
V (Å^3)	490.3(2)	491.0(1)	487.5(2)	487.0(1)	486.2(2)	490.3(1)	493.0(3)	492.1(1)	491.2(2)
Polytype	1*M*	1*M*	1*M*	1*M*	1*M*	1*M*	1*M*	1*M*	1*M*
Crystal size (µm^3)	8x100x200	8x90x180	15x100x130	10x100x100	20x40x100	15x50x60	15x70x110	15x160x180	10x80x100
Data collection									
θ_{max} (°)	36.8	36.6	36.6	36.4	36.6	36.6	36.7	36.8	36.6
total refl. collected	8899	5899	5042	4941	6565	4681	11119	11300	10880
unique refl. (R_{int})	1252 (5.15)	1230 (8.39)	1216 (3.73)	1202 (6.12)	1221 (5.76)	1209 (7.37)	1251 (6.45)	1257 (4.78)	1244 (7.16)
refl. with $F > 4\sigma(F)$	1001	730	971	806	802	712	954	1024	909
structure refinement									
refined parameters	56	56	56	56	55	56	57	60	56
R_1 [$F > 4\sigma(F)$]	3.88	5.92	3.91	5.99	4.39	5.60	6.19	4.27	5.27
R_1 all	5.24	11.39	5.27	9.37	7.89	11.02	10.75	6.13	7.72
Largest diff. peak and hole (e$^-$/Å^3)	1.61/-0.73	1.53/-0.77	1.24/-0.48	1.92/-0.85	1.58/-0.60	1.06/-0.76	1.64/-0.67	0.85/-0.48	1.34/-1.01

Table 2.1 (continued)

	VS29_11	VS29_12	VS29_01	VS29_08	VS70_15	VS70_16	VS90_01	VS90_04
Crystal data								
a (Å)	5.312(1)	5.319(1)	5.3148(7)	5.318(2)	5.326(1)	5.321(2)	5.318(1)	5.3162(8)
b (Å)	9.207(1)	9.213(1)	9.206(1)	9.219(3)	9.215(4)	9.219(2)	9.195(5)	9.209(1)
c (Å)	10.208(2)	10.201(2)	19.995(2)	20.000(5)	20.050(4)	20.024(4)	19.994(4)	19.988(2)
β (°)	100.08(1)	100.11(1)	95.15(1)	95.09(4)	95.12(2)	95.12(3)	95.10(1)	95.17(1)
V (Å^3)	491.5(1)	492.1(1)	974.4(1)	976.7(6)	980.1(5)	978.3(5)	973.8(6)	974.6(2)
Polytype	1*M*	1*M*	2M_1	2M_1	2M_1	2M_1	2M_1	2M_1
Crystal size (µm^3)	10x80x110	18x80x135	20x120x120	10x90x150	10x50x120	10x60x130	20x90x110	10x60x100
Data collection								
θ_{max} (°)	36.5	36.4	36.5	36.7	36.7	36.6	36.6	36.7
total refl. collected	11124	11078	22060	22134	17976	17996	22529	22481
unique refl. (R_{int} %)	1246 (7.70)	1236 (3.13)	2328(8.39)	2351(11.35)	2334(16.56)	2341(10.16)	2349 (6.06)	2349 (7.12)
refl. with $F > 4\sigma(F)$	916	1155	2.328	1262	970	1186	1360	1274
structure refinement								
refined parameters	56	59	99	96	96	96	97	97
R_1 [$F > 4\sigma(F)$] (%)	4.71	2.36	6.42	7.81	6.59	6.18	7.38	6.42
R_1 all (%)	7.31	2.55	9.82	14.04	17.51	13.15	15.07	14.17
Largest diff. peak and hole (e$^-$/Å^3)	1.36/-0.51	0.47/-0.67	0.75/-0.86	1.30/-1-11	2.20/-0.93	2.03/-0.75	2.46/-0.91	1.41/-0.67

Table 2 2. Fractional atom coordinates (Å), and equivalent isotropic displacement parameters (Å^2) for studied micas

VDA3_X

Atom	*x*	*y*	*z*	U_{iso}
K	0	0	0	.0363(4)
M1	0	½	½	.0120(3)
M2	0	.83336(7)	½	.0122(3)
T	.57574(8)	.16724(4)	.22773(5)	.0134(5)
O1	.8257(2)	.2306(1)	.1694(1)	.0224(3)
O2	.5164(4)	0	.1696(2)	.0221(3)
O3	.63072(2)	.16683(1)	.3906(1)	.0131(2)
O4	.1317(3)	0	.3985(2)	.0138(3)

ORC1_01

Atom	*X*	*y*	*Z*	U_{iso}
K	0	0	0	.0311(3)
M1	0	½	½	.0100(4)
M2	0	.83904(8)	½	.0120(3)
T	.5744(1)	.16706(6)	.22399(7)	.0130(2)
O1	.8182(3)	.2364(2)	.1653(2)	.0230(4)
O2	.5274(5)	0	.1667(3)	.0218(5)
O3	.6312(3)	.1685(2)	.3895(2)	.0139(3)
O4	.1296(4)	0	.3994(3)	.0127(4)

VDA3_XI

Atom	*x*	*y*	*Z*	U_{iso}
K	0	0	0	.0365(7)
M1	0	½	½	.0110(6)
M2	0	.8333(1)	½	.0106(5)
T	.5759(2)	.16676(8)	.22777(9)	.0141(2)
O1	.8251(5)	.2308(3)	.1697(2)	.0227(5)
O2	.5177(7)	0	.1701(3)	.0221(7)
O3	.6303(4)	.1669(2)	.3903(2)	.0136(4)
O4	.1310(5)	0	.3979(3)	.0137(6)

ORC1_02

Atom	*X*	*Y*	*Z*	U_{iso}
K	0	0	0	.0332(5)
M1	0	½	½	.0111(5)
M2	0	.8393(1)	½	.0140(4)
T	.5742(2)	.16717(9)	.2238(1)	.0138(2)
O1	.8173(5)	.2370(3)	.1652(3)	.0236(6)
O2	.5281(8)	0	.1667(4)	.0250(8)
O3	.6309(4)	.1691(2)	.3896(3)	.0148(5)
O4	.1286(6)	0	.3988(3)	.0145(6)

MVC100_02

Atom	*X*	*y*	*Z*	U_{iso}
K	0	0	0	.03238(4)
M1	0	½	½	.0107(3)
M2	0	.83338(7)	½	.0111(3)
T	.57542(8)	.16671(5)	.22616(5)	.0110(1)
O1	.8248(3)	.2315(2)	.1679(1)	.0197(3)
O2	.5192(4)	0	.1682(2)	.0193(4)
O3	.6308(2)	.1669(1)	.3908(1)	.0112(2)
O4	.1321(3)	0	.4000(2)	.0094(2)

SIS50_02

Atom	*X*	*Y*	*Z*	U_{iso}
K	0	0	0	.0381(3)
M1	0	½	½	.0114(2)
M2	0	.83714(5)	½	.0135(2)
T	.57493(6)	.16697(4)	.22645(4)	.01418(9)
O1	.8202(2)	.2350(1)	.1677(1)	.0237(2)
O2	.5249(3)	0	.1692(1)	.0237(3)
O3	.6305(2)	.16768(9)	.39016(9)	.0139(2)
O4	.1309(2)	0	.3982(1)	.0139(2)

MVC100_04

Atom	*X*	*y*	*Z*	U_{iso}
K	0	0	0	.0362(7)
M1	0	½	½	.0123(6)
M2	0	.83338(7)	½	.0133(5)
T	.57542(8)	.16671(5)	.22616(5)	.0150(2)
O1	.8248(3)	.2315(2)	.1679(1)	.0227(5)
O2	.5192(4)	0	.1682(2)	.0236(7)
O3	.6308(2)	.1669(1)	.3908(1)	.0144(4)
O4	.1321(3)	0	.4000(2)	.0123(5)

SIS50_07

Atom	*X*	*Y*	*Z*	U_{iso}
K	0	0	0	.0348(2)
M1	0	½	½	.0100(1)
M2	0	.83578(3)	½	.0116(1)
T	.57537(4)	.16684(2)	.22682(2)	.01191(6)
O1	.8236(1)	.23252(7)	.16858(5)	.0209(1)
O2	.5203(2)	0	.16912(7)	.0204(2)
O3	.6306(1)	.16741(5)	.39069(5)	.0119(1)
O4	.1312(1)	0	.39854(7)	.0119(1)

VS29_10

Atom	*X*	*Y*	*Z*	U_{iso}
K	0	0	0	.0393(6)
M1	0	½	½	.0166(5)
M2	0	.83704(9)	½	.0176(4)
T	.5754(1)	.16696(6)	.22648(7)	.0170(2)
O1	.8243(3)	.2315(2)	.1683(2)	.0259(4)
O2	.5178(5)	0	.1693(3)	.0256(5)
O3	.6303(3)	.1677(2)	.3909(2)	.0172(3)
O4	.1316(4)	0	.3992(2)	.0180(4)

VS29_11

Atom	*X*	*Y*	*Z*	U_{iso}
K	0	0	0	.0348(5)
M1	0	½	½	.0121(4)
M2	0	.83628(9)	½	.0137(3)
T	.57531(1)	.16692(6)	.22646(6)	.0127(2)
O1	.8241(3)	.2316(2)	.1683(2)	.0221(4)
O2	.5182(5)	0	.1691(2)	.0221(5)
O3	.6305(3)	.1674(2)	.3908(2)	.0126(3)
O4	.1311(4)	0	.3995(2)	.0128(4)

VS29_12

Atom	*X*	*Y*	*Z*	U_{iso}
K	0	0	0	.0317(2)
M1	0	½	½	.0100(2)
M2	0	.83762(3)	½	.0117(1)
T	.57503(4)	.16697(2)	.22606(2)	.01027(8)
O1	.8244(1)	.23113(8)	.16786(7)	.0191(1)
O2	.5177(2)	0	.16885(9)	.092(2)
O3	.6309(1)	.16794(6)	.39135(6)	.0110(1)
O4	.1315(2)	0	.39935(8)	.0115(2)

VS29_01

Atom	*X*	*Y*	*Z*	U_{iso}
K	0	.0841(2)	¼	.0335(5)
M1	¾	¼	0	.0125(3)
M2	.2385(1)	.07935(8)	.00003(3)	.0141(2)
T1	.4619(2)	.2499(1)	.13809(5)	.0126(2)
T2	.9638(2)	.4173(1)	.13820(5)	.0132(2)
O11	.7407(5)	.3149(3)	.1656(2)	.0228(6)
O21	.2412(5)	.3523(3)	.1671(2)	.0216(6)
O22	.4353(5)	.0837(3)	.1671(1)	.0230(6)
O31	.4296(5)	.2494(3)	.0544(1)	.0154(5)
O32	.9388(5)	.4194(3)	.0545(1)	.0148(4)
O41	.9347(5)	.0830(3)	.0500(1)	.0158(5)

VS29_08

Atom	*X*	*Y*	*Z*	U_{iso}
K	0	.0838(3)	¼	.0338(8)
M1	¾	¼	0	.0129(5)
M2	.2365(2)	.0787(1)	.00006(6)	.0143(4)
T1	.4619(3)	.2498(2)	.13827(8)	.0136(3)
T2	.9641(3)	.4173(2)	.13827(8)	.0137(3)
O11	.7403(8)	.3150(5)	.1658(2)	.0222(9)
O21	.2409(8)	.3519(5)	.1672(2)	.0232(9)
O22	.4357(8)	.0830(5)	.1672(2)	.0229(9)
O31	.4289(7)	.2489(4)	.0544(2)	.0151(7)
O32	.9390(7)	.4194(5)	.0546(2)	.0153(7)
O41	.9336(7)	.0833(5)	.0495(2)	.0169(7)

VS70_15

Atom	*X*	*Y*	*Z*	U_{iso}
K	0	.0842(2)	¼	.0351(7)
M1	¾	¼	0	.0129(4)
M2	.2378(2)	.0791(1)	.00008(5)	.0148(3)
T1	.4621(2)	.2499(2)	.13803(7)	.0150(3)
T2	.9642(2)	.4173(2)	.13809(7)	.0137(3)
O11	.7416(7)	.3145(4)	.1657(2)	.0242(8)
O21	.2412(7)	.3527(4)	.1670(2)	.0249(9)
O22	.4343(7)	.0837(4)	.1666(2)	.0240(8)
O31	.4291(6)	.2487(5)	.0543(2)	.0166(7)
O32	.9392(6)	.4191(5)	.0546(2)	.0163(6)
O41	.9347(6)	.0828(5)	.0502(2)	.0170(6)

VS70_16

Atom	*X*	*Y*	*Z*	U_{iso}
K	0	.0840(2)	¼	.0348(6)
M1	¾	¼	0	.0133(3)
M2	.2376(1)	.07922(8)	.00003(4)	.0148(3)
T1	.4617(2)	.2499(1)	.1381(1)	.0142(2)
T2	.9639(2)	.4171(1)	.1381(1)	.0139(2)
O11	.7411(6)	.3148(3)	.1657(2)	.0239(7)
O21	.2418(6)	.3520(3)	.1671(2)	.0233(7)
O22	.4358(6)	.0833(3)	.1667(4)	.0230(6)
O31	.4294(5)	.2487(3)	.0544(1)	.0161(5)
O32	.9390(5)	.4187(3)	.0541(1)	.0164(5)
O41	.9340(5)	.0824(3)	.0499(1)	.0166(5)

VS90_01

Atom	*X*	*Y*	*Z*	U_{iso}
K	0	.08424(9)	¼	.0343(3)
M1	¾	¼	0	.0129(2)
M2	.23985(7)	.07967(4)	.00002(2)	.0142(1)
T1	.46187(9)	.25010(6)	.13818(2)	.0133(1)
T2	.96368(9)	.41736(6)	.13818(2)	.0161(1)
O11	.7406(3)	.3151(2)	.1660(1)	.0233(3)
O21	.2401(3)	.3520(2)	.1670(1)	.0234(3)
O22	.4360(3)	.0837(2)	.16679(7)	.0233(3)
O31	.4308(2)	.2499(2)	.05463(6)	.0163(3)
O32	.9387(2)	.4194(2)	.05450(6)	.0166(2)
O41	.9342(2)	.0836(2)	.04970(6)	.0160(2)

VS90_04

Atom	*X*	*Y*	*Z*	U_{iso}
K	0	.0843(2)	¼	.0333(7)
M1	¾	¼	0	.0121(4)
M2	.2392(2)	.0796(1)	.00002(5)	.0135(4)
T1	.4620(2)	.2501(2)	.13817(7)	.0126(3)
T2	.9636(2)	.4173(2)	.13814(7)	.0138(3)
O11	.7401(7)	.3152(4)	.1657(2)	.0225(9)
O21	.2403(7)	.3515(4)	.1670(2)	.0216(9)
O22	.4365(7)	.0835(4)	.1669(2)	.0219(8)
O31	.4301(6)	.2496(5)	.0547(2)	.0159(7)
O32	.9387(6)	.4191(5)	.0546(2)	.0155(7)
O41	.9340(6)	.0828(5)	.0497(2)	.0146(6)

3 Results

3.1 Single crystal X-ray diffraction

Selected interatomic distances and mean electron numbers (*m.e.n.*) are shown in Tables 3.1 and 3.2. Micas from selected lamproites are chemically *homo-octahedral* (Ďurovič 1994; Ferraris and Ivaldi 2002; Nespolo and Ďurovič 2002) since the difference between *m.e.n* of M1 and M2 is always < 1 (Schingaro et al., 2001). Geometrical features of these micas point on the other hand towards a meso-octahedral nature since the difference between <M1-O> and <M2-O> is always greater than 1σ (Weiss et al., 1992), although the range of variation is very wide. This fact makes it very hard to gather general inferences on cation distributions over M1 and M2 sites. However, as it will discussed in chapter 5, crystal chemical considerations based on the analysis of individual M-O distances and structural distortions (Tables 3.3 and 3.4.) are able to provide useful information concerning cation distribution.

3.2 Chemistry

EMPA and SIMS data are presented in Table 3.5. The studied samples are Ti- and F- bearing phlogopites and show a modest "brittle mica component" due to the presence of small quantities of Ba. SIMS data show that H_2O content ranges from that of an almost pure *oxy*-mica end-member to that typical of a moderately dehydrogenated one; in addition, all the samples bear moderate amounts of Li.

Calculation of the structural formula of micas is a critical aspect that presents many intricacies. Several normalization schemes (Waters and Charnley, 2002; Mesto et al., 2006) may be used and each one of them is based on somewhat arbitrary assumptions concerning parameters that could be lacking or ambiguously determined, namely H, Li and other light elements concentration other than the Fe^{2+}/Fe_{tot} ratio. Furthermore this implies, when feasible, combining data from different analytical techniques. In this work, the combined use of EMPA and SIMS data implies a comparison between data measured on a different volumetric scale: micro-volumes involved in the production of X-rays and secondary ions in fact cannot match exactly. Indeed, X-rays emitted during an electron-beam bombardment emanate from a few micrometers depth, whereas the secondary analytical ions are produced by a shallower depth (<1 μm). For these reasons, the suggestion of a relative uncertainty for H and Li concentrations near 10–15% seems realistic.

The most common normalization methods used for trioctahedral micas are summarized below:

a) The negative charge is assumed to be equal to 22, which is the same as constraining the anionic composition as the ideal $O_{10}(OH,F,Cl)_2$.

b) When possible, the electrostatic balance can also be inferred from the measured anionic composition and, although this would imply the quantification of oxygen, this method is usually applied employing the measured values of only H, F and Cl using an esteem of the oxygen content obtained by microprobe analyses.

These two methods are obviously affected by the indetermination of the Fe^{2+}/Fe_{tot} ratio but they are both useful to get an esteem of octahedral and interlayer vacancies, especially through the method b), given the more accurate evaluation of the anionic component.

We can base our normalization procedure also on a fixed number of cations, in this case the most common methods are:

c) The total number of tetrahedral, octahedral and interlayer cations is fixed to 8; this scheme is nonetheless rarely used since it is compromised by the usually low (<1 a.p.f.u.) sum of the interlayer cations.

d) The total number of octahedral and tetrahedral cations is normalized to 7, this method is more commonly used but it is still influenced by the possible presence of octahedral vacancies.

e) An iterative method was developed by Dymek (1983); this procedure however is based on the assumption that "Ti-vacancy" and $3\,{}^{VI}M^{2+} \leftrightarrow 2\,{}^{VI}Al^{3+} + {}^{VI}\square$ are the only substitutions mechanisms occurring and it has been developed for Al-rich metamorphic biotites.

Methods a), c) have not been used since they lie on too strong assumptions of the occupancy of anionic sites and interlayer cations respectively and would then lead to a too high approximation while method e) was not employed because of the specificity of its assumptions. Formula recalculations have then been at first performed using the method b) and d) on the basis of both SIMS and EMPA data (Tables 3.6 and 3.7) and assuming all Fe as Fe^{2+} and Ti as Ti^{4+}. In many cases, both the methods showed unsatisfactory results since charge balance could not be achieved. The very different chemical composition showed by the samples made it necessary to elaborate a different strategy for each crystal. For this reason all these aspects will be discussed in detail in chapter 5 on a case-by-case basis.

3.3 Mössbauer spectroscopy

Mössbauer spectra for samples VDA3 and MVC100 are reported in Figure 3.1 a and b respectively. The three main absorption bands are positioned at about -0.2, 0.8 and 2.4 mm/s for VDA3 and -0.1, 0.8 and 2.3 for MVC100. These features indicate the presence of octahedral Fe^{2+} and Fe^{3+} doublets. No evidence was found for the presence of Fe^{3+} in tetrahedral coordination. Table 3.8 lists Mössbauer parameters obtained by the QSD fitting method.

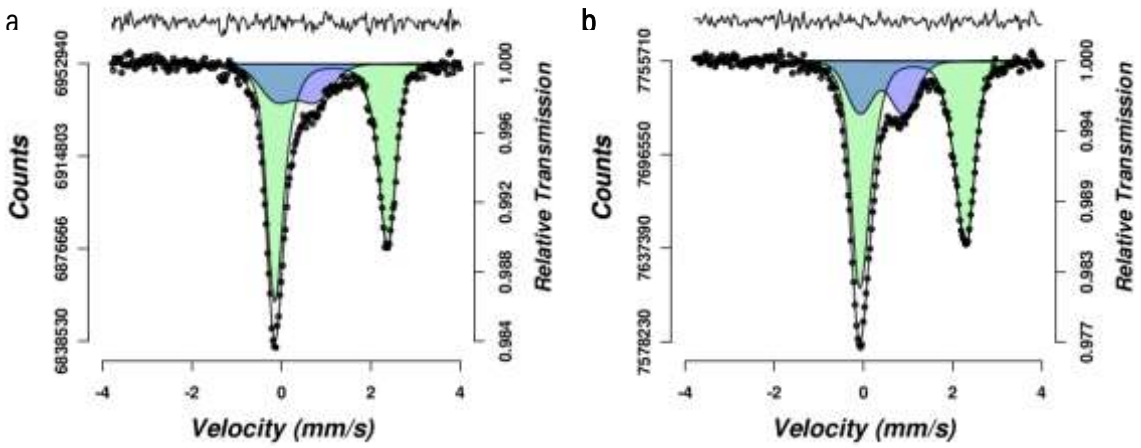

Figure 3.1. Room-temperature Mössbauer spectra of samples VDA3 (**a**) and MVC100 (**b**)

Table 3.1 Selected interatomic distances (Å) and mean electron numbers for 1*M* studied micas

	VDA3_X	VDA3_XI	MVC100_02	MVC100_04	ORC1_01	ORC1_02	SIS50_02	SIS50_07	VS29_10	VS29_11	VS29_12
K											
O1 (x4)	2.983(1)	2.988(2)	2.976(1)	2.981(2)	3.005(2)	3.020(3)	3.019(1)	3.0003(6)	2.987(2)	2.989(2)	2.9834(8)
O1' (x4)	3.327(1)	3.326(2)	3.306(2)	3.296(3)	3.245(2)	3.247(3)	3.283(1)	3.3072(7)	3.315(2)	3.315(2)	3.3178(8)
O2 (x2)	2.974(2)	2.985(3)	2.976(2)	2.978(3)	3.002(3)	3.011(4)	3.015(2)	2.9901(2)	2.982(3)	2.982(3)	2.980(1)
O2' (x2)	3.336(2)	3.335(3)	3.309(2)	3.303(3)	3.262(2)	3.268(4)	3.302(2)	3.3243(9)	3.331(3)	3.328(3)	3.332(1)
$<K-O>_{inner}$	2.980	2.987	2.976	2.980	3.004	3.017	3.018	2.997	2.985	2.987	2.982
$<K-O>_{outer}$	3.330	3.329	3.307	3.298	3.251	3.254	3.289	3.313	3.320	3.319	3.323
<K-O>	3.155	3.158	3.142	3.139	3.127	3.136	3.154	3.155	3.153	3.153	3.152
m.e.n	18.68	18.68	18.36	18.04	19.00	19.00	18.36	18.68	18.68	18.68	18.36
M1											
O4 (x2)	2.045(2)	2.053(3)	2.036(2)	2.034(3)	2.048(2)	2.059(3)	2.055(1)	2.0490(7)	2.046(2)	2.047(2)	2.0467(9)
O3 (x4)	2.086(1)	2.088(2)	2.082(1)	2.082(2)	2.101(2)	2.110(2)	2.098(1)	2.0928(5)	2.090(2)	2.091(2)	2.0923(6)
<M1-O>	2.072	2.076	2.067	2.066	2.083	2.093	2.084	2.078	2.075	2.076	2.077
m.e.n	12.84	12.56	13.68	12.56	14.80	15.92	14.24	13.12	13.68	13.68	14.24
M2											
O4 (x2)	2.040(1)	2.042(3)	2.029(1)	2.027(2)	1.987(2)	1.993(3)	2.018(1)	2.0255(5)	2.012(2)	2.015(2)	2.0085(6)
O3 (x2)	2.079(1)	2.084(2)	2.075(1)	2.077(2)	2.077(2)	2.082(2)	2.086(1)	2.0798(6)	2.083(2)	2.081(2)	2.0790(7)
O3' (x2)	2.084(1)	2.084(2)	2.079(1)	2.08(2)	2.115(2)	2.118(3)	2.110(1)	2.0993(6)	2.102(2)	2.100(2)	2.1041(6)
<M2-O>	2.068	2.070	2.061	2.061	2.060	2.064	2.071	2.068	2.066	2.065	2.064
m.e.n	12.84	12.56	13.68	13.12	15.08	15.92	14.24	13.68	14.24	14.24	14.80
T											
O1	1.652(1)	1.654(2)	1.648(1)	1.647(2)	1.645(2)	1.648(3)	1.652(1)	1.6498(6)	1.652(2)	1.652(2)	1.6534(7)
O3	1.640(1)	1.637(2)	1.648(1)	1.644(2)	1.646(2)	1.654(3)	1.646(1)	1.6477(6)	1.652(2)	1.652(2)	1.6600(7)
O2	1.6535(8)	1.651(1)	1.6490(8)	1.649(1)	1.646(1)	1.651(2)	1.6515(7)	1.6526(4)	1.653(1)	1.653(1)	1.6546(4)
O1'	1.652(1)	1.649(2)	1.652(2)	1.650(2)	1.646(2)	1.649(3)	1.652(1)	1.6550(6)	1.652(2)	1.654(2)	1.6544(7)
<T-O>	1.649	1.648	1.649	1.648	1.646	1.651	1.650	1.651	1.652	1.653	1.656

Table 3.2 Selected interatomic distances (Å) and mean electron numbers for 2M_1 studied micas

	VS29_01	VS29_08	VS70_15	VS70_16	VS90_01	VS90_04
K						
O11 (x2)	2.974(3)	2.979(5)	2.973(4)	2.976(3)	2.970(2)	2.975(4)
O11' (x2)	3.319(3)	3.315(5)	3.329(4)	3.323(4)	3.312(2)	3.316(4)
O21 (x2)	2.964(3)	2.968(5)	2.969(4)	2.969(3)	2.969(2)	2.973(4)
O21' (x2)	3.298(3)	3.296(5)	3.305(4)	3.300(4)	3.289(2)	3.289(4)
O22 (x2)	2.965(3)	2.966(4)	2.972(4)	2.974(3)	2.972(2)	2.973(4)
O22' (x2)	3.296(3)	3.297(5)	3.313(4)	3.302(3)	3.298(1)	3.292(4)
$\langle K\text{-}O\rangle_{inner}$	2.968	2.971	2.971	2.973	2.970	2.974
$\langle K\text{-}O\rangle_{outer}$	3.304	3.303	3.316	3.308	3.300	3.299
<K-O>	3.136	3.137	3.144	3.141	3.135	3.136
m.e.n	18.20	18.20	18.04	18.20	18.04	18.52
M1						
O31 (x2)	2.101(3)	2.105(4)	2.107(3)	2.105(3)	2.099(1)	2.104(3)
O32 (x2)	2.105(3)	2.109(4)	2.108(4)	2.103(3)	2.104(2)	2.104(4)
O41 (x2)	2.037(3)	2.031(4)	2.044(4)	2.042(3)	2.029(1)	2.034(4)
<M1-O>	2.081	2.082	2.086	2.083	2.077	2.081
m.e.n	18.44	18.16	18.16	18.16	17.88	18.16
M2						
O31	2.073(3)	2.078(4)	2.080(4)	2.079(3)	2.072(2)	2.074(4)
O31'	2.113(3)	2.120(4)	2.113(4)	2.114(3)	2.116(2)	2.117(4)
O32	2.068(3)	2.073(4)	2.076(4)	2.078(3)	2.067(2)	2.071(4)
O32'	2.113(3)	2.123(4)	2.121(3)	2.118(3)	2.107(1)	2.113(4)
O41	1.974(3)	1.963(4)	1.976(3)	1.972(3)	1.979(2)	1.977(4)
O41'	1.979(3)	1.967(4)	1.980(4)	1.974(3)	1.983(1)	1.977(4)
<M2-O>	2.053	2.054	2.058	2.056	2.054	2.055
m.e.n	18.16	18.3	18.02	18.02	17.46	17.74
T1						
O11	1.646(3)	1.647(5)	1.653(4)	1.651(3)	1.648(1)	1.644(4)
O21	1.650(3)	1.650(5)	1.655(4)	1.647(3)	1.650(2)	1.648(4)
O22	1.647(3)	1.653(5)	1.647(4)	1.650(3)	1.644(2)	1.648(4)
O31	1.666(3)	1.670(4)	1.672(4)	1.670(3)	1.664(1)	1.661(4)
<T-O>	1.652	1.655	1.657	1.655	1.652	1.650
T2						
O11	1.647(3)	1.651(5)	1.651(4)	1.649(3)	1.649(2)	1.649(4)
O21	1.647(3)	1.648(5)	1.648(4)	1.653(3)	1.644(1)	1.647(4)
O22	1.649(3)	1.645(5)	1.649(4)	1.648(3)	1.643(2)	1.645(4)
O32	1.668(3)	1.667(4)	1.668(4)	1.668(3)	1.666(1)	1.663(4)
<T-O>	1.653	1.653	1.654	1.655	1.651	1.651

Table 3.3 Selected structural parameters for 1*M* studied micas

	VDA3_X	VDA3_XI	MVC100_02	MVC100_04	ORC1_01	ORC1_02	SIS50_02	SIS50_07	VS29_10	VS29_11	VS29_12
Whole layer											
Δ_{TM} (Å)	0.490	0.479	0.507	0.501	0.471	0.457	0.463	0.487	0.503	0.504	0.517
β_{ideal}	99.955	99.959	100.011	100.018	100.094	100.084	100.001	99.988	100.000	99.989	100.009
intralayer shift	-0.335	-0.335	-0.336	-0.335	-0.338	-0.340	-0.337	-0.341	-0.335	-0.336	-0.337
Interlayer											
$V_{K\text{-}inner}$(Å^3)	35.29	35.53	35.11	35.24	36.00	36.392	36.60	35.87	35.45	35.51	35.35
t_{int} (Å)	3.412	3.422	3.364	3.358	3.302	3.310	3.387	3.396	3.391	3.391	3.382
$\Delta_{K\text{-}O}$ (Å)	0.350	0.342	0.331	0.318	0.247	0.237	0.272	0.316	0.335	0.333	0.340
Tet. sheet											
α (°)	7.6620	7.5744	7.3052	6.9150	5.3825	5.1530	5.9399	6.9118	7.3030	7.2698	7.4602
Δz (Å)	0.0020	0.0040	0.0030	0.0050	0.0139	0.0150	0.0147	0.0050	0.0100	0.0080	0.0100
τ (°)	110.74	110.74	110.67	110.73	110.60	110.59	110.76	110.69	110.58	110.61	110.57
TAV_T	2.107	1.853	1.755	1.9514	1.580	1.542	2.053	1.823	1.533	1.609	1.480
TQE_T	1.0005	1.0004	1.0004	1.0005	1.0004	1.0004	1.0005	1.0004	1.0004	1.0004	1.0004
BLD_T	0.296	0.319	0.076	0.121	0.015	0.121	0.144	0.153	0.015	0.045	0.145
$T_{disp.}$	0.035	0.037	0.034	0.035	0.030	0.033	0.037	0.035	0.030	0.032	0.028
V_T (Å^3)	2.301	2.295	2.299	2.294	2.287	2.307	2.305	2.287	2.31	2.31	2.33
t_{tet} (Å)	2.220	2.219	2.230	2.225	2.223	2.230	2.233	2.229	2.229	2.229	2.244
Oct. sheet											
V_{M1} (Å^3)	11.68	11.75	11.56	11.55	11.82	11.96	11.87	11.77	11.71	11.72	11.73
V_{M2} (Å^3)	11.60	11.66	11.47	11.48	11.46	11.52	11.68	11.62	11.56	11.56	11.52
ψ_{M1} (°)	58.76	58.67	59.07	59.05	59.22	59.24	58.87	58.92	59.02	59.03	59.19
ψ_{M2} (°)	58.69	58.57	58.97	58.97	58.84	58.76	58.65	58.75	58.87	58.84	58.97

	VDA3_X	VDA3_XI	MVC100_02	MVC100_04	ORC1_01	ORC1_02	SIS50_02	SIS50_07	VS29_10	VS29_11	VS29_12
OAV_{M1}	34.282	32.519	39.270	38.950	42.145	41.630	35.691	36.718	38.336	38.443	40.886
OAV_{M2}	33.158	31.193	37.810	37.923	36.684	35.416	32.963	34.113	36.208	35.944	37.913
OQE_{M1}	1.0105	1.0099	1.0122	1.0121	1.0131	1.0130	1.0110	1.0113	1.0119	1.0119	1.0127
OQE_{M2}	1.0101	1.0095	1.0116	1.0116	1.0117	1.0112	1.0103	1.0105	1.0113	1.0112	1.0118
BLD_{M1}	0.885	0.755	0.984	1.033	1.136	1.083	0.912	0.940	0.948	0.948	0.978
BLD_{M2}	0.887	0.902	1.035	1.116	2.347	2.310	1.723	1.380	1.727	1.631	1.787
ELD_{M1}	4.863	4.740	5.196	5.164	5.382	5.378	4.960	5.030	5.146	5.156	5.324
ELD_{M2}	4.765	4.622	5.079	5.072	4.923	4.816	4.726	4.831	4.956	4.931	5.069
$Shift_{M2}$(Å)	0.0009	0.0000	0.0007	0.0009	0.0525	0.0554	0.0354	0.0230	0.0341	0.0276	0.0396
w	0.080	0.077	0.092	0.098	0.098	0.092	0.081	0.078	0.083	0.087	0.080
$t_{M(O3)}$ (Å)	2.202	2.210	2.186	2.190	2.198	2.202	2.208	2.208	2.198	2.192	2.195
$t_{M(O4)}$ (Å)	2.043	2.057	2.002	1.994	2.001	2.019	2.047	2.047	2.041	2.025	2.020
$t_{M(O3\text{-}O4)}$ (Å)	2.149	2.159	2.125	2.125	2.132	2.141	2.155	2.155	2.146	2.136	2.137

Notes: Δ_{TM} =dimensional misfit = $2\sqrt{3}\langle O\text{-}O\rangle_{basal}\text{-}3\sqrt{2}(\langle M1\text{-}O\rangle+\langle M2\text{-}O\rangle+\langle M3\text{-}O\rangle)/3$; β_{ideal} = ideal monoclinic angle = $\cos^{-1}(-a/3c)$; intralayer shift = $c\cos\beta/a$; t_{int} = interlayer separation, calculated from the *z* coordinates of basal O atoms; $\Delta_{K\text{-}O}$ = difference between mean bond length for *inner*/*outer* K-O bonds; α = tetrahedral rotation angle (Hazen and Burnham, 1973); Δz = departure from co-planarity of the basal O atoms (Güven, 1971); τ = tetrahedral flattening angle; TAV = tetrahedral angle variance (Robinson et al., 1971); TQE = tetrahedral quadratic elongation (Robinson et al., 1971); T_{disp}.= Tetrahedral displacement, calculated as in Brigatti and Guggenheim (2002); t_{tet} = tetrahedral sheet thickness calculated from *z* coordinates of basal and apical O atoms; ψ = octahedral flattening angle (Hazen and Burnham 1973); OQE = octahedral quadratic elongation (Robinson et al., 1971); OAV = octahedral angle variance (Robinson et al., 1971); BLD and ELD = octahedral bond-length and edge-length distortion parameters (Kunz et al., 1991); $Shift_{M2}$ = off-center shift (Laurora et al., 2007); *w* = O3 and O4 "non-planarity" parameter (Mercier et al., 2005); $t_{M(O3\text{-}O4)}$, $t_{M(O3)}$, $t_{M(O4)}$, octahedral sheet thickness calculated from the *z* coordinates, respectively, of all oxygens bonded to octahedral cations (O3 and O4), of only the tetrahedral apical oxygens (O3), and of only oxygens bonded to hydrogens (O4) (Toraya, 1981).

Table 3.4 Selected structural parameters for 2M_1 studied micas

	VS29_01	VS29_08	VS70_15	VS70_16	VS90_01	VS90_04
Whole layer						
Δ_{TM} (Å)	0.534	0.533	0.530	0.533	0.530	0.525
β_{ideal}	95.08	95.08	95.08	95.08	95.09	95.09
intralayer shift	-0.338	-0.334	-0.336	-0.336	-0.334	-0.339
Interlayer						
$V_{K\text{-}inner}$(Å^3)	34.79	34.90	34.94	34.99	34.89	35.00
t_{int} (Å)	3.318	3.321	3.324	3.321	3.318	3.315
$\Delta_{K\text{-}O}$ (Å)	0.337	0.332	0.344	0.335	0.329	0.325
Tet. sheet						
α (°)	7.37	7.27	7.53	7.34	7.22	7.13
Δz (Å)	0.030	0.027	0.022	0.024	0.019	0.025
τ_{T1} (°)	110.15	110.09	110.09	110.09	110.09	110.07
τ_{T2} (°)	110.06	110.12	110.08	110.11	110.12	110.12
TAV_{T1}	0.5590	0.5013	0.5274	0.5092	0.4795	0.4407
TAV_{T2}	0.4478	0.5256	0.4853	0.5196	0.5639	0.4856
TQE_{T1}	1.0002	1.0002	1.0002	1.0002	1.0002	1.0002
TQE_{T2}	1.0002	1.0002	1.0002	1.0002	1.0002	1.0002
BLD_{T1}	0.409	0.453	0.468	0.483	0.393	0.318
BLD_{T2}	0.469	0.439	0.423	0.423	0.485	0.363
$T1_{disp.}$	0.011	0.015	0.013	0.010	0.014	0.011
$T2_{disp.}$	0.010	0.010	0.007	0.012	0.007	0.012
V_{T1} (Å^3)	2.31	2.33	2.33	2.32	2.31	2.31
V_{T2} (Å^3)	2.31	2.32	2.32	2.32	2.31	2.31
t_{tet} (Å)	2.242	2.243	2.245	2.248	2.241	2.238
Oct. sheet						
V_{M1} (Å^3)	11.75	11.75	11.85	11.79	11.69	11.74
V_{M2} (Å^3)	11.33	11.33	11.40	11.36	11.34	11.35
ψ_{M1} (°)	60.16	60.00	60.08	60.17	59.87	60.80
ψ_{M2} (°)	59.71	59.55	59.63	59.74	59.50	60.39
OAV_{M1}	47.640	49.203	46.766	47.905	46.817	47.319
OAV_{M2}	42.313	45.079	41.773	43.203	42.378	42.184
OQE_{M1}	1.0151	1.0158	1.0148	1.0152	1.0149	1.0151
OQE_{M2}	1.0135	1.0146	1.0134	1.0139	1.0135	1.0135
BLD_{M1}	1.4099	1.6174	1.3585	1.3285	1.5570	1.4900
BLD_{M2}	2.5009	2.8893	2.5758	2.6837	2.3698	2.5228
ELD_{M1}	5.7623	5.8463	5.7086	5.7857	5.6998	5.7362
ELD_{M2}	5.2108	5.3013	5.1403	5.2453	5.2480	5.2184
$Shift_{M2}$(Å)	0.071	0.087	0.12	0.076	0.063	0.066
w	0.089	0.100	0.085	0.090	0.097	0.153
$t_{M(O3)}$ (Å)	2.151	2.191	2.157	2.154	2.191	2.190
$t_{M(O4)}$ (Å)	1.991	1.972	2.005	1.990	1.980	1.871
$t_{M(O3\text{-}O4)}$ (Å)	2.071	2.082	2.081	2.072	2.085	2.030

Notes: see Table 3.3

Table 3.5 Electron microprobe analyses (means in wt% of oxides) for studied micas

	VDA3_X	VDA3_XI	MVC100_02	MVC100_04	ORC1_01	ORC1_02	ORC1_03	SIS50_02	SIS50_07
SiO_2	41.6	42.4	41.3	42.4	38.5	38.5	38.7	39.9	41.7
TiO2	1.50	1.36	1.38	1.44	7.97	7.96	7.64	5.84	3.91
Al2O3	12.57	12.43	13.13	12.35	12.6	12.04	12.2	11.69	12.50
V2O3	-	-	0.05	0.05	0.16	0.14	0.16	0.08	0.09
Cr2O3	1.02	0.89	1.23	0.62	0.07	-	0.05	-	0.54
MgO	25.6	26.0	24.3	25.5	17.3	16.3	18.4	18.6	23.6
MnO	-	-	0.05	0.05	0.06	0.06	0.05	0.09	-
FeO	2.69	2.58	3.99	3.00	9.28	10.68	7.97	9.56	3.76
BaO	0.16	0.14	0.10	0.07	1.66	1.70	1.57	0.27	0.13
Na2O	0.06	0.04	0.31	0.34	0.45	0.43	0.35	0.10	0.10
K2O	10.44	10.53	10.06	10.03	9.04	8.75	9.15	10.04	10.38
F	1.34	1.27	4.30	4.30	3.09	2.67	3.68	1.02	1.49
total $_{(EMPA)}$	96.41	97.04	98.32	98.3	98.93	98.1	98.35	96.73	97.59
H2O*	2.64	2.74	1.72	2.00	0.64	1.08	0.79	1.26	2.12
Li_2O*	0.02	0.02	0.02	0.01	0.12	0.10	0.12	0.04	0.01
total $_{(EMPA+SIMS)}$	99.07	99.8	100.06	100.31	99.69	99.28	99.26	98.03	99.72

Notes: * SIMS data

Table 3.5 (continued)

	VS29_01	VS29_08	VS29_10	VS29_11	VS29_12	VS70_15	VS70_16	VS90_01	VS90_04
SiO_2	36.2	36.0	39.9	40.6	39.4	35.8	35.5	35.4	36.5
TiO2	6.73	6.47	3.69	3.04	3.98	6.89	6.90	6.57	6.47
Al2O3	16.98	17.18	13.99	13.85	14.18	16.73	16.75	16.73	16.65
V2O3	0.55	0.28	0.09	0.11	0.09	0.30	0.28	0.28	0.26
Cr2O3	0.26	0.15	0.10	1.34	0.79	0.14	0.14	0.13	0.13
MgO	11.09	11.06	22.16	22.84	21.42	11.23	11.18	11.09	11.15
MnO	-	-	-	-	-	-	-	-	-
FeO	16.11	16.53	5.77	4.23	5.70	15.88	15.86	16.85	16.63
BaO	0.18	0.23	0.23	0.25	0.32	0.21	0.16	0.17	0.18
Na2O	0.41	0.45	0.11	0.10	0.17	0.39	0.37	0.39	0.37
K2O	9.33	9.21	10.26	10.13	10.13	9.31	9.36	9.35	9.45
F	0.88	0.99	1.29	1.49	1.57	0.60	0.79	1.80	1.53
$total_{(EMPA)}$	98.32	98.17	97.01	97.36	97.04	97.18	96.99	97.98	98.67
H2O*	0.64	0.56	1.80	1.89	1.58	0.69	0.62	0.60	0.37
Li*	0.06	0.02	0.01	0.01	0.01	0.03	0.04	0.05	0.07
$total_{(EMPA+SIMS)}$	99.02	98.75	98.82	99.26	98.63	97.9	97.65	98.63	99.11

Table 3.6 Atomic ratios calculated on the basis of (O+F+OH)=12

	VDA3_X	VDA3_XI	MVC100_02	MVC100_04	ORC1_01	ORC1_02	ORC1_03	SIS50_02	SIS50_07
Si	2.99	3.02	2.94	2.99	2.90	2.92	2.89	3.04	3.00
^{IV}Al	1.01	0.98	1.06	1.01	1.10	1.08	1.08	0.96	1.00
^{IV}Sum	4.00	4.00	4.00	4.00	4.00	4.00	3.97	4.00	4.00
Ti^{4+}	0.08	0.07	0.07	0.08	0.45	0.45	0.43	0.33	0.21
^{VI}Al	0.05	0.06	0.04	0.02	0.02	-	-	0.09	0.06
Fe^{2+}	0.16	0.15	0.24	0.18	0.58	0.68	0.5	0.61	0.23
Mg	2.74	2.75	2.58	2.67	1.95	1.84	2.06	2.11	2.53
Cr	0.06	0.05	0.07	0.03	-	-	-	-	0.03
V^{3+}	-	-	-	-	0.01	0.01	0.01	-	0.01
Mn^{2+}	-	-	-	-	-	-	-	0.01	-
Li	0.01	0.01	0.01	-	0.04	0.03	0.04	0.01	-
^{VI}Sum	3.09	3.08	3.00	2.98	3.01	2.98	3.00	3.15	3.07
K	0.96	0.96	0.92	0.90	0.87	0.85	0.87	0.98	0.95
Na	0.01	0.01	0.04	0.05	0.07	0.06	0.05	0.01	0.01
Ba	-	-	-	-	0.05	0.05	0.05	-	-
^{XII}Sum	0.98	0.98	0.97	0.95	1.03	0.99	1.01	1.01	0.96
OH	1.27	1.3	0.82	0.94	0.32	0.55	0.39	0.64	1.02
F	0.30	0.29	0.97	0.96	0.74	0.64	0.87	0.25	0.34
O	11.11	10.64	10.43	10.41	10.21	10.10	10.94	10.81	10.74
Charge (+)	22.42	22.41	22.16	22.11	22.93	22.83	22.73	23.11	22.62
Charge (-)	22.43	22.41	22.21	22.10	22.94	22.81	22.74	23.11	22.64

Table 3.6 (continued)

	VS29_01	VS29_08	VS29_10	VS29_11	VS29_12	VS70_15	VS70_16	VS90_01	VS90_04
Si	2.83	2.83	2.94	2.95	2.91	2.83	2.82	2.78	2.85
^{IV}Al	1.17	1.17	1.06	1.05	1.09	1.17	1.18	1.22	1.15
^{IV}Sum	4.00	4.00	4.00	4.00	4.00	4.00	4.00	4.00	4.00
Ti^{4+}	0.40	0.38	0.20	0.17	0.22	0.41	0.41	0.39	0.38
^{VI}Al	0.39	0.42	0.15	0.14	0.15	0.39	0.39	0.33	0.39
Fe^{2+}	1.05	1.09	0.36	0.26	0.35	1.05	1.05	1.11	1.09
Mg	1.29	1.29	2.43	2.48	2.37	1.32	1.32	1.30	1.30
Cr	0.02	0.01	0.01	0.08	0.05	0.01	0.01	0.01	0.01
V^{3+}	0.03	0.02	0.01	0.01	0.01	0.02	0.02	0.02	0.02
Mn^{2+}	-	-	-	-	-	-	-	-	-
Li	0.02	0.01	-	-	-	0.01	0.01	0.02	0.02
^{VI}Sum	3.18	3.21	3.16	3.14	3.15	3.20	3.20	3.16	3.19
K	0.93	0.92	0.96	0.94	0.96	0.94	0.95	0.94	0.94
Na	0.06	0.07	0.02	0.01	0.02	0.06	0.06	0.06	0.06
Ba	0.01	0.01	0.01	0.01	0.01	0.01	-	0.01	0.01
^{XII}Sum	1.02	1.01	0.99	0.96	0.99	1.02	1.02	1.03	1.03
OH	0.33	0.29	0.88	0.92	0.78	0.36	0.33	0.31	0.19
F	0.22	0.25	0.30	0.34	0.37	0.15	0.20	0.45	0.38
O	11.45	11.46	10.82	10.74	10.85	11.49	11.47	11.24	11.43
Charge (+)	23.46	23.48	22.83	22.77	22.86	23.50	23.48	23.28	23.45
Charge (-)	23.45	23.46	22.82	22.74	22.85	23.49	23.47	23.24	23.43

Table 3.7 Atomic ratios calculated on the basis of Σ (octahedral+tetrahedral cations)=7

	VDA3_X	VDA3_XI	MVC100_02	MVC100_04	ORC1_01	ORC1_02	ORC1_03	SIS50_02	SIS50_07
Si	2.96	2.99	2.93	2.99	2.88	2.92	2.89	2.97	2.97
^{IV}Al	1.05	1.02	1.07	1.01	1.11	1.07	1.08	1.03	1.03
^{IV}Sum	4.00	4.00	4.00	4.00	3.99	3.99	3.97	4.00	4.00
Ti^{4+}	0.08	0.07	0.07	0.08	0.45	0.45	0.43	0.33	0.21
^{VI}Al	-	0.01	0.03	0.02	-	-	-	-	0.02
Fe^{2+}	0.16	0.15	0.24	0.18	0.58	0.68	0.50	0.60	0.22
Mg	2.69	2.71	2.58	2.68	1.93	1.84	2.05	2.05	2.51
Cr	0.05	0.04	0.07	0.03	-	-	-	-	0.03
V^{3+}	-	-	-	-	0.01	0.01	0.01	-	0.01
Mn^{2+}	-	-	-	-	-	-	-	0.01	-
Li	0.01	0.01	0.01	0.01	0.04	0.03	0.04	0.01	-
^{VI}Sum	3.00	3.00	3.00	3.00	3.01	3.01	3.03	3.00	3.00
K	0.94	0.94	0.91	0.9	0.86	0.85	0.87	0.95	0.94
Na	0.01	0.01	0.04	0.05	0.07	0.06	0.05	0.01	0.01
Ba	-	-	-	-	0.05	0.05	0.05	0.01	-
^{XII}Sum	0.95	0.95	0.95	0.95	0.98	0.96	0.97	0.97	0.95
OH	1.25	1.28	0.82	0.94	0.32	0.55	0.39	0.63	1.01
F	0.30	0.28	0.97	0.96	0.73	0.64	0.87	0.24	0.34
O	10.45	10.44	10.21	10.10	10.95	10.81	10.74	11.13	10.65
Charge (+)	22.12	22.13	22.11	22.14	22.77	22.80	22.71	22.60	22.40
Charge (-)	22.45	22.44	22.21	22.10	22.95	22.81	22.74	23.13	22.65

Table 3.7 (continued)

	VS29_01	VS29_08	VS29_10	VS29_11	VS29_12	VS70_15	VS70_16	VS90_01	VS90_04
Si	2.75	2.75	2.87	2.90	2.85	2.75	2.74	2.72	2.77
^{IV}Al	1.25	1.25	1.13	1.10	1.15	1.25	1.26	1.28	1.23
^{IV}Sum	4.00	4.00	4.00	4.00	4.00	4.00	4.00	4.00	4.00
Ti^{4+}	0.38	0.37	0.20	0.16	0.22	0.40	0.40	0.38	0.37
^{VI}Al	0.27	0.29	0.06	0.07	0.06	0.26	0.26	0.23	0.26
Fe^{2+}	1.02	1.05	0.35	0.25	0.35	1.02	1.02	1.08	1.06
Mg	1.26	1.25	2.37	2.43	2.31	1.28	1.28	1.26	1.26
Cr	0.02	0.01	0.01	0.08	0.05	0.01	0.01	0.01	0.01
V^{3+}	0.03	0.02	0.01	0.01	0.01	0.02	0.02	0.02	0.02
Mn^{2+}	-	-	-	-	-	-	-	-	-
Li	0.02	0.01	-	-	-	0.01	0.01	0.02	0.02
^{VI}Sum	3.00	3.00	3.00	3.00	3.00	3.00	3.00	3.00	3.00
K	0.90	0.90	0.94	0.92	0.94	0.91	0.92	0.92	0.92
Na	0.06	0.07	0.02	0.01	0.02	0.06	0.06	0.06	0.05
Ba	0.01	0.01	0.01	0.01	0.01	0.01	-	0.01	0.01
^{XII}Sum	0.97	0.98	0.97	0.94	0.97	0.98	0.98	0.99	0.98
OH	0.32	0.28	0.86	0.90	0.76	0.35	0.32	0.31	0.19
F	0.21	0.24	0.29	0.34	0.36	0.15	0.19	0.44	0.37
O	11.47	11.48	10.85	10.76	10.88	11.50	11.49	11.25	11.44
Charge (+)	22.79	22.79	22.33	22.33	22.39	22.82	22.80	22.72	22.77
Charge (-)	23.47	23.48	22.85	22.76	22.88	23.50	23.49	23.25	23.44

Table 3.8 Mössbauer parameters obtained by the QSD fitting method

	X^2_r	Species	δ_0(mm/s)	A^-/A^+	ΔE_q(mm/s)	σ	P (%)	A (%)
VDA3	0.64							
		$^{VI}Fe^{2+}$	1.115(6)	1.29(2)	2.55(2)	0.25(5)	78.4*	77(2)
					2.1(9)	0.4(3)	21.6(4)	
		$^{VI}Fe^{2+}$	0.33(7)	1*	0.9(1)	0.7(1)	100*	23(2)
MVC100	0.89							
		$^{VI}Fe^{2+}$	1.107(7)	1.23(1)	2.43(3)	0.245(5)	47.0*	75(1)
					2.17(12)	0.44(5)	53.0(2)	
		$^{VI}Fe^{2+}$	0.41(4)	1*	0.97(7)	0.51(4)	100*	25(1)

Notes: χ^2_r = reduced χ^2 = χ^2 /degrees of freedom; δ = centre shift, $\delta = \delta_0 + \delta_1 \Delta E_Q$, δ_1=0 during fitting; A^-/A^+ = ratio between low- and high-velocity spectral areas of the Mössbauer doublets; ΔE_Q = quadrupole splitting and position of the individual Gaussian component to the QSD; σ = width of the individual Gaussian component to the QSD; P = portion of the individual Gaussian component to the QSD. * Fixed parameters

4 Discussion

4.1 Ideal mica structure and main distortion parameters

The ideal mica structure can be described as a sandwich consisting of two tetrahedral *sheets* pointing to each other with one edge-sharing octahedral sheet interposed between them (Fig. 4.1a). The ensemble of linked sheets is referred to as *layer*. Layers are negatively charged and are then compensated by large interlayer cations that bond the layers together. Tetrahedra are linked together by sharing three *basal* oxygens (O_{basal}) forming an hexagonal pattern; the fourth corner, the *apical* oxygen (O_{apical}), points in the direction normal to the layer and links the octahedral sheet (Fig. 4.1b).

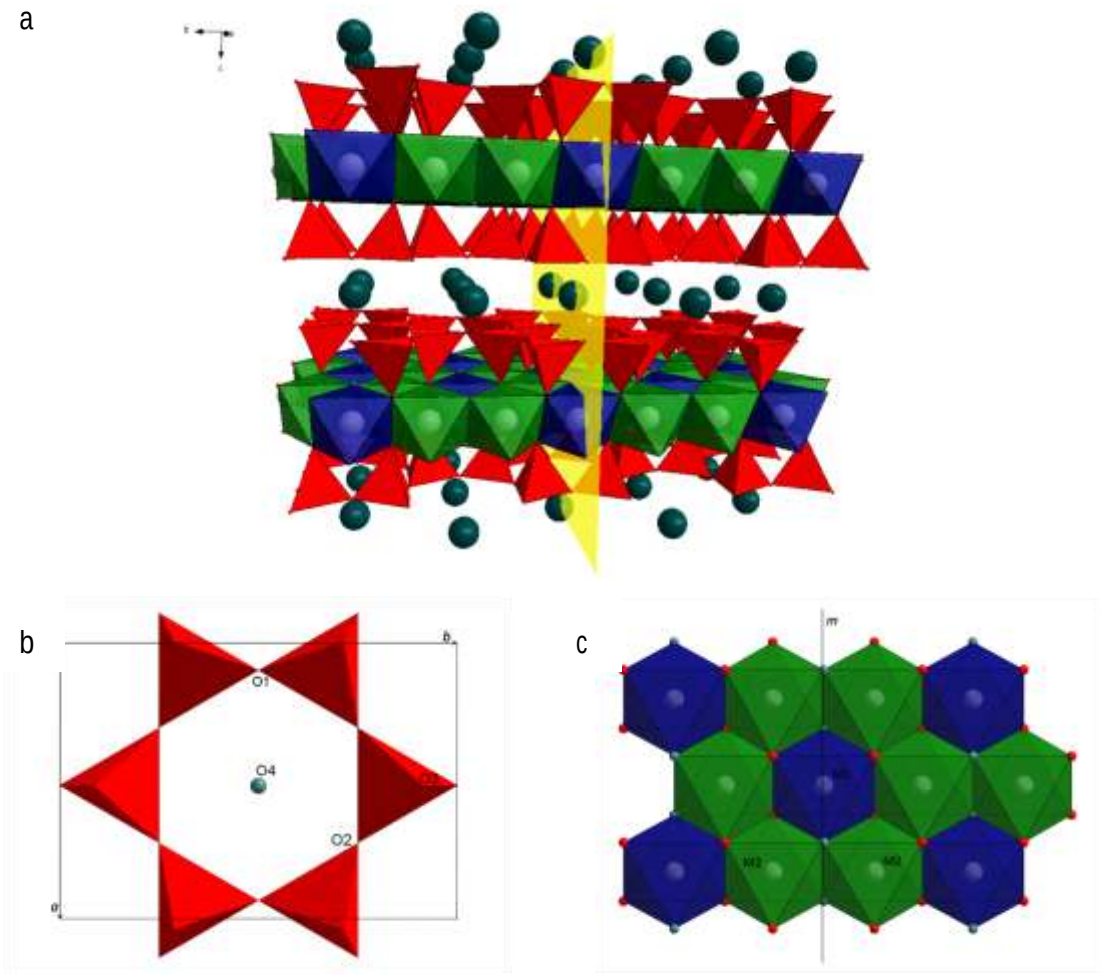

Figure 4.1. a) the T-O-T layer, M1 and M2 in blue and green, respectively; the mirror plane is represented in yellow; Interlayer cations in dark green. b) the hexagonal tetrahedral ring. c) the octahedral layer.

The octahedral sheet is then completed by unshared anions (usually indicated as "OH" anions, although their composition may vary) positioned at the centre of the hexagonal tetrahedral rings on the apical oxygens plane. Note that the plane formed by apical oxygens and "OH" anions is shifted by *a*/3 with respect to its counterpart in the sheet below. The *structural unit*,

consisting of the mica layer plus the interlayer cation, has monoclinic symmetry with space group *C*2/*m*. In general, assuming no distortion in the oxygen array, the following relationships for unit-cell parameters can be outlined: $b = a\sqrt{3}$; $\cos\beta = -a/3c$ (Smith and Yoder, 1956).There are two different kinds of octahedra with respect to the mirror plane: the one on the mirror plane, with "OH" atoms on opposite sides is called *trans-site* (M1), while the one lying outside, with "OH" atoms on adjacent corners, is called *cis-site* or (M2) (Fig. 4.1c). However there are several cases which exhibit ordering of octahedra, lowering the symmetry to *C*2 (e.g. Guggenheim and Bailey, 1977; Backhaus, 1983; Brigatti et al., 2000b; this study, paragraph 5.2).

Depending on how many of the octahedral sites are filled, micas are named *dioctahedral*, or *trioctahedral*; note that many micas show an intermediate character, although a complete solid solution between di-and tri-octahedral micas has not been observed. Moreover, when the interlayer positions are filled with monovalent cations micas are defined *true,* while, in case the cations is divalent, they are called *brittle*.

Many deviations from this ideal structure are found in "real" cases. To better understand how and why these "irregularities" occur, here is presented a brief summary about distortions in micas as well as a description of the main parameters describing them.

The principal cause of distortion is the fact that usually, depending on their chemical composition, tetrahedral and octahedral sheets present very different "lateral" dimensions. This misfit is quantified by the relationship found by Toraya (1981) Δ_{TM} = dimensional misfit = $2\sqrt{3} \langle O\text{-}O \rangle_{basal} - 3\sqrt{2} \langle M\text{-}O \rangle$. To accommodate this misfit, three main mechanisms usually occur. The most effective is undoubtedly the rotation of tetrahedra around [001], which lowers the symmetry of the tetrahedral ring from hexagonal to trigonal and reduces the dimension of the tetrahedral sheet on the (001) plane. The parameter expressing the tetrahedral rotation is α, which can be calculated, according to Hazen and Burnham (1973), as $\tan(\alpha) = 4\sqrt{3}*(1/4 - y_{O1})$. Another distortion balancing this misfit, although to a minor extent compared to the ditrigonalization of the tetrahedral layer, is the elongation/flattening of tetrahedra, which leads to a variation of tetrahedral basal edges; this mechanism is quantified by the parameter $\tau(°)$, calculated as the variation of the measured $\langle O_{basal}\text{-}T\text{-}O_{apical} \rangle$ with respect to the ideal value (109.28°). Δz is the parameter describing the corrugation of the basal oxygen plane, i.e. the tilting of tetrahedra and can be calculated as the difference between the basal oxygens *z* coordinate multiplied by $c\sin\beta$. Flattening of octahedra is another mechanism able to reduce the dimensional misfit. This mechanism is measured by the angle ψ between the [001] direction

and the principal diagonal of the octahedron (54.44 ° in undistorted octahedra) and can be calculated, according to Takeda (1981), as $\psi = \cos^{-1}(t_{oct}/ 2\langle M\text{-}O\rangle)$, where t_{oct} is the thickness of the octahedral layer (see *notes* in Table 3.3 for calculation). Note that among the described mechanisms that reduce Δ_{TM}, α is by far the most effective one. This is not surprising, since if the energy associated with tetrahedral rotation is low compared to that necessary to modify other parts of the structure.

Obviously, structural deformations occur also as a consequence of the different nature of cations occupying the polyhedra. This is true in particular for octahedra, which show a remarkable chemical variability. Other than parameters such as Angle Variance (AV) and Quadratic Elongation (QE) (Robinson et al., 1971) other parameters are commonly used to describe distortion in micas: Bond Length Distortion (BLD) is a measure of the distortion of bond lengths of a polyhedron, calculated comparing individual cation-anion distances with their average length. Edge Length Distortion (ELD) parameter is analogous to BLD but takes into account polyhedral edges instead of bond lengths; both BLD and ELD were defined by Griffen and Ribbe, (1979) for tetrahedral distortions and were then applied by Kunz et al., (1991) to octahedra. Other parameters, useful to describe specific crystal-chemical mechanisms leading to structural distortions are described in detail in the discussion.

4.2 Mica polytypes

As already pointed out, tetrahedral sheets have an hexagonal or a trigonal symmetry. It is then possible that they stack upon each other with different orientation; in other words, the stacking vector is free to point in six different directions from layer to layer. If the sequence of stacking directions is periodic, then the periodicity along [001] will increase, forming different *polytypes.* Polytypes are usually indicated as *n*_[ ], where *n* is the number of layers in the unit-cell of the polytype, _ represents the crystal system of the polytype and [ ] lists the number of 60°-rotation (+ or – for anti-clockwise and clockwise rotation respectively) between stacking vectors of consecutive layers.

The six "standard" polytypes defined by Smith and Yoder (1956) are 1*M*[0], 2M_1[2$\bar{2}$], 2M_2[1$\bar{1}$], 2*O*[33], 3*T*[222], and 6*H*[111111] (Fig. 4.2) and, since they are only six, with unambiguous angular sequences, the angular portions are usually omitted. Assuming that all polytypes are composed of the ideal 1*M* layer, resulting space groups are then *C*2/*m*, *C*2/*c*, *C*2/*c*, $P3_121$(or

$P3_112$) and $P6_122$ ($P6_522$) or , respectively for 1*M*, 2M_1, 2M_2, 2*O*, 3*T*, and 6*H*. However, many many cases of symmetry lowering from this ideal space groups are reported in the literature (e.g. Takeda and Ross, 1975; Swanson and Bailey, 1981; Ohta et al., 1982; Lin and Guggenheim, 1983; Lahti and Saikkonen, 1985; Slade et al., 1987; Rieder et al.1996; Scordari et al., 2012b). Generally 2M_1 polytype is the most abundant among dioctahedral micas, while 1*M* is the most represented in the trioctahedral group (Bailey, 1984).

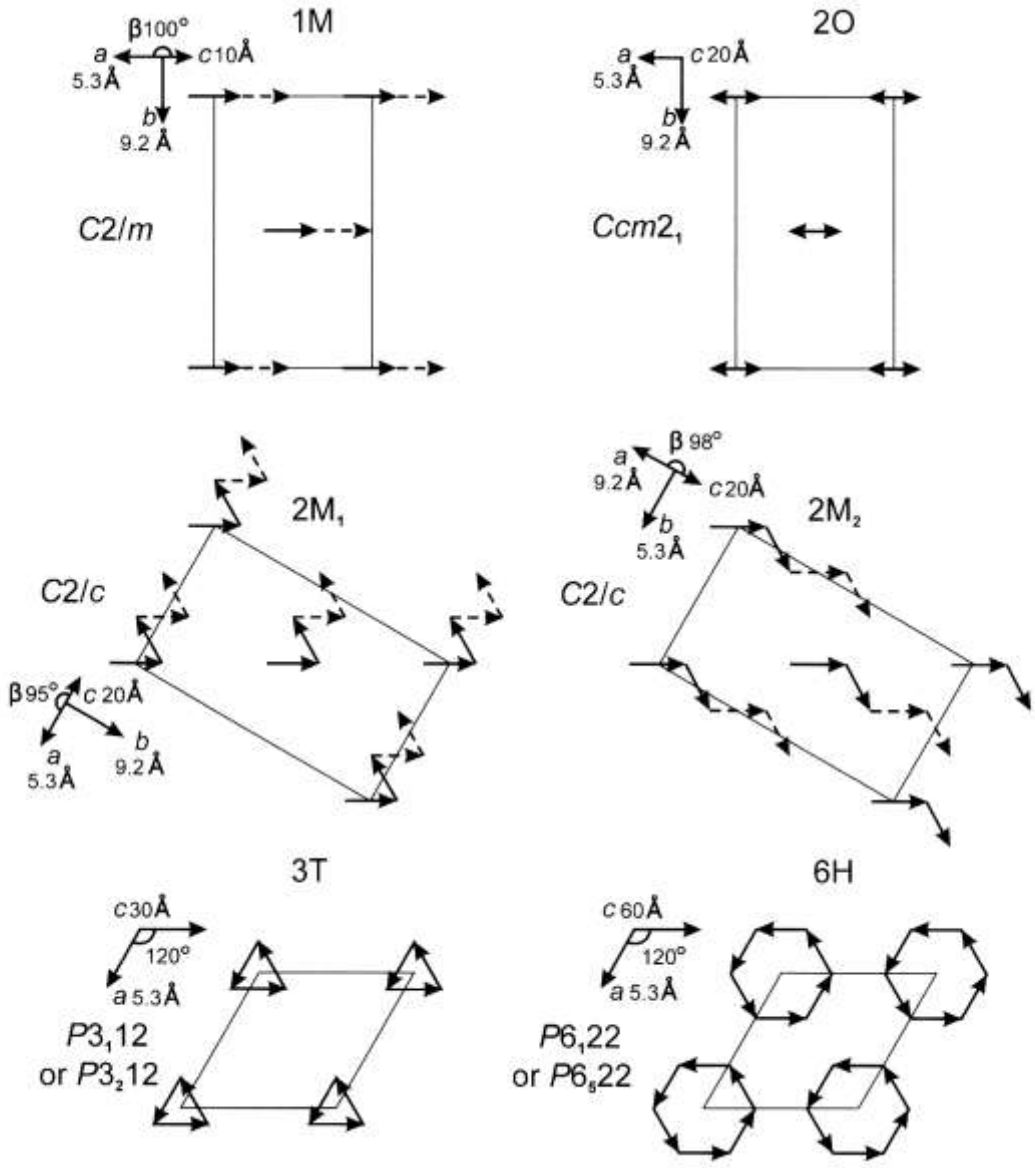

Figure 4.2. The six "standard" ways of stacking mica layers in an ordered manner. The arrows represent the stacking vectors. Full line vectors show the layer stacking in one unit-cell, whereas the broken line vectors show the positions of layers in the next unit-cell. The base of the unit-cell is shown by thin lines, and the space group and lattice parameters are listed by the side of the diagram (after Smith and Yoder, 1956).

4.3 Considerations on chemical composition

Trends and correlations between elements in micas stem from a complex and mutual control of both the structural characteristics of the mineral and the chemistry of the host rock.

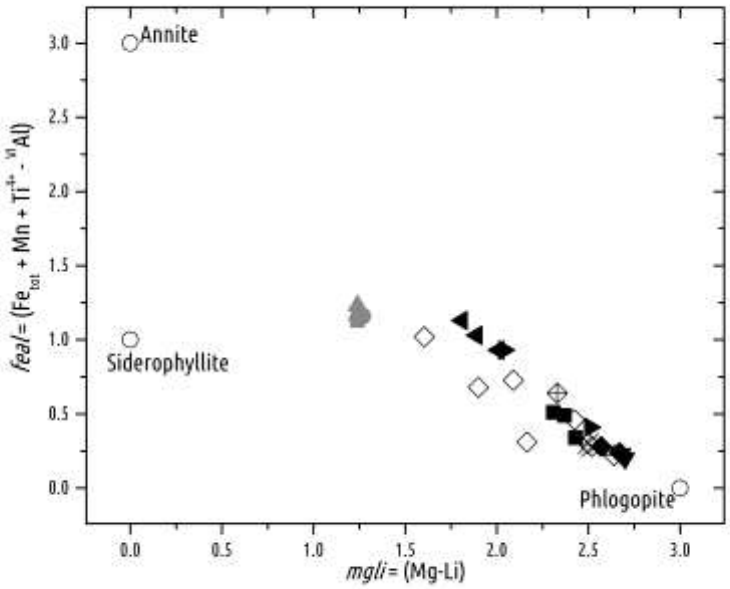

Figure 4.3. *feal*s. *mgli* classification plot modified after Tischendorf et al. (2007). Symbols: black and grey solid symbols: phlogopites from lamproitic rocks from this study belonging respectively to 1*M* and 2M_1 polytypes (squares= VS29; circles= VS70; upward triangles= VS90; downward triangles= VDA3; diamonds= MVC100; leftward triangles= ORC1; rightward triangles= SIS50); open diamonds = phlogopites from lamproitic rocks from the literature (empty diamonds= Brigatti et al., 1991; diamonds with horizontal line= Schingaro et al., 2014; diamonds with plus= Brigatti and Poppi, 1993; diamonds with cross= Cruciani and Zanazzi, 1994); empty circles= ideal phlogopite, annite and siderophyllite end-members.

From a chemical point of view, studied micas, lie on the join between phlogopite and annite (Fig. 4.3) with studied samples (solid symbols) plotted together with other phlogopite crystals from worldwide lamproitic rocks; we note a syderophyllitic component for the 2M_1 micas from Torre Alfina (grey symbols), owing to their high Al content. In Figure 4.4 the representation in terms of the "ideal biotite plane" (Guidotti, 1984) is shown; here is as well evident how 2M_1 micas from Torre Alfina lie in quite a different compositional field compared to the other studied samples. They show in particular a strong enrichment in Al and a less primitive character, as testified by the lower Mg#, which is quite anomalous for lamproitic phlogopite. The variable but often very high values of Ti (Fig. 4.5) are instead typical of phlogopite with lamproitic provenance even though, also in this graph, 2M_1 micas cluster separately from the other crystals.

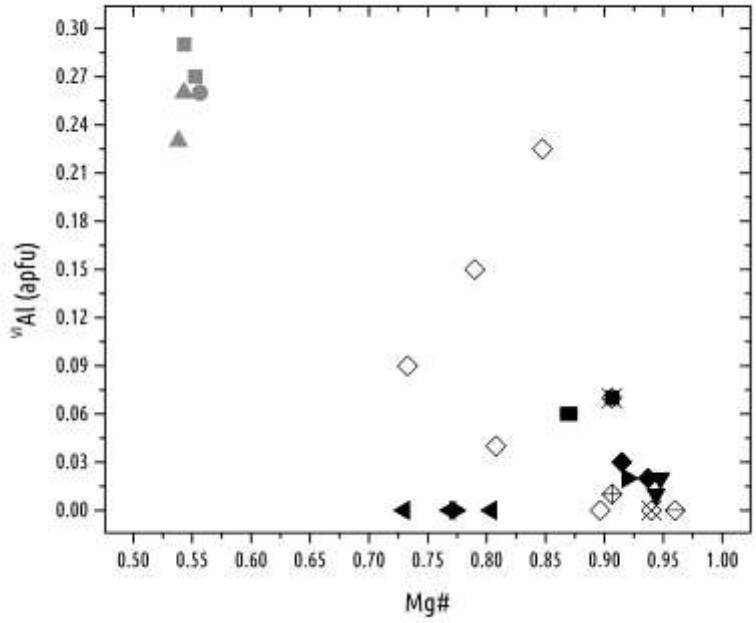

Figure 4.4. Plot of ^{VI}Al vs. Mg# = [Mg/(Mg+Fe_{tot})], known as "ideal biotite plane", for the studied micas and other phlogopites from lamproites from the literature. Symbols as in Figure 4.3

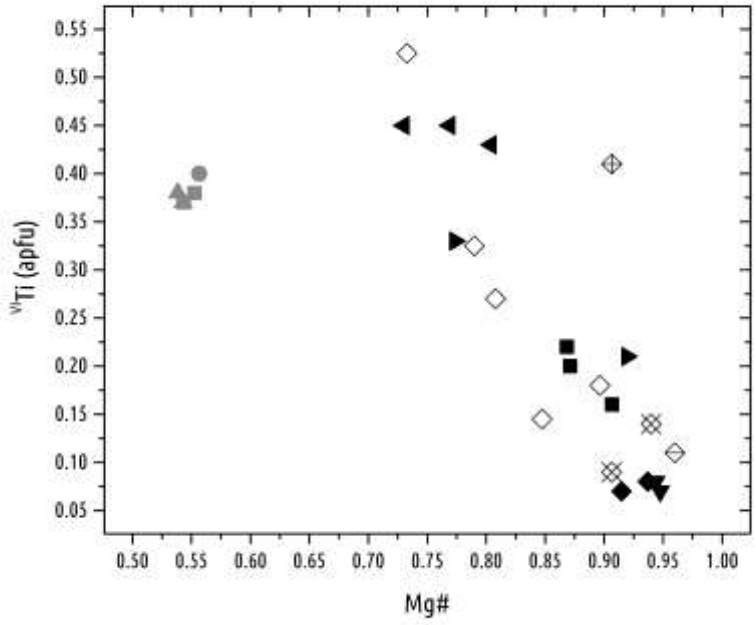

Figure 4.5. Plot of Ti content vs. Mg# for the studied micas and other phlogopites from lamproites from the literature. Symbols as in Figure 4.3

Studied phlogopite crystals show variable but generally high amounts of fluorine that can reach up to ~ 1 apfu (Fig. 4.6). Edgar and Charbonneau (1991) and Edgar et al. (1996) already

pointed out how fluorine content in lamproitic phlogopite is typically 3-4 times higher compared to other micas from ultrapotassic rocks; they found that, in minerals from ultrapotassic rocks, F usually decreases with the increasing degree of evolution of the host rock. This general trend is confirmed for many of the studied samples; the observed scattering of data can be due to other factors such as variable H_2 and F activity coefficients (a_{H_2} and a_F) in the melt from which the minerals crystallized.

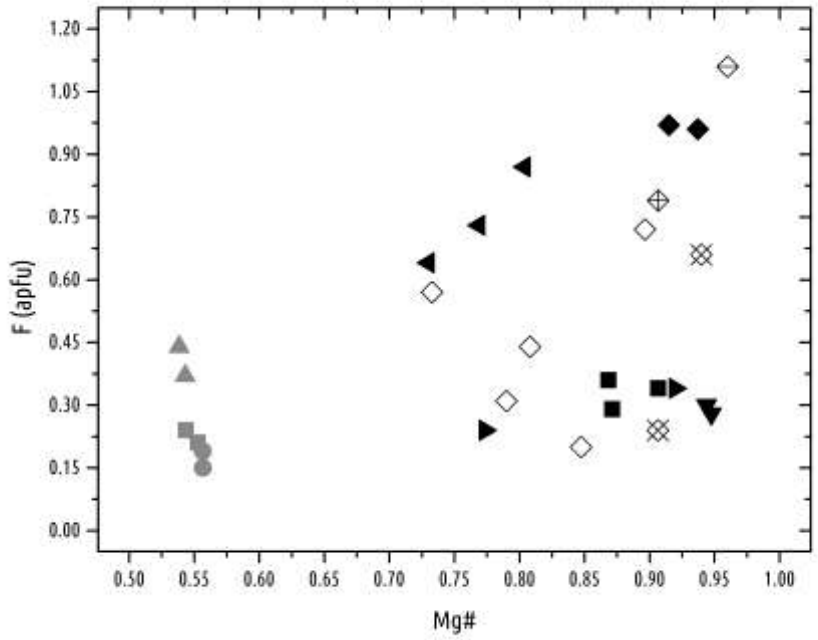

Figure 4.6. Plot of F content vs. Mg# for the studied micas and other phlogopites from lamproites from the literature. Symbols as in Figure 4.3

Figure 4.7 shows the relationship between the contents of Al and Si: the general decrease of the total content of Al with increasing Si is compatible with a $M^{3,4+}$-Tschermak substitution. A component of $M^{3,4+}$-Tschermak substitution is also observable in Figure 4.8 where the sum of octahedral tri- and tetra-valent cations shows a general increase with the increase of tetrahedral Al. However, it is possible to note that for some samples this trend is not observed. This difference is even more evident when Al and Ti content are taken into account separately (Fig. 4.9a and b): specifically, for many of the samples the ^{IV}Al content does not vary with increasing Ti, while for Torre Alfina micas the increase of incorporation of Ti in the octahedra corresponds to a certain degree of Al for Si substitution in the tetrahedra. The same applies to the Al content in octahedra for all the studied samples, which shows a clear linear correlation with the increase of Al in tetrahedra.

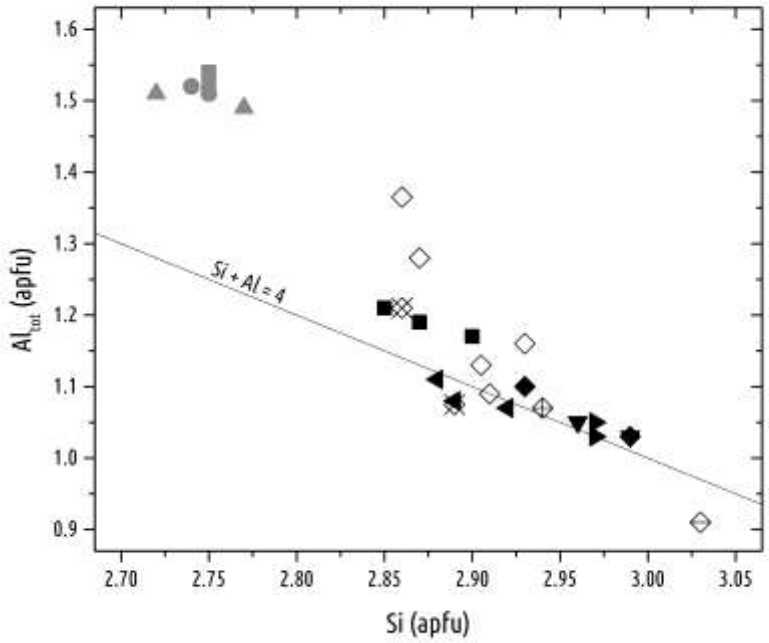

Figure 4.7. Variation of Si content with respect to the total Al content. Symbols as in Figure 4.3

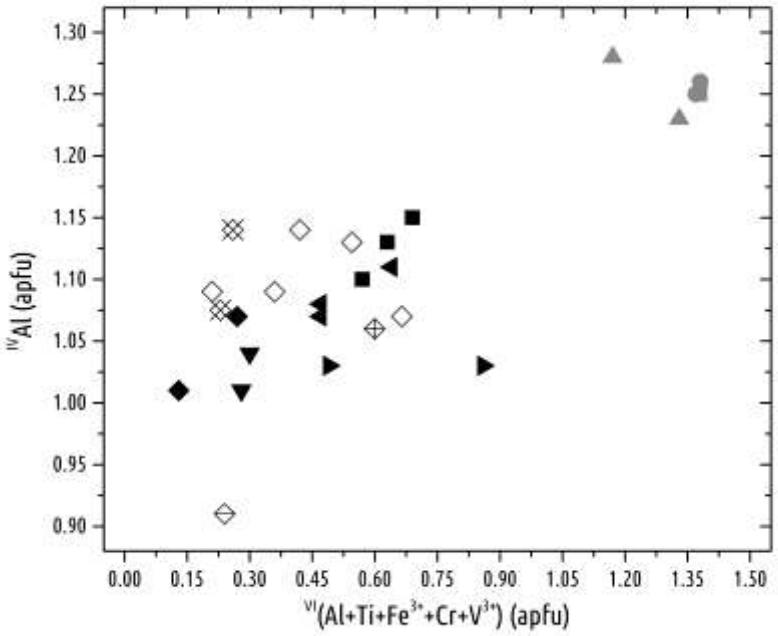

Figure 4.8. Relationship between the tetrahedral Al content and the sum of octahedral tri- and tetra-valent cations. Symbols as in Figure 4.3

Nonetheless, if we plot the total content of tri- and tetra-valent cations in octahedra against the *oxy* component [2-(OH+F); Fig. 4.10], we observe that all the studied crystals show a strong correlation between these two parameters, indicating that the increase of O^{2-} at O4 site,

more than the Al for Si substitution in tetrahedra, balances the increase of tri- and tetra-valent octahedral cations. If we focus our attention on the relationship between Ti and the *oxy* component (Fig. 4.11) we notice that there is another substitutional mechanism involving samples from Orciatico.

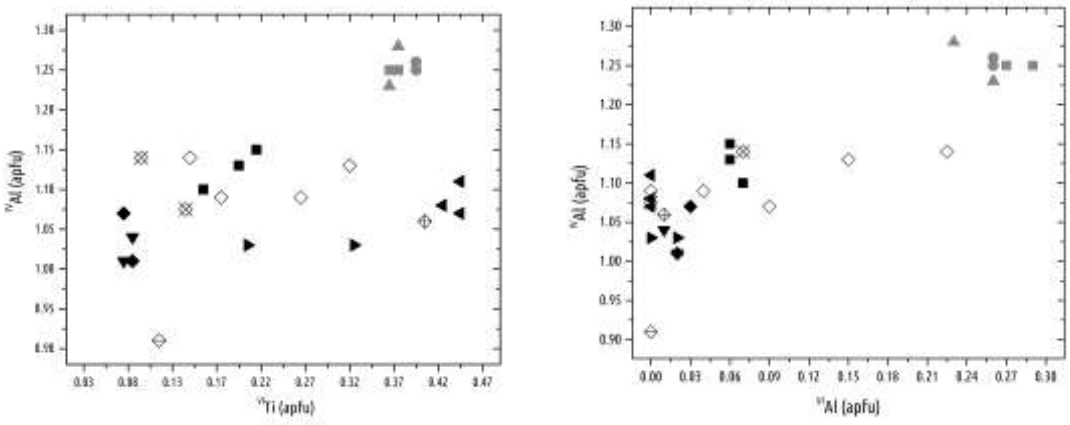

Figure 4.9. Relationship between tetrahedral Al content and octahedral Ti (a) and Al (b) content. Symbols as in Figure 4.3

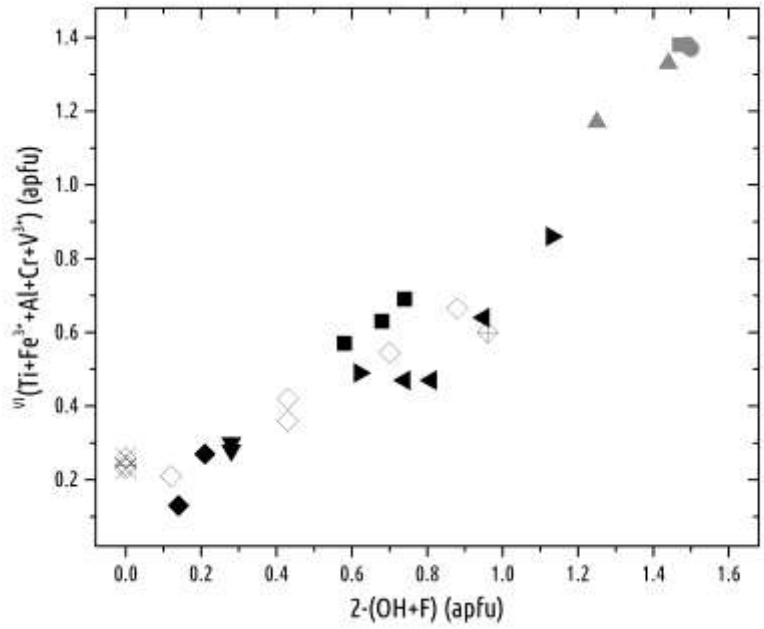

Figure 4.10. Relationship between the sum of octahedral tri- and tetra-valent cations and the *oxy* component at O4 site. Symbols as in Figure 4.3

We can recognize that Orciatico micas have much higher Ti content compared with other samples with the same degree of "oxidation"; if this difference is ascribed to a Ti-Tschermak substitution, data in Figure 4.9 would then show a higher ^{IV}Al content; crystals from Orciatico lamproite show a slightly higher content of Ti compared to those showing no hints of a Ti-

Tschermak substitution; however, this increase is not marked enough to balance the very high content of Ti shown by these samples.

Since chemical data did not give any suggestion of the presence of structural vacancies in the octahedral sites, a possible explanation involves the presence of monovalent cations. Crystals from Orciatico lamproite have indeed Li-bearing phlogopite compositions (see Table 3.5) with Li content up to 0.04 apfu; a mechanism capable of explaining a contribute of this element in balancing the higher Ti content of these crystals could then be schematized as $3R^{2+} \leftrightarrow Ti^{4+} + 2Li^{+}$.

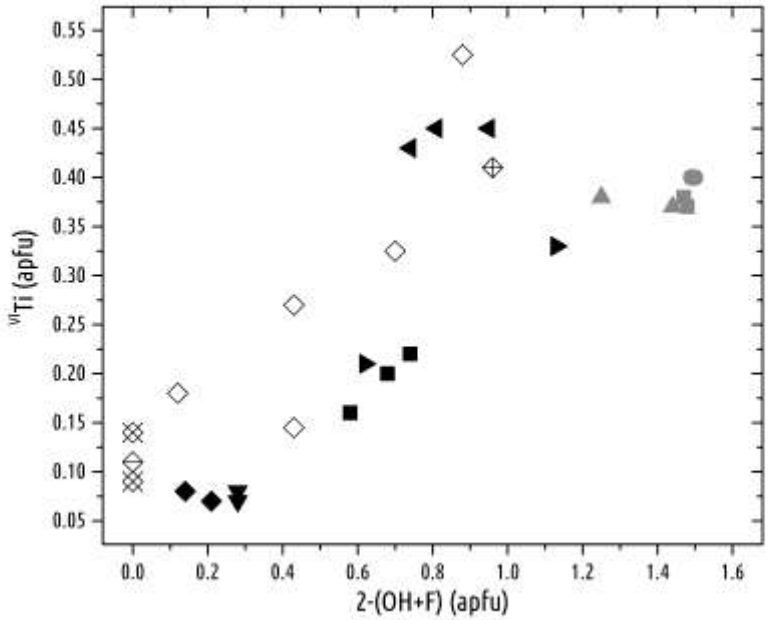

Figure 4.11. Relationship between octahedral Ti content and the *oxy* component at O4 site. Symbols as in Figure 4.3

4.4 Lattice parameters

The correlation between *a* and *b* cell parameters is in agreement, within a certain approximation, to the *ideal* dependence defined as $b = a\sqrt{3}$ (Fig. 4.12).

Observing the behavior of *a* and *b* parameters, together with those of phlogopite crystals from lamproites worldwide, *versus* the average <M-O>and <T-O>distances (Fig. 4.13 and 4.14), we do not recognize any effect of octahedral and tetrahedral mean bond lengths over the *a* and *b* lateral dimension.

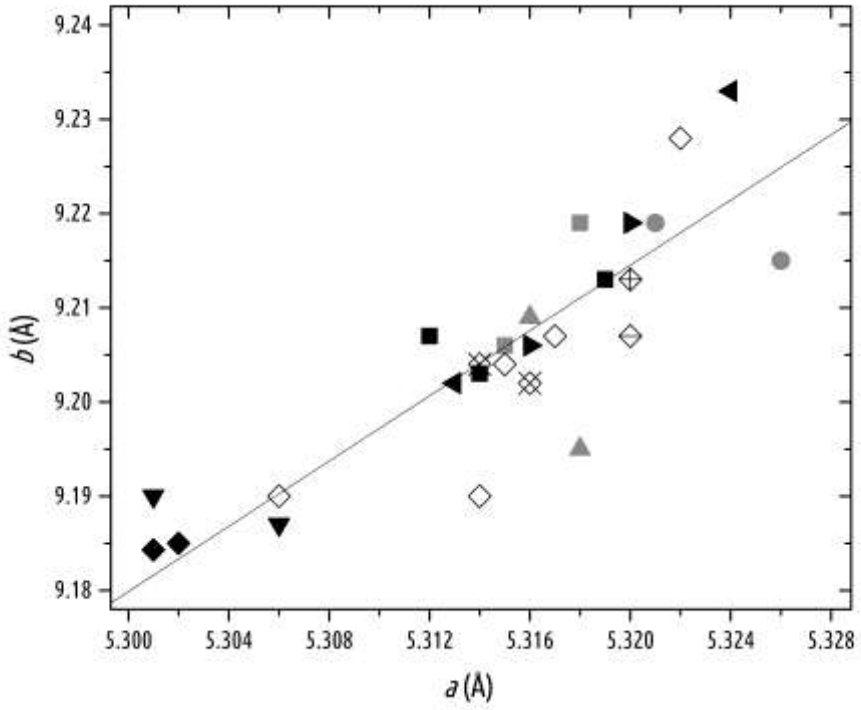

Figure 4.12. *a* vs. *b* cell parameters relationship compared to the "ideal" $b=a\sqrt{3}$. Symbols as in Figure 4.3

Considering their high content of small Al and Ti cations, 2*M*$_1$ samples show relatively high *a* and *b* parameters, probably because of the deformations that follow the incorporation of such small and highly charged cations that yield the octahedral layer to increase its "lateral" dimensions (see paragraph 4.7).

"Lateral" cell dimensions are, with the exception of 2*M*1 samples from Torre Alfina, consistent with the relationship found by Cruciani and Zanazzi (1994) with Mg fraction (a = 5.368(3) – X_{Mg}*6.3(6)*10^{-2}, r^2=0.85; b= 9.308(5) - X_{Mg}*12.1(9)*10^{-2}, r^2=0.91,X_{Mg}= Mg/ ^{VI}total). The dependence of the *c* parameter on octahedral and tetrahedral composition, as known from literature (e.g., Hazen and Wones, 1972; Cruciani and Zanazzi, 1994; Schingaro et al., 2011), is very weak. The actual relationship existing between *c* length and the substitution for high-charge cations such as Ti (Fig. 4.15) is ascribed to the substitution mechanism through which octahedral cations are incorporated in the structure. Its variation indeed depends on the relationship between the interlayer cation and the O4 site (e.g. Giese, 1984; Cruciani and Zanazzi, 1994; Schingaro et al., 2011) and on the substitutions occurring at interlayer site. The relationship between *c* and the content of the O4 hydroxyl site is well known from literature (Cruciani and Zanazzi, 1994; Ventruti et al., 2008; Schingaro et al., 2011).

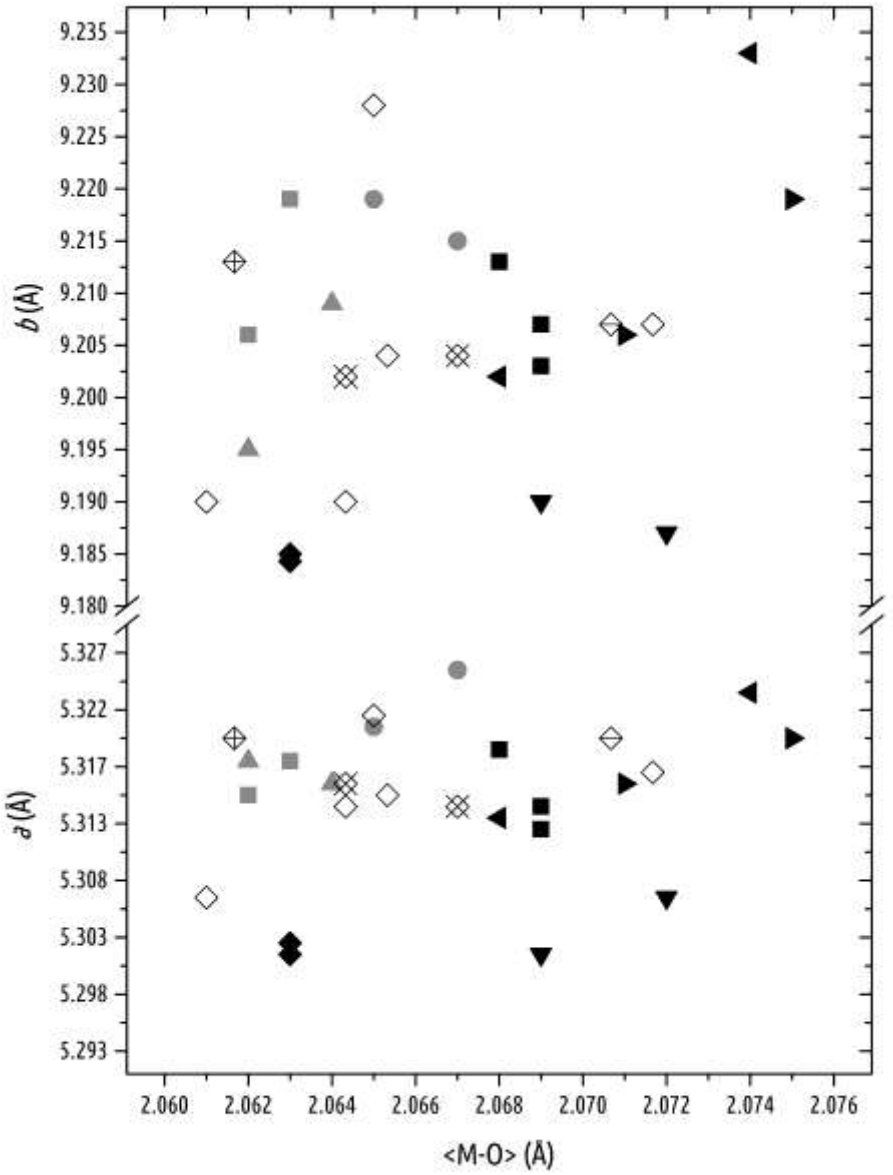

Figure 4.13. *a* and *b* cell parameters variations confronted with mean octahedral bond-length. Symbols as in Figure 4.3

Variations of *c* are indeed related to $OH^- \leftrightarrow F^-$ and $OH^- \leftrightarrow O^{2-}$ substitution mechanisms: in trioctahedral micas the O-H bond is directed approximately along [001] with the H atom pointing towards the interlayer cation (Giese, 1979). Deprotonation and/or incorporation of fluorine, as calculated by Giese (1984) for OH-phlogopite and fluorophlogopite on the basis of electrostatic potential energy calculations, result in a reduced repulsion between the cation in the interlayer site and the O4 site, which allows a variation of *c* in a wide interval, ranging from ~10.30 Å for end-member phlogopite to ~10.10 Å for H-deficient phlogopites and

fluorophlogopites (Ohta et al., 1982; Mesto et al., 2006; Scordari et al., 2008; Schingaro et al., 2011; Scordari et al., 2013; this study).

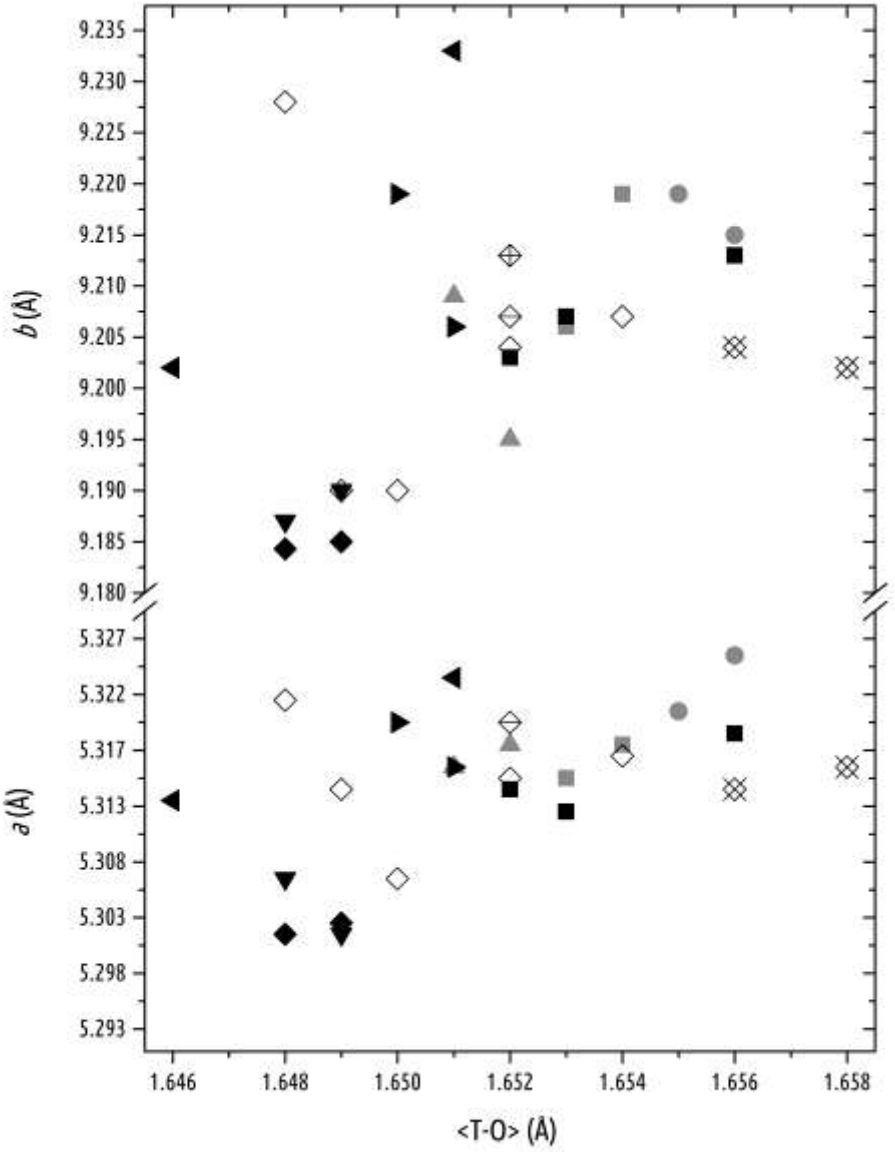

Figure 4.14. *a* and *b* cell parameters variations confronted with mean tetrahedral bond-lenght. Symbols as in Figure 4.3

Figure 4.16 shows the variation of tetrahedral, octahedral and interlayer thicknesses (t_{tet}, t_{oct} and t_{int}, respectively) plotted against the variation of $c\sin\beta$ ($1/2 * c\sin\beta$ for crystals belonging to the $2M_1$ polytype) for samples from this study and from the literature. Octahedral and tetrahedral thicknesses show, as expected, no relationship with $c\sin\beta$, while the interlayer thickness shows a clear positive correlation with $c\sin\beta$. Low values of octahedral thickness for $2M_1$ phlogopite are another effect of the remarkable content of Al in the octahedra.

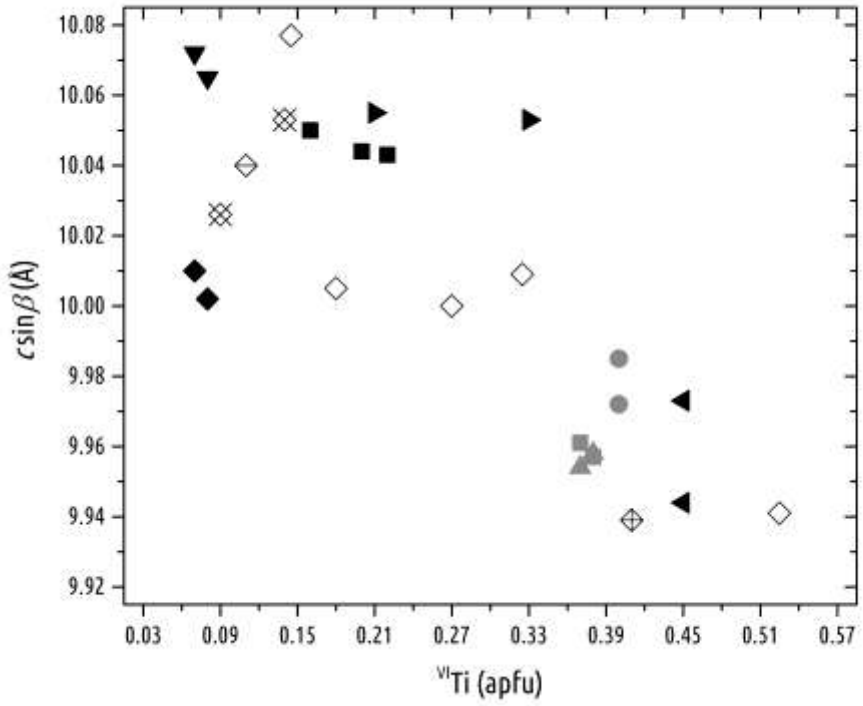

Figure 4.15. *c*sinβ variation with respect to Ti content. Symbols as in Figure 4.3

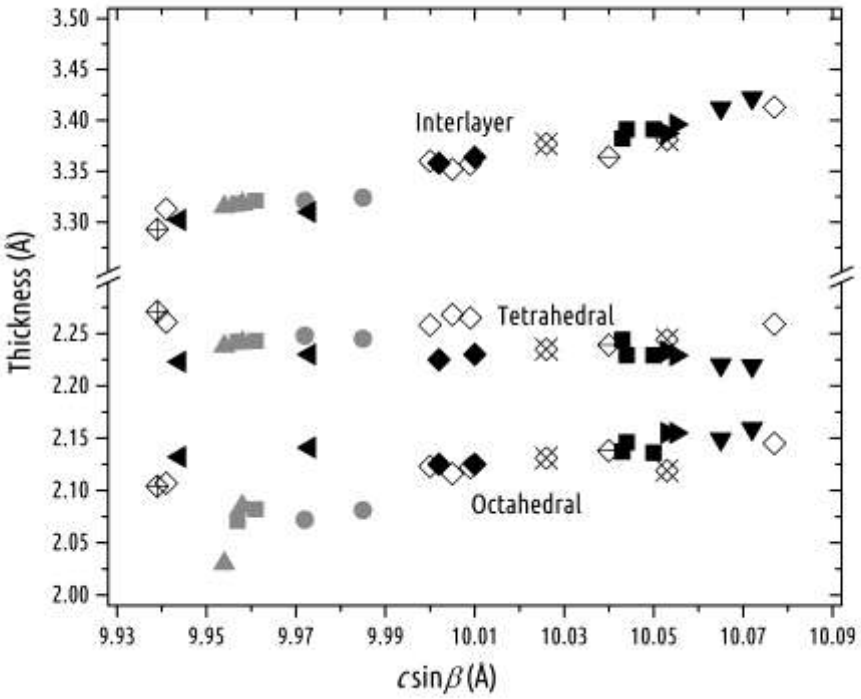

Figure 4.16. Thickness variation of individual mica sheets as a function of *c*sinβ. Symbols as in Figure 4.3

4.5 Indirect evaluation of water content

In Figure 4.17 the variation of the OH content is plotted against $c\sin\beta$ for data from this study and all the other phlogopite crystals from literature where the hydrogen content has been measured by SIMS and c measured by single-crystal X-ray diffraction. This relationship proves to be very helpful since it can efficiently be used for an indirect evaluation of the water content of phlogopite and it can therefore help to check for mistakes in H_2O measurements. The relationship found by Cruciani and Zanazzi (1994), calculated by regression analysis with data from Brigatti and Davoli (1990) and Brigatti et al. (1991), who measured H_2O content by thermogravimetric analysis, led to OH = 8.3(9)*c - 83.7(1) (r^2= 0.88) (dashed line in Fig. 4.17).

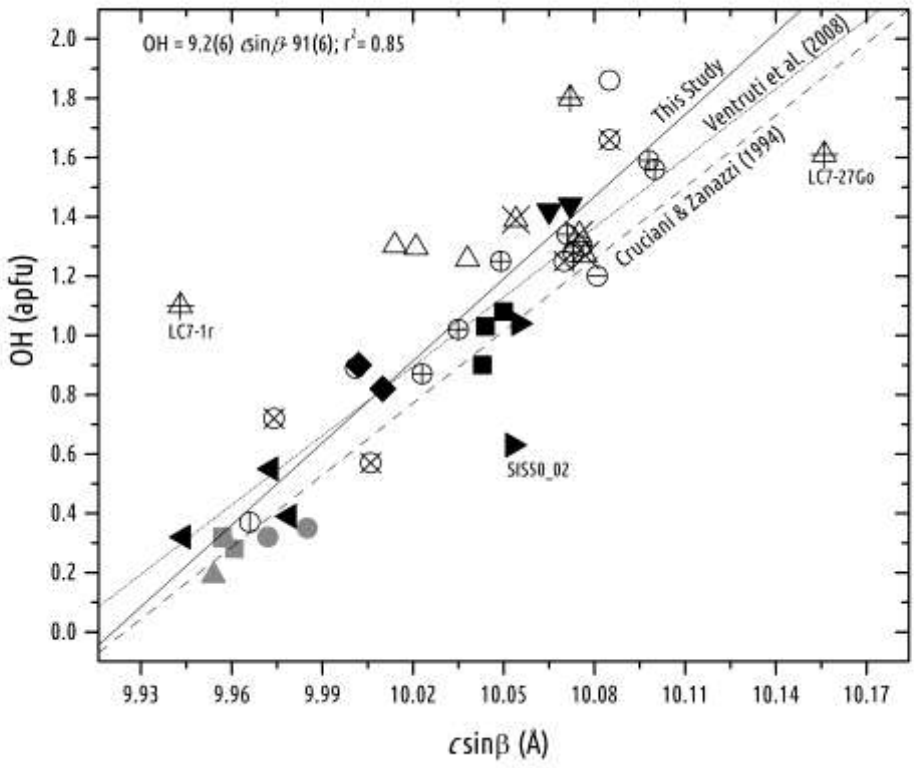

Figure 4.17. Relationship between the OH content and $c\sin\beta$ for phlogopites whose H content was measured by SIMS analysis. Solid symbols as in Figure 4.3 (for 2M_1 micas $c\sin\beta/2$ has been plotted). Empty circles= Matarrese et al., 2008; circles with plus= Scordari et al., 2010; circles with cross= Scordari et al., 2008; circles with horizontal line= Scordari et al., 2006; circles with horizontal line= Schingaro et al., 2011; empty upward triangles= Cesare et al., 2003; upward triangles with plus= Mesto et al. 2006; upward triangles with cross= Zema et al., 2010

Ventruti et al. (2008) calculated a slightly different relationship on the basis of few data from literature in which H_2O contents were determined with different analytical methods (e.g., C-H-N analysis, Scordari et al., 2006;SIMS, Matarrese et al., 2008; indirect evaluation on synthetic

samples, Redhammer and Roth, 2002), and they found a similar result with a slightly lower slope [c = 10.065(16) + 0.125(13) * OH (r^2= 0.97)] (dotted line in Fig. 4.17). Thanks to the recent availability of new data from this study and from the literature, a new linear regression equation was calculated using all the available data from SIMS analyses and single crystal X-ray diffraction; only three of the available 43 data-points were excluded from calculation. In particular, samples LC7-1R and LC7-27Go from Mesto et al. (2006) were omitted since, as the authors reported in the paper, they show hints of an unsatisfactory estimate of F and H; likewise, sample SIS50_02 from this study, which showed indications of an under-estimation of the H content, was not included in the regression analysis. The lengths of $c$sinβ and ½$c$sinβ respectively for 1M and 2M_1polytype were employed to allow the use of both the polytypes in the calculation. Regression analysis yielded to the relationship OH = 9.22 *$c$sinβ – 91.5 (r^2= 0.85) with an estimated error on the calculated OH value of about 14%. The equation from this study (solid line in Fig. 4.17) is steeper than the other two leading to some differences especially for samples with very short or long c parameters.

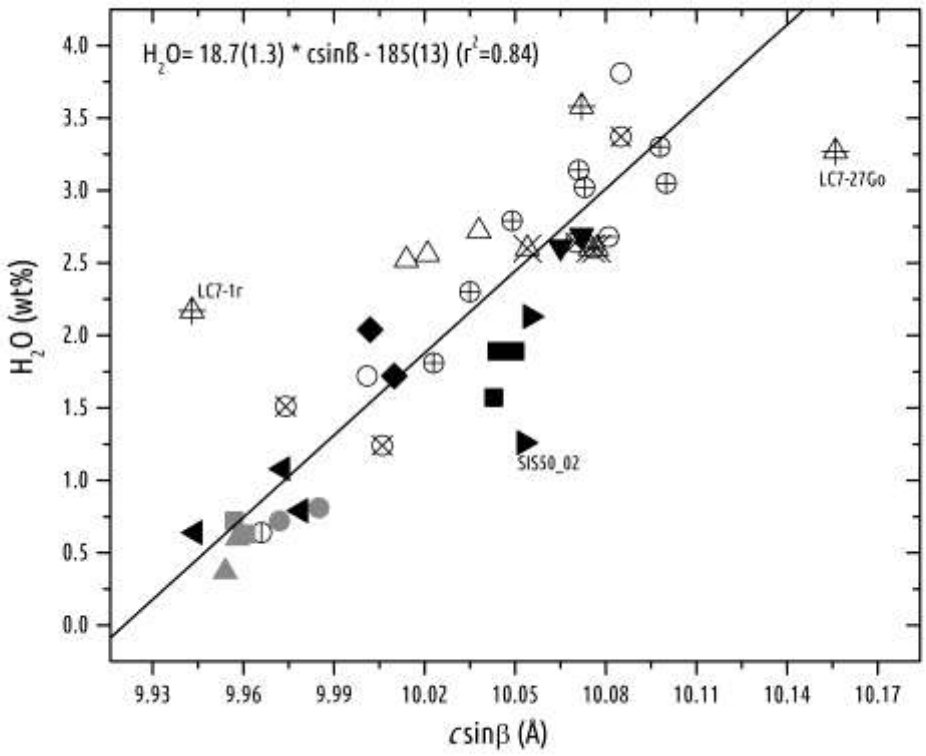

Figure 4.18. H_2O content (wt.%) plotted vs. $c$sinβ for phlogopites whose H content was measured by SIMS analysis. Symbols as in Figure 4.17 (for 2M_1 micas $c$sinβ/2 has been plotted).

Figure 4.18 shows the relationship between the H_2O content (wt%), directly derived from H determinations with SIMS for all the samples used for the calculation of the OH vs. $c\sin\beta$ correlation, and $c\sin\beta$. Although hypothesizing a relationship between c and H_2O content (wt%) is theoretically wrong, we can say that, examining the difference in molar weight between H_2O and the sum of the other oxides present in the samples, those values are nonetheless comparable. Micas examined in this study have a phlogopitic component spanning from ~90% down to ~50%; even assuming a full occupancy of O4 site by OH, the resulting variation of H_2O content (wt%), between the "lighter" phlogopitic term and the "heavier" annitic-richer one, would be about 0.32 wt.%. A new linear regression equation has been then determined, excluding the same data as in the previous calculation. It is evident that the spread of the H_2O content values along the correlation line is much greater than 0.32 (Fig. 4.18) allowing us to exploit this relationship. The resulting equation: H_2O (wt%) = 18.7(1.3) * $c\sin\beta$ - 185(13) (r^2=0.84), is certainly quite approximate since we can estimate a final uncertainty of about the 15% for the calculated H_2O contents; nonetheless it may indeed be useful, representing a quick tool to evaluate the water content. This information is crucial since very often phlogopite is assumed to be fully hydrated in routine analyses.

4.6 Tetrahedral sheet and interlayer site geometry

Tetrahedra in studied crystals are quite regular and follow the general trend of increasing <T-O> distance with the increase of ^{IV}Al content (Fig. 4.19). $2M_1$ samples, however, show a low <T-O> distance compared to the ^{IV}Al content. If we look at Tables 3.3 and 3.4, we note that tetrahedra are generally elongated parallel to $c\sin\beta$ as we can see from the τ values greater than 109.47°; $2M_1$ micas, on the contrary, always exhibit the lowest values among them while they show at the same time the highest volumes.

The τ value increases along with Si content in tetrahedra(Fig. 4.20), in good agreement with the relationship found by Brigatti and Guggenheim (2002). In Figure 4.21, τ values are plotted against the displacement of the tetrahedral cation from its ideal position (T_{disp}); $2M_1$ phlogopite crystals from Torre Alfina have much lower τ and T_{disp} values than $1M$ crystals. On the other hand they show much higher BLD_T values, while TQE, and especially TAV values, are lower than the others (Table 3.3 and 3.4). The high BLD and low τ values for these samples are explained by the very long T-O_{apical} distances compared to short T-O_{basal} bonds (Table 3.2).

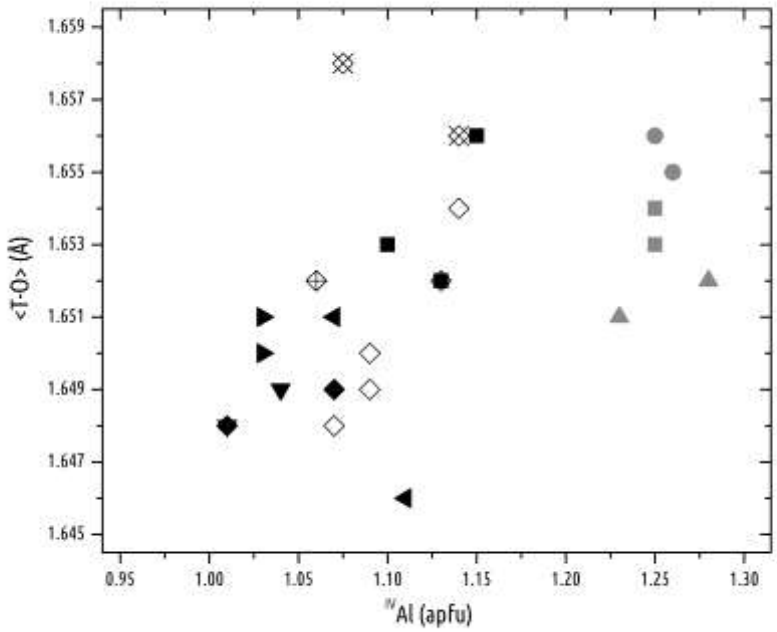

Figure 4.19. Variation of the average T-O bond distance as a function of the ^{IV}Al content. Symbols as in Figure 4.3

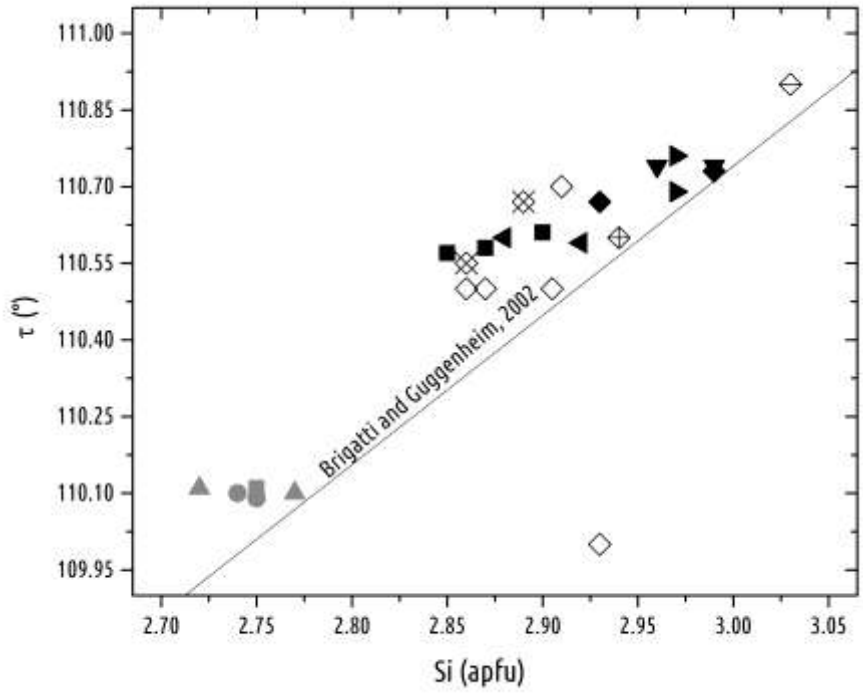

Figure 4.20. Relationship between τ and Si tetrahedral content. Regression line after Brigatti and Guggenheim (2002): τ = 2.920 * Si + 101.98 (r = 0.950). Symbols as in Figure 4.3

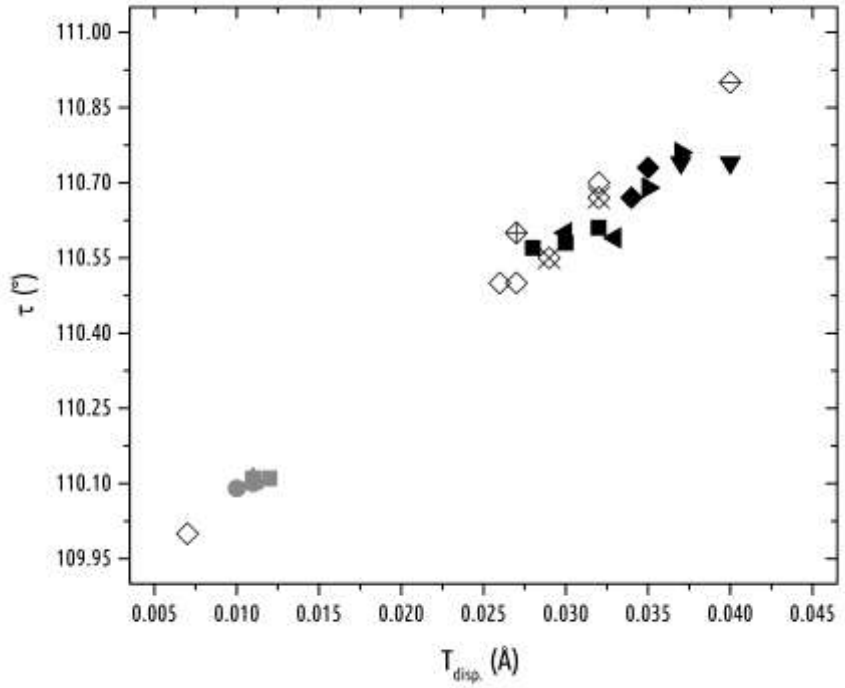

Figure 4.21. Relationship between τ and the displacement of the T cation from the center of the tetrahedron mass, after Brigatti and Guggenheim (2002). Symbols as in Figure 4.3

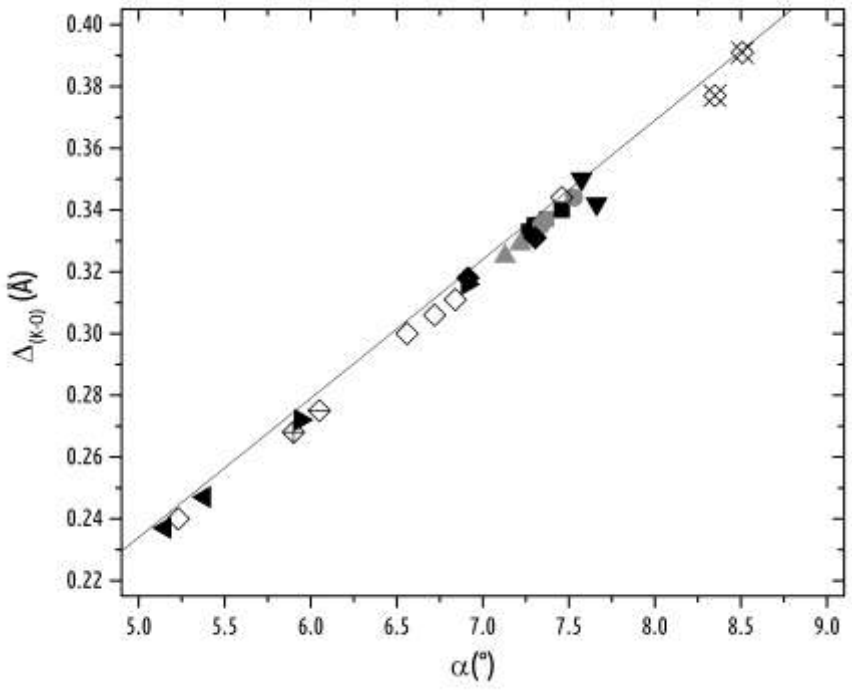

Figure 4.22. Linear relationship between $\Delta_{(K-O)}$ ($\langle K\text{-}O\rangle_{inner}$-$\langle K\text{-}O\rangle_{outer}$) and α. Regression line from Crucianiand Zanazzi (1994): $\Delta_{(K-O)}$= 0.009(3) + α 4.5(5) * 10^{-2}. Symbols as in Figure 4.3

This different behavior is probably due to the higher ^{IV}Al content shown by these crystals, whose enlarging effect is balanced by structural distortion resulting in a decrease of the "lateral" dimension of the tetrahedral sheet. Figure 4.22 shows the relationship between the in-plane rotation α and $\Delta_{(K-O)}$, i.e. the difference between the mean of the six longest K-O distances (K-O_{outer}) and the mean of the six shortest ones (K-O_{outer}); a very good linear relationship exists between these two parameters (McCauley and Newnham, 1971; Cruciani and Zanazzi, 1994).

The most important role of the in-plane rotation is to reduce the mismatch between octahedral and tetrahedral lateral dimensions and it then depends on the composition of the sheets. This is evident by comparing α with the dimensional misfit parameter (Δ_{TM}) (Table 3.3 and 4.4), which is a function of the composition of the tetrahedral and octahedral sheets. The low α, $\Delta_{(K-O)}$ of ORC1_01, ORC1_02 and SIS50_02 is due to the high content of O and F replacing for OH, related to an elevated content of Ti in the octahedral sheet, whose structural effect will be discussed in the next paragraph.

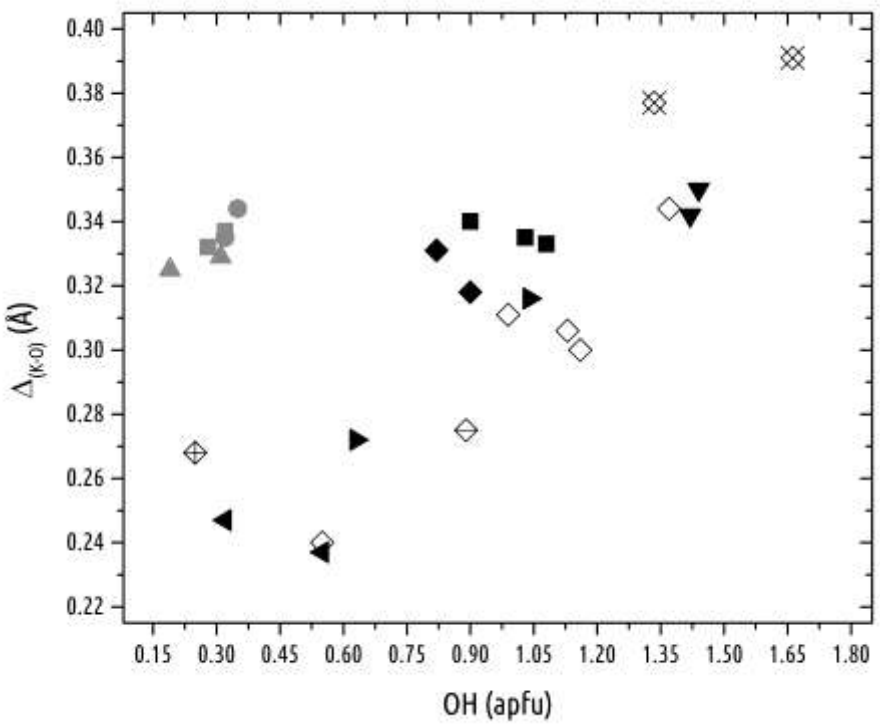

Figure 4.23. Variation of $\Delta_{(K-O)}$ as a function of the OH content . Symbols as in Figure 4.3

In general, a decrease of the OH content, associated with the incorporation of high charge cations in the octahedral sheet, is accompanied by a decrease of $\Delta_{(K-O)}$ (Fig. 4.23), since the loss of the proton is able to strengthen the longer K-O bonds with respect to the others (Table 3.1 and 3.2). The position of 2M_1 samples in Figure 4.23 is to be attributed to the significant amount

of siderophyllitic component. The Al for Si substitution, together with the lower τ value, increases the size of the tetrahedra, thus requiring a higher α value (therefore higher $\Delta_{(K-O)}$) in order to reduce the dimensional misfit. The different way with which the tetrahedral sheet adjusts its dimensions in $2M_1$ samples is also evident if we look at the corrugation of the basal tetrahedral plane, expressed by the parameter (Δz) (Table 3.3 and 3.4). Δz value reflects the out of plane tilting of tetrahedra about the basal bridging oxygen atoms which produces a corrugation of the tetrahedral sheet and a shortening of the distance between apical oxygens along the octahedral edges parallel to (001) (Brigatti and Guggenheim, 2002 and references therein).

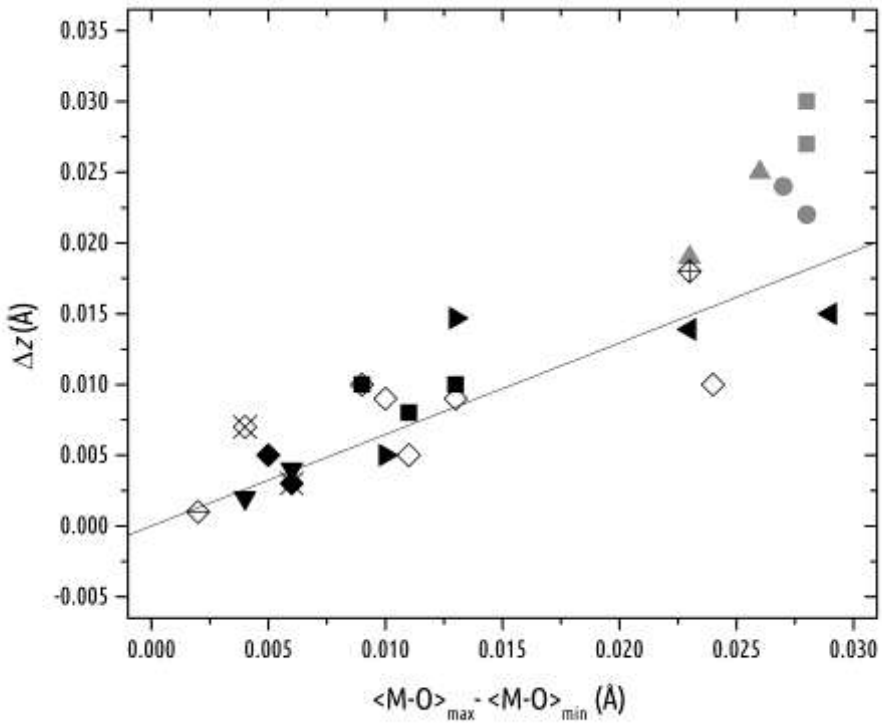

Figure 4.24. Relationship between Δz and the difference in mean bond length between the two octahedral sites $<M\text{-}O>_{max}$ - $<M\text{-}O>_{min}$. Symbols as in Figure 4.3

As expected, Δz values for $2M_1$ samples are the highest observed in this study. Moreover, according to Lee and Guggenheim (1981) and Brigatti and Guggenheim, 2002, Δz reflects the differences in octahedral size; this relationship is evident in Figure 4.24 where Δz is plotted against the difference in mean M-O bond length between the two octahedral sites, in good agreement with the correlation found by Brigatti and Guggenheim (2002). The different crystal chemical behavior of $2M_1$ samples is then to be ascribed not only to the higher Al content of the tetrahedral layer but also to the composition and cation ordering of the octahedral layer that will be discussed in the next paragraph.

4.7 Octahedral sheet geometry

As already mentioned in paragraph 3.1, the analysis of *m.e.n.* points toward a *homooctahedral* nature of the studied samples while geometrical considerations concerning mean M-O distances indicate a *mesooctahedral* character with M1 always larger than M2 (Table 3.1 and 3.2). Difference in size between *cis* and *trans* octahedra is minor for Mg-rich samples and increases with the degree of octahedral substitutions. In all the studied samples, M1 octahedra are more flattened than M2, as testified by the ψ and ELD values (Table 3.3 and 3.4).

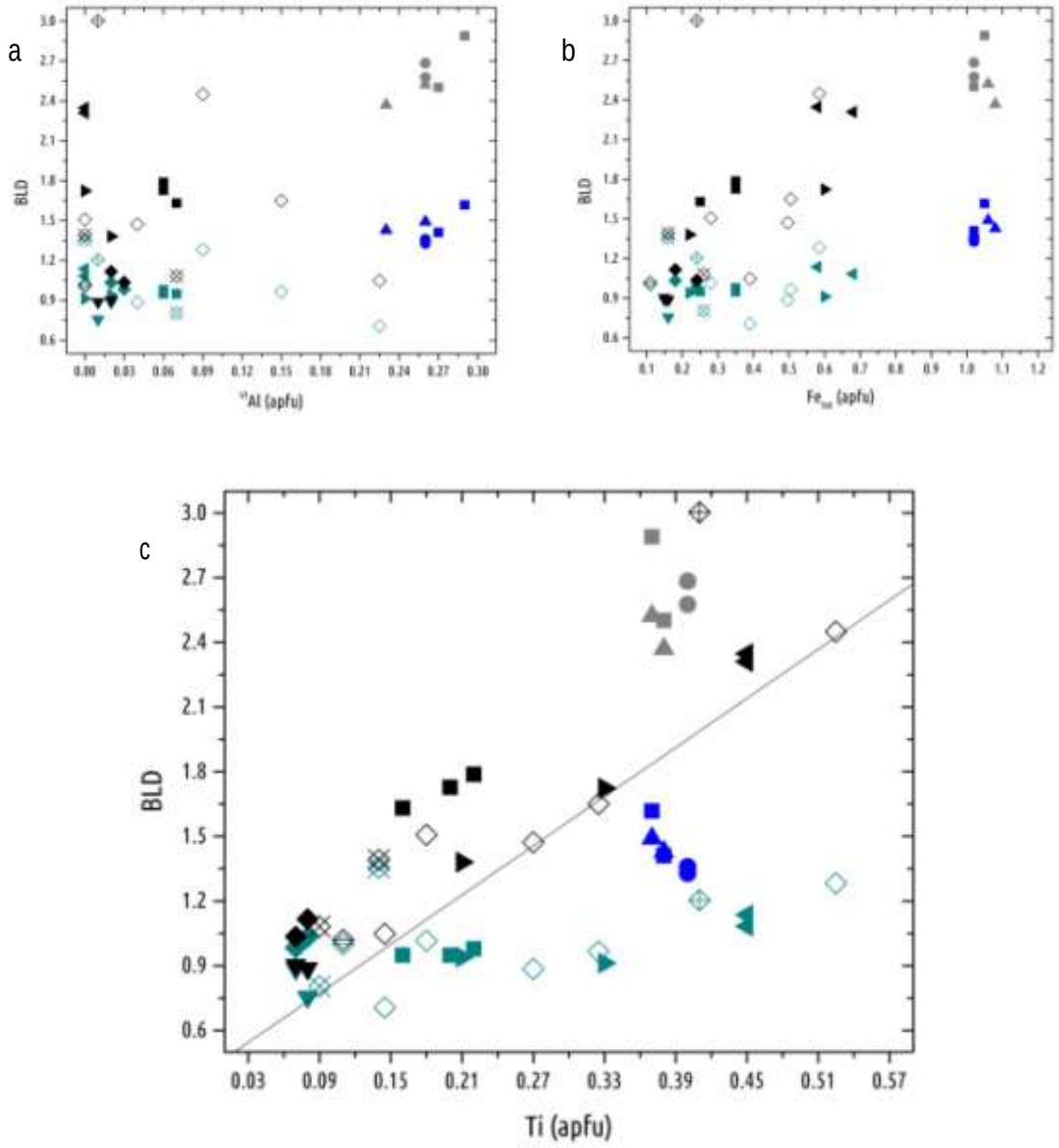

Figure 4.25. Bond length distortion values for M1 and M2 octahedra versus ^{VI}Al content (a), Fe_{tot}content (b) and Ti content (c). Colors: as in Figure 4.3 for M2, green and blue for 1*M* and 2M_1polytypes respectively for M1. Symbols as in Figure 4.3

On the other hand, BLD values for crystals with high contents of cations with charge and size different from Mg, are generally greater in M2 than in M1 (Fig. 4.25 a, b and c). Indeed, given the smaller volumes of M2, the M1 octahedron is forced to flatten in order to reduce its thickness and "adapt" it to the surrounding M2 octahedra. Generally speaking, since M1 is surrounded by six M2 octahedra, with which it shares edges, distortions in M2 have a strong effect on the geometry of M1.

A very interesting aspect is the clear positive correlation occurring between the Ti content and the distortion of bond lengths in M2, already pointed out by many authors (e.g., Cruciani and Zanazzi, 1994; Cesare et al., 2003; Scordari et al., 2006; Schingaro et al., 2011) (Fig. 4.25 c). This is due to the fact that the cation in M2 moves away from the ideal centre of the octahedron by lengthening and shortening specific bonds. In 1*M* crystals the cation is constrained by symmetry to move only on the *y* direction and therefore changes in M2-O bond lengths simply correspond to a negative or positive shift of the cation from the center of the octahedron along *y*, i.e. towards- or away-from the O4-O4 shared edge.

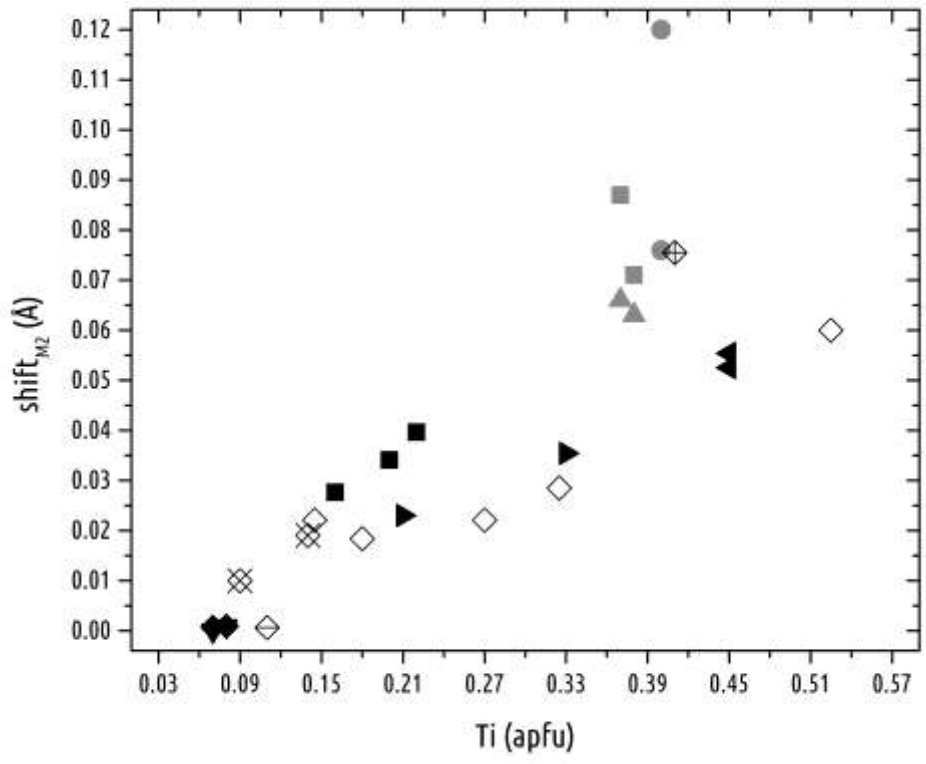

Figure 4.26. Shift$_{M2}$ parameter vs. Ti content. Symbols as in Figure 4.3

The parameter "shift$_{M2}$" (Cruciani and Zanazzi, 1994), which quantifies this displacement, shows values ≥ 0 (i.e. corresponding to a movement towards the O4-O4 shared edge) for all the

studied crystals (Table 3.3 and 3.4); moreover it is well related, as for the BLD parameter, to the Ti content (Fig. 4.26). Concurrently, as Ti increases, a general shortening of the O4-O4 edge can be observed, (Fig. 4.27) (Scordari et al. 2006, 2008; Matarrese et al. 2008; Lacalamita 2009; Schingaro et al. 2011) although samples with low Ti content such as those from Sisco lamproite show as well short O4-O4 edges. These features can be regarded as an indication for the preferential partitioning of Ti in M2; indeed, the phenomenon that would best explain such a structural response is the Ti-*oxy* substitution (Cruciani and Zanazzi, 1994; Cesare et al., 2003; Scordari et al., 2006; Lacalamita et al., 2011). The loss of protons, attached to O4, associated with the displacement of Ti towards the same O4 site, are indeed compatible with the charge-balance requirements in the local M2 environment.

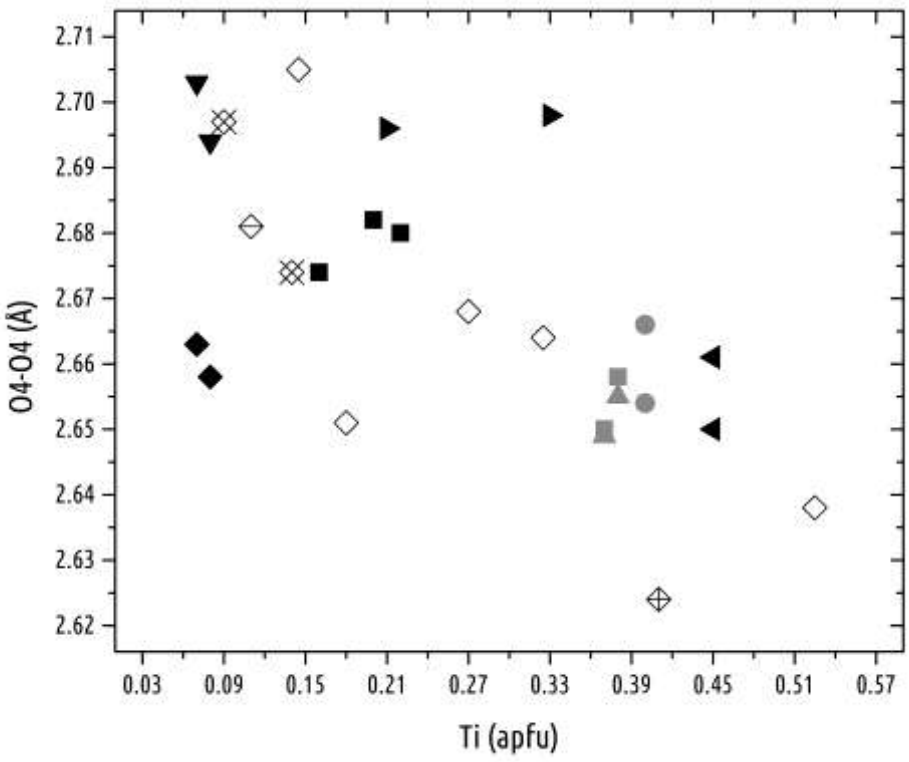

Figure 4.27. O4-O4 edge lenght vs. Ti content. Symbols as in Figure 4.3

Figures 4.28 a, b and c show the relationship between OH content and the most represented highly charged cations, i.e. Al, Fe^{3+} and Ti respectively; it is evident that the presence of Ti is associated with a decrease of the OH content. Since the increase of Ti is directly related to structural distortions in M2, this relationship further support the hypothesis that Ti is preferentially incorporated in M2 through an *oxy*-substitution mechanism. In brief, when Ti enters in M2, it moves toward the O4-O4 edge to balance the loss of the proton by O4; this displacement, however, leads to a decrease of the Ti-Ti distance across the O4-O4 edge, which is

obviously not favored by the increased electrostatic repulsion among cations. The consequence of this mutual repulsion is partially attenuated by a shortening of the O4-O4 shared edge, which intensifies the charge screening effect. According to Cesare et al. (2003), the repulsion would also be avoided assuming short-range ordering of Ti in only one of the two mirror-related M2 sites.

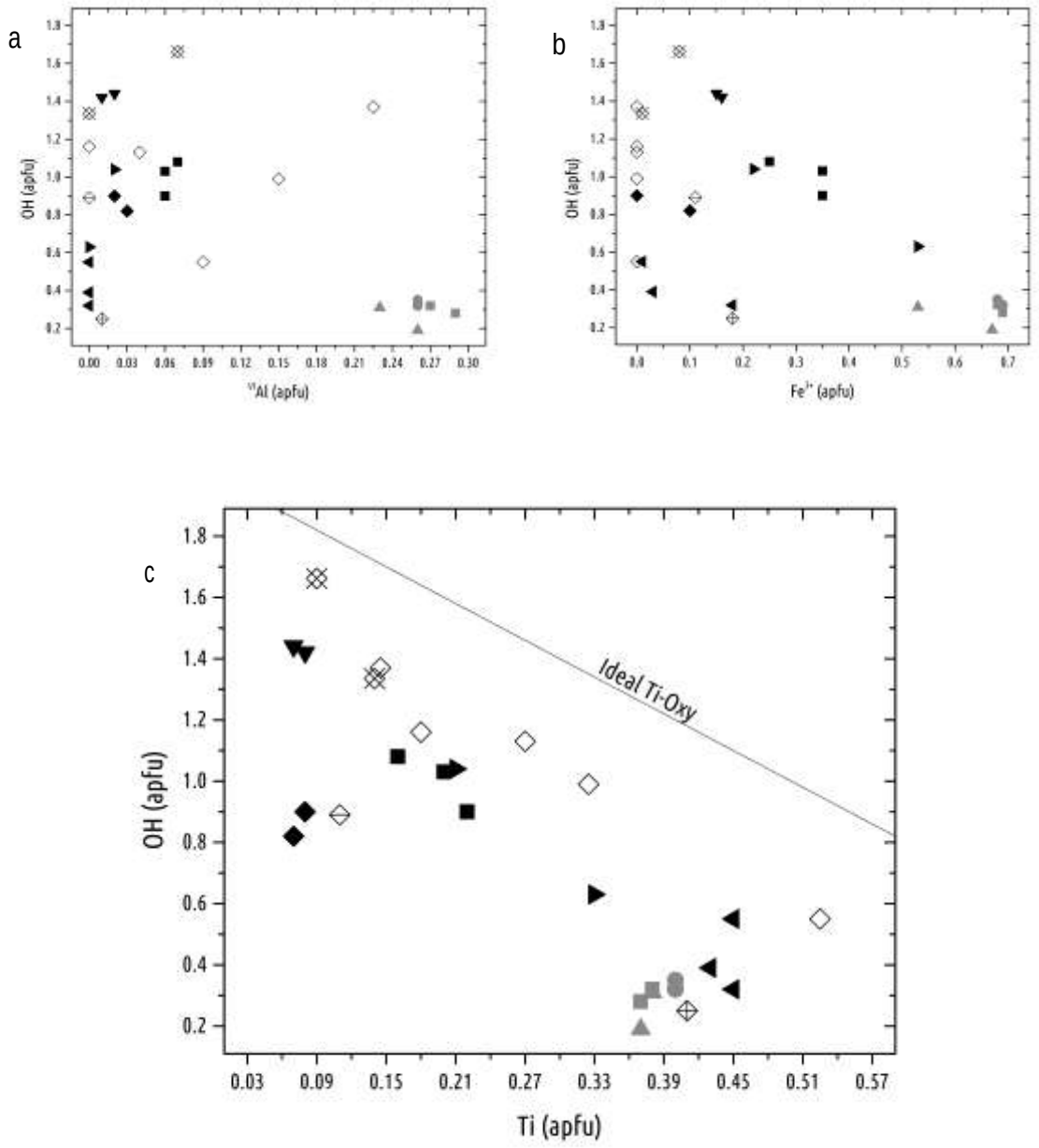

Figure 4.28. OH content plots against: ^{VI}Al content (a), Fe^{3+}content (b), Ti content (c). Symbols as in Figure 4.3

Figure 4.28 c shows that studied crystals describe a linear anticorrelation between OH (apfu) and Ti (apfu), which plot below the correlation line representing the ideal Ti-*oxy*

substitution. The gap might be due to have not taken into account either fluorine content or Fe^{3+} and Al occurrence in the *oxy* substitution. In the former case OH+F would have contributed to satisfy the ideal Ti-*oxy* substitution; furthermore, occurrence of trivalent cations beside Ti, would also contribute to meet the ideal *oxy* substitution relationship. Fe^{3+} is indeed fairly related with the increase of O^{2-} in O4 (Fig. 4.29). The increase of Fe^{3+}, however, does not show direct structural effects on either M1 or M2 sites. With regard to the Al incorporation, it is not observed any relationship with either the content of OH or O^{2-}. It is then likely that the principal mechanism balancing the presence of Al in the octahedral sheet is represented, as already suggested in paragraph 4.3, by Al-Tschermak substitution (Fig. 4.9). According to Brigatti et al. (2000a), a preferential partitioning of Al in M2 is reflected in the shortening of the average M2-O3 distance which decreases with the increase of Al. This feature, however, has neither been observed in the studied crystals nor in phlogopite crystals from lamproite worldwide. In general no relationship was found between the increase of Al and structural modifications, except for a reduction in thickness of the whole octahedral sheet.

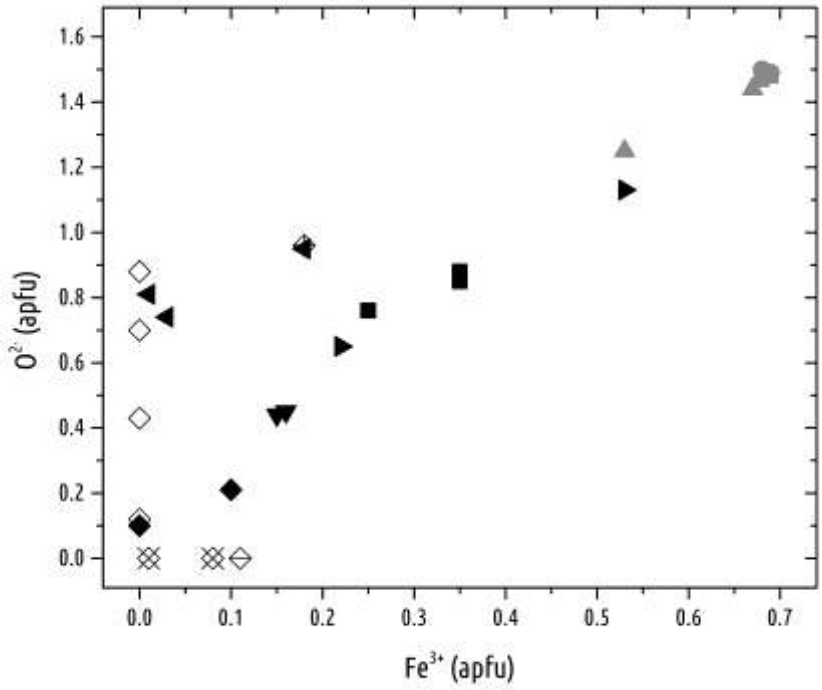

Figure 4.29. Relationship between Fe^{3+} content and O^{2-} content in O4. Symbols as in Figure 4.3

Figure 4.30 shows the representation on (001) of the "octahedral hexagon" formed by the O3 oxygen atoms with O4 placed at its ideal centre introduced by Brigatti et al. (2003a) and Schingaro et al. (2005).

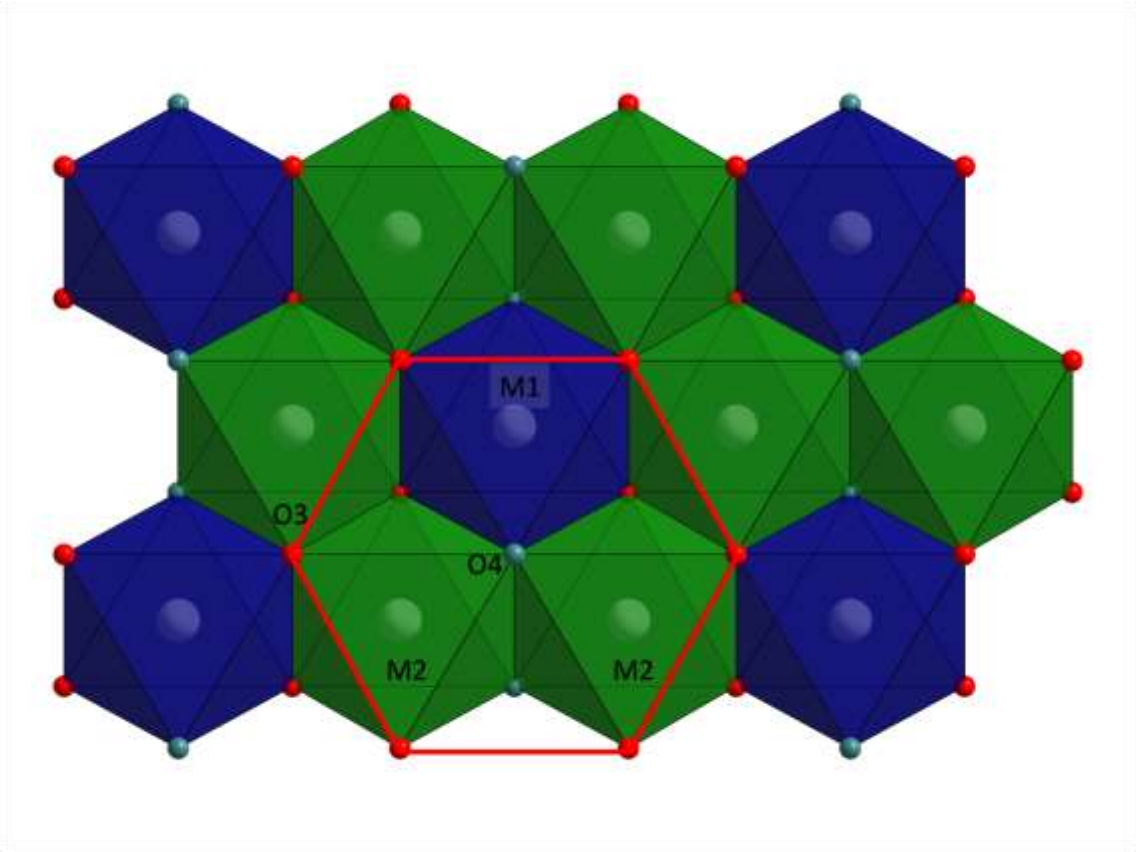

Figure 4.30. Representation of an undistorted octahedral sheet. In red, the hexagon formed by O3 atoms (in red as well); O4 atoms in light-blue; M1 and M2 octahedra in blue and green respectively

This representation is useful to summarize the structural effects of octahedral substitutions in 1*M* micas. The differences in length between the hexagonal edges belonging respectively to M1 and M2 are shown in Figure 4.31, plotted against the displacement of the O4 atom away from the centre of the hexagon. For the studied samples, the displacement of O4 is positively related to the distortion of the hexagon and, consequently, to the increase in size of M1 edges respect to those belonging to the smaller M2; it is not surprising that the samples showing the highest distortion of the hexagon are those from Orciatico, i.e. the richest in Ti. The distortion of the hexagon is indeed, as we note in Figure 4.32, well related to the Ti content. The above mentioned relationships can be seen as the consequences of two main factors: on the one hand, the entrance in M2 of small, highly-charged cations such as Ti decreases the octahedron size; on the other hand, the resulting shortening of the O4-O4 edge, related to the *oxy* substitution mechanism occurring in M2, causes O4 to move towards M2 and away from M1. Not surprisingly, the cation showing the best fit with these distortional parameters is Ti, in good agreement with what observed by Schingaro et al. (2005) and Mesto et al. (2006), who indicated these features as a typical characteristic of *oxy*-substituted micas.

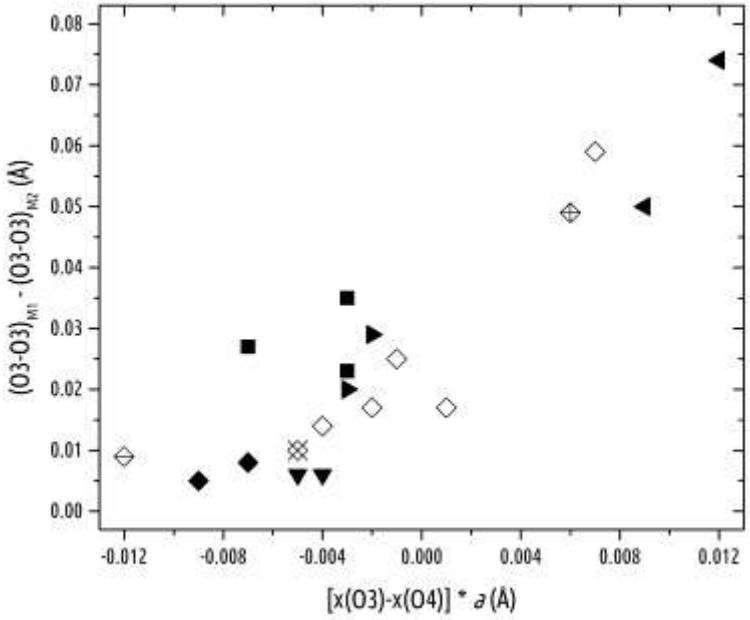

Figure 4.31. Relationship between the O3 hexagon distortion and the O4 atom displacement from the"octahedral hexagon" center. Symbols as in Figure 4.3

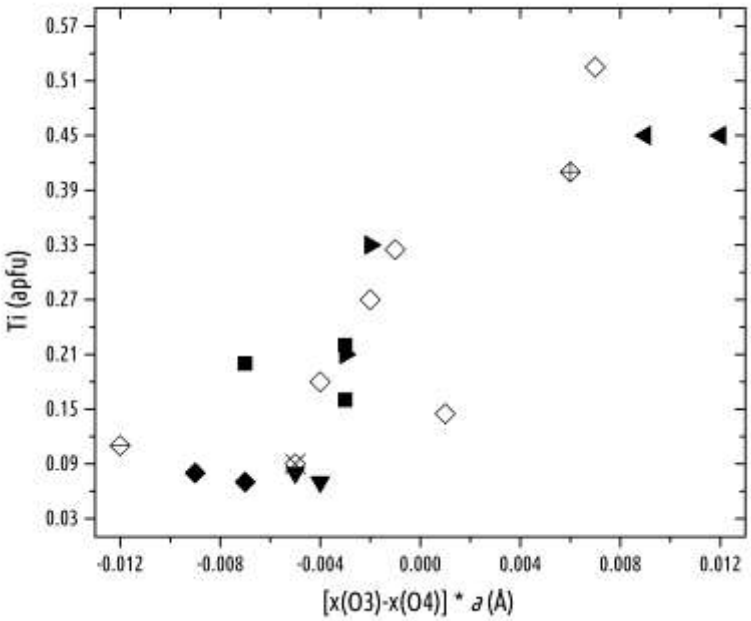

Figure 4.32. Relationship between the displacement of the O4 atom from the "octahedral hexagon center" and the Ti content. Symbols as in Figure 4.3

4.8 Structural role of the O4 site

From all the above considerations we infer the key role of the crystal chemical environment of the O4 site that, thanks to both its adaptability and its interaction with some of the most receptive elements of the mica structure, acts as a mirror of the major modifications occurring in the mineral.

Mercier et al. (2005) defined a parameter useful to better define the role of O4. Similarly to what already done for the Δz parameter (Güven 1971; Toraya 1981), Mercier et al. (2005) defined an expression representing the deviation from planarity of the O3 and O4 sites as $w = (zO3\text{-}zO4) \cdot c\sin\beta$.

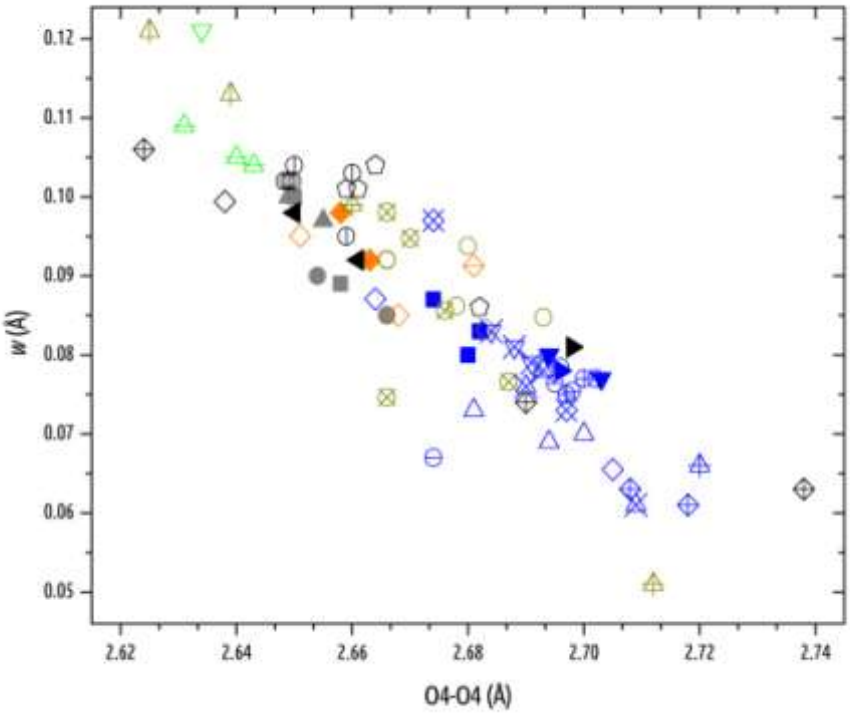

Figure 4.33. *w* vs. O4-O4 edge length for selected micas belonging to the solid solution between annite, phlogopite and tetraferriphlogopite. Symbols: solid symbols, empty diamonds, diamonds with horizontal line, diamonds with plus and diamonds with cross as in Figure 4.3; circles: with horizontal line= Scordari et al. (2006), with vertical line= Schingaro et al. (2011), with cross= Scordari et al. (2008), hollow= Matarrese et al. (2008), with plus= Scordari et al. (2010); upward triangles: with horizontal line= Scordari et al. (2013), with vertical line= Gianfagna et al. (2007), hollow= Cesare et al. (2003), with plus= Mesto et al. (2006), with cross= Zema et al. (2010); downward triangles: hollow= McCauley et al. (1973), with cross= Schingaro et al. (2007); empty pentagons= Lacalamita et al. (2011). Colors: blue = [OH]> 0.9 PFU; black= [OH] < 0.6 apfu; green= [F]>1.0 apfu; orange= intermediate anionic compositions with high OH and F; olive green= [K]<0.85 apfu

The parameter was extensively discussed by Schingaro et al. (2011) who noticed that *w* could have an interesting potential in the discrimination of the anion hosted at the O4 site. In particular, they noted that *w* is anti-correlated with the O4-O4 distance (Fig. 4.33) and seems to have some kind of relationship with the *oxy* component, although fluorophlogopites, independently of the extents of *oxy* substitution, always show the highest *w* values.

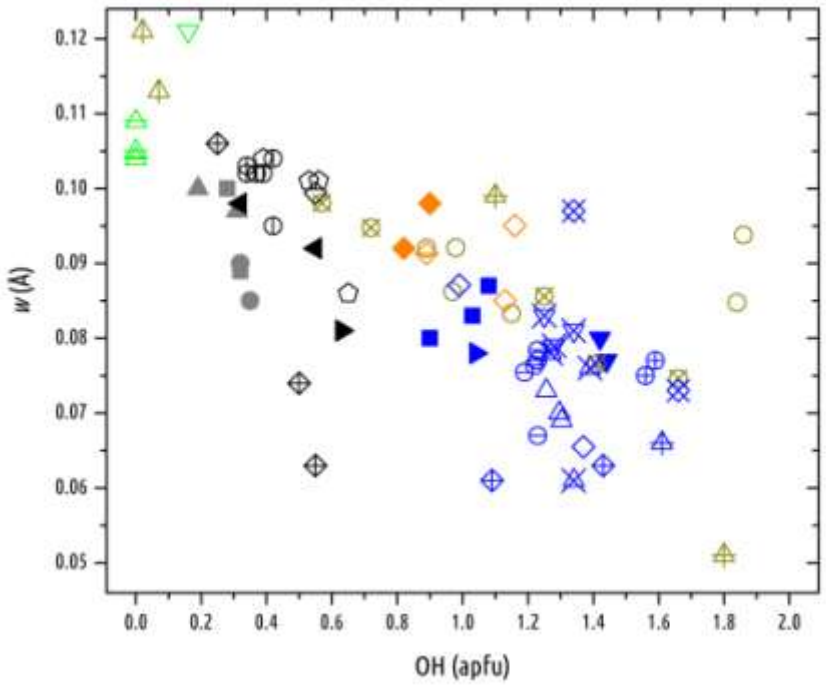

Figure 4.34. *w* vs. OH content. Symbols as in Figure 4.33

Figure 4.34 shows the relationship of *w* with the OH content for samples from this study together with other data from literature having different proportions of OH^-, F^- and O^{2-} at O4 and a wide range of substitutions occurring in the octahedral sheet. The plot confirms that there is a negative correlation between the loss of hydrogen and the magnitude of *w.* Figure 4.35a shows the plot of *w* values against the O^{2-} content in O4 for the same set of samples. Plotted data confirm the observations made by Schingaro et al. (2011) since fluorophlogopites are positioned at the top of the diagram and *w* magnitude still seems to be independent from the amount of $(OH,F)^- \leftrightarrow O^{2-}$ substitution. A possible reason for this behavior could reside in the interaction between O4 and the interlayer cation, that will be different whether O4 is mainly filled by OH, F or O. The substitution of O^{2-} or F^- for OH produces, as previously discussed (paragraph 4.5) a similar effect on the interaction between the interlayer cation and O4.

a

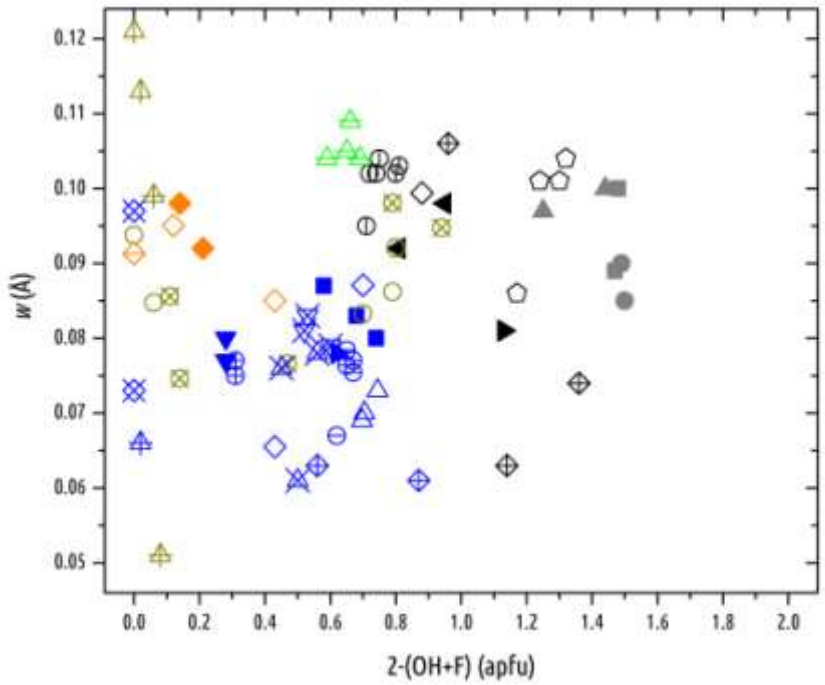

b

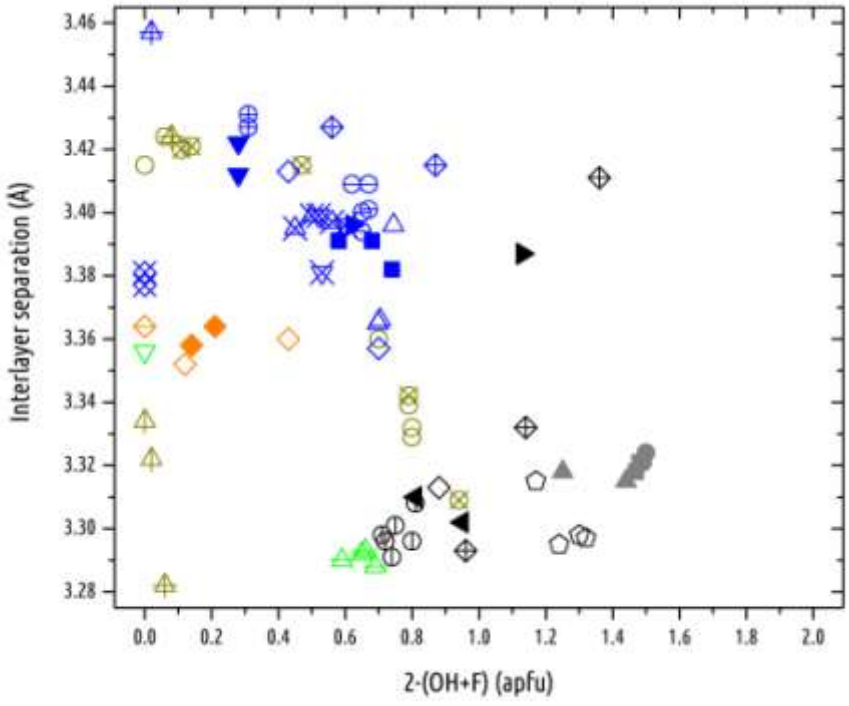

Figure 4.35. The parameter *w* (a) and the interlayer separation (b) plotted vs. the *oxy* component in O4. Symbols as in Figure 4.33

Nonetheless, the different characteristics of oxygen and fluorine, as suggested by Scordari et al., (2013), should be taken into account. In this light it can be interesting to look at the relationship between the O^{2-} content at O4 and the interlayer separation thickness (Fig. 4.35b).

In the diagrams of this paragraph a gross discrimination between OH-rich (>~0.9 apfu; blue symbols), OH-poor (<~0.6 apfu; black and grey symbols) and F-rich (>1.0 apfu; green symbols) samples has been made (see figures caption for details).

As we can see, for OH-rich samples (blue symbols) the increase in the *oxy* component leads to a decrease of the interlayer separation; this behavior is in good agreement with what discussed before, since the loss of hydrogen leads to an increased attraction between O4 and the interlayer cation. However, for OH-poor (black and grey symbols) and F-rich (green symbols) samples, we observe the opposite behavior: the increase of O^{2-} at O4 produces an increase of the interlayer separation. Let us look back at Figure 4.35a: here, the same samples (OH-poor and F-rich), show a behavior opposite to the expected (see previous paragraph). Indeed, a decrease of *w*, and consequently an increase in the O4-O4 distance, is observed with increasing O^{2-}. In Figure 4.36a and b we see that the same trends are confirmed by the relationship of the $shift_{M2}$ parameter, which represents an indirect appraisal of the *oxy* component, with interlayer thickness and *w*, respectively.

In regard to the effect of F, nothing can be said about a dependence of the interlayer separation on the fluorine content for OH-rich, F-poor samples by looking at plotted data (Fig. 4.37a and b). However, with the increase of fluorine content, F-rich (green symbols) or OH-poor (black and grey symbols) samples show a decrease of the interlayer separation and an increase of *w* (Fig. 4.37a and b, respectively). The relationship between the interlayer separation and F content, as well as that with O^{2-}, is obviously biased by the presence of different cations in the interlayer cavity which can lead to apparent discordances with this interpretation (olive green symbols in figures). Moreover, the partitioning into the categories (OH-rich, F-rich, OH-poor) in which data have been subdivided are somewhat arbitrary and cannot account for the many overlaps between them. Furthermore, samples with an intermediate OH composition and elevated F content show an ambiguous behavior between those explained above (orange symbols).

Even so, it is the opinion of the author that analyzed data show that O^{2-} and F^{-} may have a very different behavior. Specifically, the interaction between the interlayer cation and the nature of the atom at O4 causes the interlayer separation to reduce, at increasing O^{2-} contents, only for OH rich samples, while it seems that beyond a certain dehydrogenation extent (roughly 0.6 OH apfu) the effect of O^{2-} reverses, causing the interlayer separation to increase (Fig. 4.35b).

a

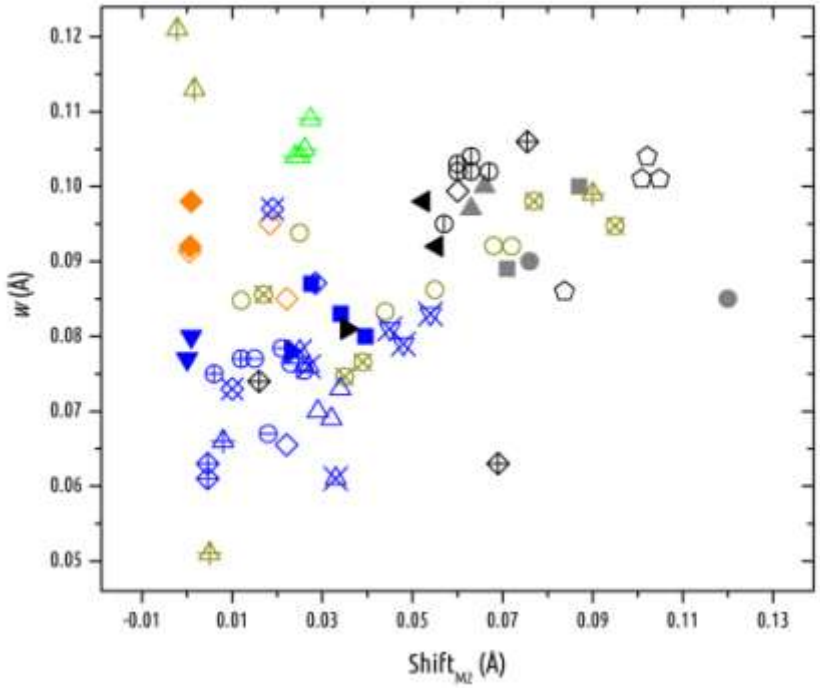

b

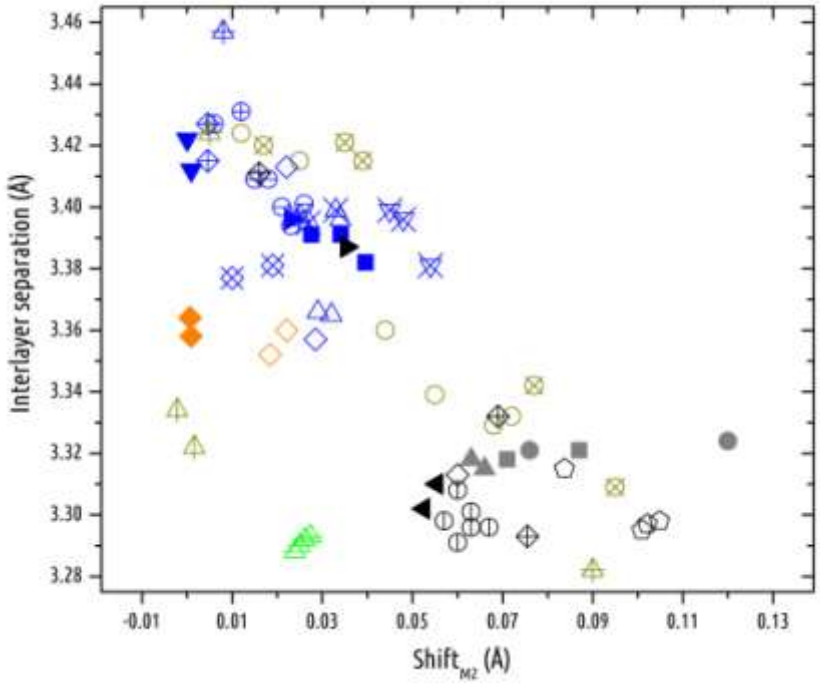

Figure 4.36. Plot. *w*(a) and interlayer separation (b) vs. Shift$_{M2}$. Symbols as in Figure 4.33

a

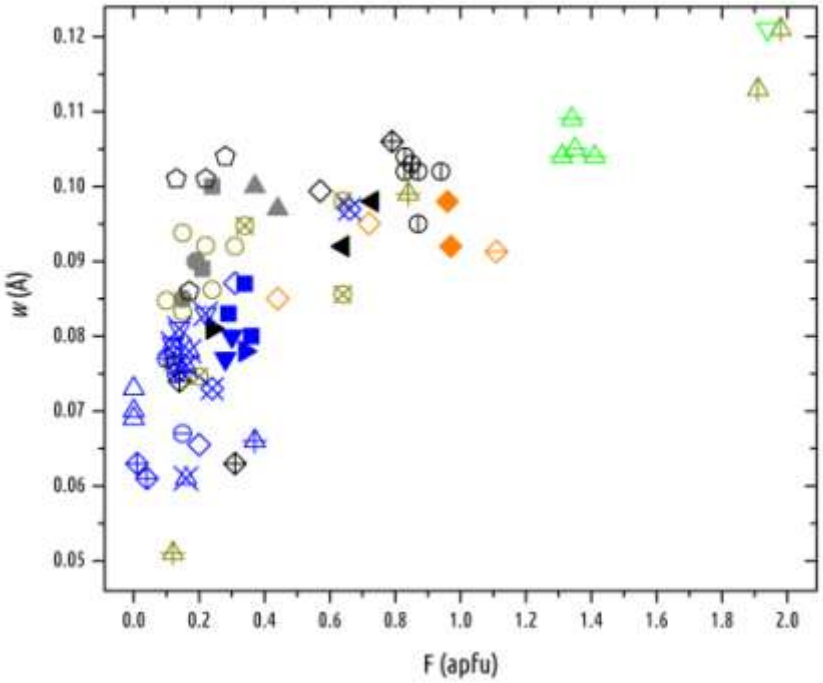

b

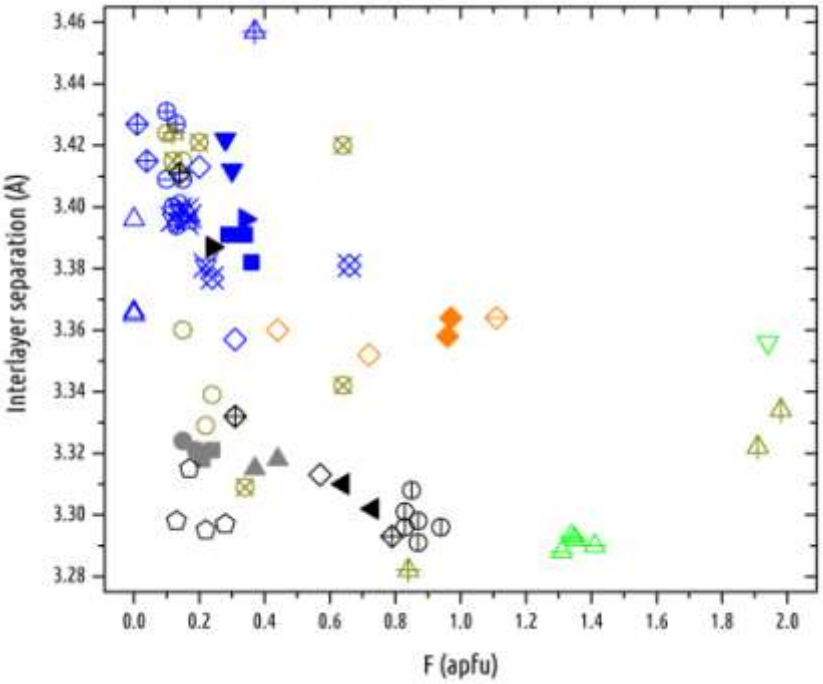

Figure 4.37. Plot of F content vs. a) *w* and b) interlayer separation. Symbols as in Figure 4.33

The most likely explanation for this phenomenon resides in the effect of the *oxy* substitution on the O4-O4 edge. As already pointed out before, as the dehydrogenation proceeds, the O4-O4 edge tends to shorten.

a

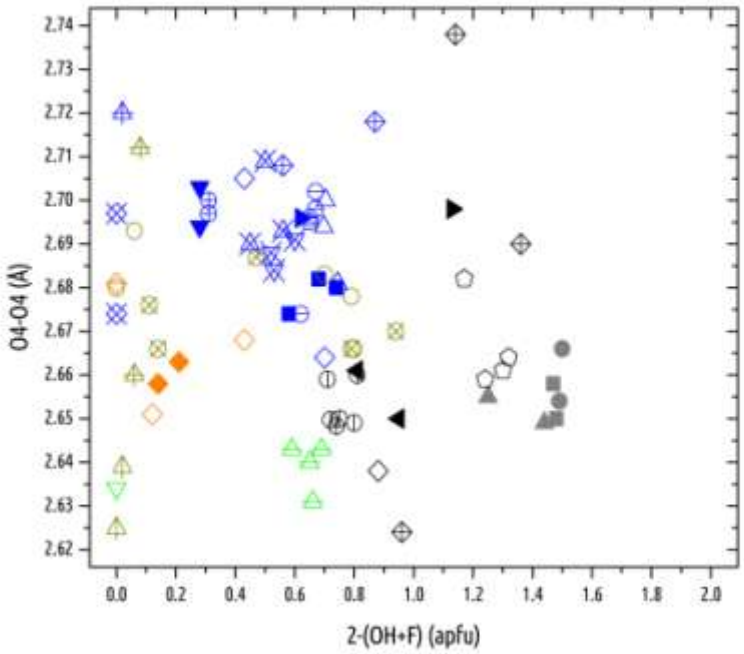

b

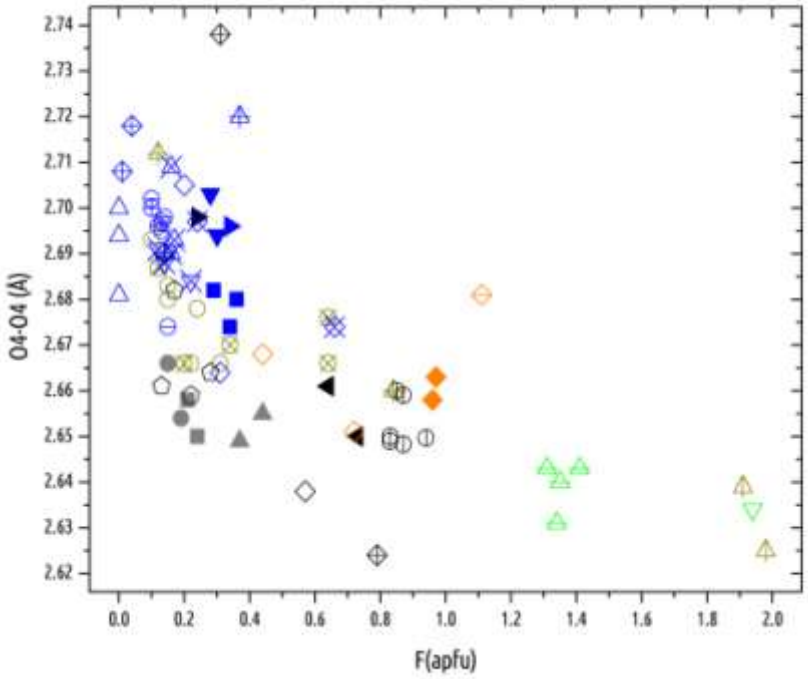

Figure 4.38. Plot of O4-O4 edge lenght vs. a) the *oxy* component in O4 and b) F content in O4. Symbols as in Figure 4.33

The concomitant increase in the electrostatic repulsion between two oxygen atoms probably has a limit beyond which the atoms cannot move any closer. The stronger interaction

between O^{2-} and the interlayer cation with respect to F^- should also be taken into account since it can partly prevent O4 from moving away from the interlayer cation.

For the same reason we do not observe this change of response when considering F, which does not seem to have a strong structural effect when present at low quantities but, at increasing contents, produces a monotone structural reaction, decreasing the interlayer separation and increasing the *w* value. This mechanism is probably due to the lower charge and size of F^- with respect to O^{2-} that makes it possible to reduce the O4-O4 edge to a higher extent and, at the same time, attenuates the interaction with the interlayer cation.

The above considerations are also evident observing the plot of the O4-O4 edge vs. F^- and O^{2-} shown in Figures 4.38a and b, respectively: while the O4-O4 edge does not show any correlation with the O^{2-} content (Fig. 4.38a), it is possible to observe a dependence in Figure 4.38b: samples show a non-linear decrease of the O4-O4 edge-length at increasing F down to a minimum value (~ 2.62 Å). Note however that analogous or even shorter O4-O4 distances have been found for completely OH-, F-free trioctahedral micas such as balestraite (~ 2.63 Å) (see paragraph 5.2) and, even more markedly, norrishite (~ 2.53 Å) (Tyrna and Guggenheim, 1991). Balestraite and norrishite are two examples of completely dehydrogenated Li-micas with Li completely filling the M1 site and, in the case of balestraite, M3 site too. The extremely low O4-O4 distance shown by these minerals suggests that the nature of the atom occupying M1 could also have an important influence on the O4 site. In this light, the characterization of phases originated in strongly oxidizing conditions with high contents of Li, can be very interesting. Chapter 7 illustrates the case of two minerals, balestraite and a new Mn rich phase, found in Cerchiara mine, an ore which shows these peculiar geochemical characteristics.

4.9 Final crystal-chemical formulae

As already mentioned in paragraph 3.2, formula recalculation of micas is indeed a tricky task. Observing the formulae normalized on the basis of 12 (O, OH, F, Cl) anions shown in Table 3.6, it is evident, by observing octahedral cations sums, that this recalculation method cannot be considered satisfactory since for almost all the studied samples these sums exceed by far the limit of 3 apfu. Nonetheless, this normalization scheme is able to highlight an important fact. Given the high sums for octahedral cations, we can assume the studied samples to be not affected by octahedral vacancies.

Table 3.7 shows formulae then calculated on the basis of the "7 cations method" assuming all Fe as Fe^{2+} and all Ti as Ti^{4+}. Given the peculiarities shown by every sample, the process leading to the final crystal-chemical formula will be here reported on a case-by-case basis. Final crystal-chemical formulae for all the studied samples are reported in Table 4.1. Table 4.2, lists *m.e.n.* obtained from final crystal chemical formulae and from structure refinements.

4.9.1 Western Alps

It is evident, from Table 3.7, that for VDA3_X and VDA3_XI crystals, the assumption of all Fe as Fe^{2+} is not in agreement with the measured anionic population. Even assuming all Fe as Fe^{3+}, the discrepancy between positive and negative charge is about 0.17 and 0.16e^- respectively in favor of negative charges. Mössbauer results (Table 3.8) suggest a Fe^{2+}/Fe_{tot} ratio of 76.5%, which is definitely not in agreement with chemical analyses. An explanation for these discrepancies probably resides in the H_2 content by SIMS. If we have a look back at Figure 4.18 we can see that, although Alpine samples composition is very close to the phlogopitic end-member, they still lie below the line relating $c\sin\beta$ to H_2O content. The final OH content was then let vary until achievement of the charge balance. It was not possible to find an agreement with Mössbauer results, likely because of both the limited amount of Fe in the samples and the fact that the information from this technique is averaged through a much bigger quantity of material. Finally, mean electron number derived from EMPA data and structure refinements are in fair agreement (Table 4.2).

4.9.2 Southern Tuscany

Samples from Montecatini Val di Cecina show a better balance between positive and negative charges (Table 3.7). The Fe^{2+}/Fe_{tot} ratio was let vary until achievement of electrostatic balance for MVC100_02, reaching a final value of 58%. Although this ratio is rather distant from the one suggested by Mössbauer results (75%, see Table 3.8), the divergence can be considered acceptable given the large difference in the amount of material analyzed with SIMS and MS techniques. Sample MVC100_04 shows instead a slight over-estimation of the H_2O content (Fig. 4.18, Table 3.7); OH content was therefore lowered in order to reach electrostatic balance. In this case, final data from EMPA and SIMS are not in agreement with Mössbauer data while they show a good accord with *m.e.n* derived from structure refinements (Table 4.2).

Samples from Orciatico show a sum of Si+Al slightly lower than 4 and tetrahedral sites were then considered filled with the addition of the necessary amount of Ti^{4+}. The Fe^{2+}/Fe_{tot} ratio was

let vary until achievement of charge-balance; *m.e.n.* from crystal chemical formulae systematically have higher values compared to those obtained from structure refinement.

4.9.3 Corsica

After adjusting the Fe^{2+}/Fe_{tot} ratio, calculated formulae, as far as it concerns electrostatic balance, lead to a satisfying result for SIS50_02 while for SIS50_07 the formula resulted slightly unbalanced (22.59 positive charges vs. 22.67 negative charges assuming all Fe as Fe^{3+}). The indirect appraisal of H_2O content for both the samples suggests an higher hydrogen content; the imbalance was then attributed to an underestimation of H via SIMS analysis. The OH value was increased by 0.08 a.p.f.u. to achieve electrostatic balance for SIS50_07 while it was left unvaried for SIS50_02 since charge balance was already achieved. Analogously to the Orciatico crystals, SIS50_02 shows an unsatisfactory difference between *m.e.n.* from chemistry and structure refinement.

4.9.4 Torre Alfina

All the crystals belonging to the $2M_1$ polytype, show a satisfactory estimate of H_2O content and charge balance is easily achieved varying the Fe^{2+}/Fe_{tot} ratio. Those belonging to the $1M$ polytype, besides having quite a different chemical composition, show a marked underestimation of the H_2O content (Figure 4.18). OH content for these samples was then increased until charge balance was finally achieved. Also sample VS90_01 exhibits a high discrepancy between calculated and observed *m.e.n.*.

Table 4.1. Final crystal-chemical formulae on the basis of of Σ (octahedral+tetrahedral cations)=7

	VDA3_X	VDA3_XI	MVC100_02	MVC100_04	ORC1_01	ORC1_02	ORC1_03	SIS50_02	SIS50_07
Si	2.96	2.99	2.93	2.99	2.88	2.92	2.89	2.97	2.97
^{IV}Al	1.05	1.02	1.07	1.01	1.11	1.07	1.08	1.03	1.03
^{IV}Ti^{4+}	-	-	-	-	0.01	0.01	0.03	-	-
^{IV}Sum	4.00	4.00	4.00	4.00	4.00	4.00	4.00	4.00	4.00
^{VI}Ti^{4+}	0.08	0.07	0.07	0.08	0.44	0.44	0.40	0.33	0.21
^{VI}Al	-	0.01	0.03	0.02	-	-	-	-	0.02
Fe^{2+}	-	-	0.14	0.18	0.40	0.67	0.47	0.07	-
Fe^{3+}	0.16	0.15	0.10	-	0.18	0.01	0.03	0.53	0.22
Mg	2.69	2.71	2.58	2.68	1.93	1.84	2.05	2.05	2.51
Cr	0.05	0.04	0.07	0.03	-	-	-	-	0.03
V^{3+}	-	-	-	-	0.01	0.01	0.01	-	0.01
Mn^{2+}	-	-	-	-	-	-	-	0.01	-
Li	0.01	0.01	0.01	0.01	0.04	0.03	0.04	0.01	-
^{VI}Sum	3.00	3.00	3.00	3.00	3.00	3.00	3.00	3.00	3.00
K	0.94	0.94	0.91	0.90	0.86	0.85	0.87	0.95	0.94
Na	0.01	0.01	0.04	0.05	0.07	0.06	0.05	0.01	0.01
Ba	-	-	-	-	0.05	0.05	0.05	0.01	-
^{XII}Sum	0.95	0.95	0.95	0.95	0.98	0.96	0.97	0.97	0.95
OH	1.42	1.44	0.82	0.90	0.32	0.55	0.39	0.63	1.04
F	0.30	0.28	0.97	0.96	0.73	0.64	0.87	0.24	0.34
O	10.28	10.28	10.21	10.14	10.95	10.81	10.74	11.13	10.62

Table 4.1. (continued)

	VS29_01	VS29_08	VS29_10	VS29_11	VS29_12	VS70_15	VS70_16	VS90_01	VS90_04
Si	2.75	2.75	2.87	2.90	2.85	2.75	2.74	2.72	2.77
^{IV}Al	1.25	1.25	1.13	1.10	1.15	1.25	1.26	1.28	1.23
^{IV}Sum	4.00	4.00	4.00	4.00	4.00	4.00	4.00	4.00	4.00
Ti^{4+}	0.38	0.37	0.20	0.16	0.22	0.40	0.40	0.38	0.37
^{VI}Al	0.27	0.29	0.06	0.07	0.06	0.26	0.26	0.23	0.26
Fe^{2+}	0.34	0.36	-	-	-	0.34	0.33	0.39	0.07
Fe^{3+}	0.68	0.69	0.35	0.25	0.35	0.68	0.69	0.67	0.53
Mg	1.26	1.25	2.37	2.43	2.31	1.28	1.28	1.26	1.26
Cr	0.02	0.01	0.01	0.08	0.05	0.01	0.01	0.01	0.01
V^{3+}	0.03	0.02	0.01	0.01	0.01	0.02	0.02	0.02	0.02
Mn^{2+}	-	-	-	-	-	-	-	-	-
Li	0.02	0.01	-	-	-	0.01	0.01	0.02	0.02
^{VI}Sum	3.00	3.00	3.00	3.00	3.00	3.00	3.00	3.00	3.00
K	0.90	0.90	0.94	0.92	0.94	0.91	0.92	0.92	0.92
Na	0.06	0.07	0.02	0.01	0.02	0.06	0.06	0.06	0.05
Ba	0.01	0.01	0.01	0.01	0.01	0.01	-	0.01	0.01
^{XII}Sum	0.97	0.98	0.97	0.94	0.97	0.98	0.98	0.99	0.98
OH	0.32	0.28	1.03	1.08	0.90	0.35	0.32	0.31	0.19
F	0.21	0.24	0.29	0.34	0.36	0.15	0.19	0.44	0.37
O	11.47	11.48	10.68	10.58	10.74	11.50	11.49	11.25	11.44

Table 4.2 Mean electron numbers of cation sites (e^-) as determined by structure refinements (X-ref) and chemical analyses (EMPA).

	VDA3_X	VDA3_XI	MVC100_02	MVC100_04	ORC1_01	ORC1_02	ORC1_03	SIS50_02	SIS50_07
$e^-_{(M1)\ X\text{-}ref}$	12.84	12.56	13.68	12.56	14.80	15.92		14.24	13.12
$e^-_{(M2)\ X\text{-}ref}$	12.84	12.56	13.68	13.12	15.08	15.92		14.24	13.68
$e^-_{(M1+M2)\ X\text{-}ref}$	38.52	37.68	41.04	38.80	45.10	47.76		42.72	40.48
$e^-_{(M1+M2)\ EMPA}$	39.56	39.21	40.84	39.61	48.27	49.76	47.41	47.74	41.67
$e^-_{(K)\ X\text{-}ref}$	18.68	18.68	18.36	18.04	19.00	19.00		18.36	18.68
$e^-_{(K)\ EMPA}$	17.97	17.97	17.73	17.65	19.91	19.61	19.88	18.72	17.97
	VS29_01	VS29_08	VS29_10	VS29_11	VS29_12	VS70_15	VS70_16	VS90_01	VS90_04
$e^-_{(M1)\ X\text{-}ref}$	18.44	18.16	13.68	13.68	14.24	18.16	18.16	17.88	18.16
$e^-_{(M2)\ X\text{-}ref}$	18.16	18.30	14.24	14.24	14.80	18.02	18.02	17.46	17.74
$e^-_{(M1+M2)\ X\text{-}ref}$	54.76	54.76	42.16	42.16	43.84	54.20	54.20	52.80	53.64
$e^-_{(M1+M2)\ EMPA}$	54.74	54.94	43.19	42.24	43.87	54.79	54.79	55.31	54.96
$e^-_{(K)\ X\text{-}ref}$	18.20	18.20	18.68	18.68	18.36	18.04	18.20	18.04	18.52
$e^-_{(K)\ EMPA}$	18.32	18.43	18.64	18.15	18.64	18.51	18.14	18.70	18.59

5 Peculiar substitutions in micas: two new minerals from Cerchiara mine

As anticipated, this chapter deals with the description of two peculiar phases found in the unique environment of Cerchiara mine. Paragraph 5.2 reports the results of chemical, structural and spectroscopic studies to define and describe balestraite, named after Corrado Balestra (b. 1962), a prominent Italian amateur mineralogist and an expert of Ligurian minerals. The mineral and its name have been approved by the Commission on New Minerals, Nomenclature and Classification, IMA (2013-080). The holotype material is deposited in the mineralogical collections of the Museo di Storia Naturale, Università di Firenze (Italy), under catalogue number 3133/I. The results of this study are reported in an article on the *American Mineralogist* (Lepore et al., 2015). Paragraph 5.3 describes some preliminary results concerning a new Mn-, Mg-rich dioctahedral mica characterized by a tetrasilicic tetrahedral sheet.

5.1 Cerchiara mine

Balestraite and the new dioctahedral Mn-rich, tetrasilicic mica were found in the ore body of the Cerchiara mine (~44°11'58''N, 9°42'1''E), which belongs to the well-known Mn district of Eastern Liguria named "Gambatesa district". The ore body is located near the base of chert sequences ("Diaspri di Monte Alpe" Formation) overlaying Jurassic ophiolites (Cortesogno et al. 1979; Lucchetti et al. 1988). The ore consists of rhythmic interlaying of braunite-bearing metasediments (5-15 cm thick) and hematite-rich cherts. According to Cabella et al. (1998), the primary Mn-oxide and hematite-rich cherts formed by fractionation from hydrothermally derived metalliferous siliceous muds during turbiditic re-sedimentation; subsequently, the sedimentary-diagenetic deposits were re-equilibrated under prehnite-pumpellyite facies conditions leading to a braunite + quartz stable assemblage. During this stage, reactions triggered by mobilized fluids along fractures produced Mn-silicate and Mn-carbonate assemblages at the expense of braunite + quartz. Successive decompressional tectonic evolution under decreasing *P-T* metamorphic conditions induced further concentration of dispersed elements, such as Ba, Sr, As, and V, to allow the genesis of a great variety of new and rare minerals in later extensional fractures. The carbonate veins exhibit boundaries which are locally enriched in alkaline and alkaline-earth elements, such as Li, Na and Ba (Cabella et al. 1990). Sugilite (Cabella et al. 1990), together with other unusual Li-rich phases such as norrishite and nambulite and small amounts of vanadiferous species like

gamagarite, tokyoite and pyrobelonite, have been found (unpublished data). Balestraite was found at the boundary between carbonate-bearing veins and hematite bands.

5.2 Balestraite

5.2.1 Introduction

Balestraite was found in the manganesiferous beds within the metacherts of the ophiolitic sequences at the Cerchiara mine, Eastern Liguria (Italy) at the boundary between carbonate-bearing veins and hematite bands. The mineral forms a layered cluster, about 2 × 1 cm in size, of randomly packed crystals in contact with quartz and calcite (Fig. 5.1).

Figure 5.1. Balestraite from Cerchiara mine associated with quartz and calcite (R. Bracco photo); field of view is 2 mm.

Preliminary chemical analyses showed a composition suggesting a new member of the mica group. In particular, data obtained via energy dispersive spectrometry (EDS) analyses on a polished section indicated an unusually high V content, and no other transition metals or Al. Muscovite and phlogopite with high V contents have been occasionally reported [e.g. Pan and Fleet (1992), Ankinovich et al. (2001) and Giuliani et al. (2008)]. Until now, however, the only known V-members of the mica group were roscoelite, ideally $KV_2[AlSi_3O_{10}(OH)_2]$ (Brigatti et al. 2003b) and chernykhite, ideally $BaV_2[Al_2Si_2O_{10}(OH)_2]$ (Ankinovich et al. 1973). Thus, owing to the absence of Al, this mineral was worthy of further investigations.

5.2.2 Physical and optical properties

Balestraite exhibits a tabular morphology, and does not show any inclusions of, or intergrowths with, other minerals. The maximum grain size of balestraite is about 400 μm. The mineral is pale yellow in color, transparent with silky lustre and does not fluoresce under short- and long-wave ultraviolet light. It is brittle (Mohs hardness between 2½ and 3) with uneven fracture and shows a perfect {001} cleavage. The calculated density is 2.946 g cm^{-3}, based on the empirical formula and the unit-cell dimensions determined by single-crystal X-ray diffraction (see below).

Balestraite is biaxial, optically negative with α = 1.642(2), β = 1.664(2) and γ = 1.676(2); the measured $2V$ is 84.4(2)° ($2V_{calc}$ = 72°), and it has a distinct dispersion ($r < v$). The mineral does not show pleochroism and its color is pale grey in thin section. Optical properties were measured using monochromatic Na light (λ = 589 nm) at room temperature.

5.2.3 Experimental methods

5.2.3.1 X-ray diffraction and structure refinement

Several platy crystals with variable lateral dimensions and thickness (volumes ranging from 1 to 400 $\cdot 10^4$ μm^3, approximately) were mounted on a 8 μm-diameter carbon fiber and examined on a CCD-equipped Oxford Diffraction Xcalibur 3 diffractometer to avoid twinned and/or deformed crystals. In general, crystal quality was poor, with weak and very broad reflections, usually not sufficient even for unit-cell determination. After dozens of trials, a crystal (30 × 220 × 250 μm) suitable for full data collection, although far from optimal, was found. The refined unit-cell dimensions are: a = 5.2024(5), b = 8.9782(7), c = 9.997(2) Å, β = 100.40(2)° and V = 459.3(1) $Å^3$, suggesting that the mineral is a 1*M* polytype. Intensity integration and standard Lorentz-

polarization corrections were performed with the *CrysAlis* RED software package (Oxford Diffraction 2006). The program ABSPACK in *CrysAlis* RED (Oxford Diffraction 2006) was used for the absorption correction, and the structure refinement was performed using the full matrix least-squares program SHELXL-97 (Sheldrick 2008). Initial attempts to refine the structure in the ideal space group $C2/m$ did not produce convergence. Ordering of the octahedral cations was considered with a decrease of symmetry to the $C2$ space group, starting from atomic coordinates given by Brigatti et al. (2000) for polylithionite. The refinement in this subgroup led to an improvement of the R factor (with R_1 decreasing from 0.261 to 0.223 for the isotropic model), without significant correlation between parameters of the pseudo-mirror related atoms. Attempts to refine a Cm model, which produces disorder of the octahedral cations, led to higher R factor (R_1 = 0.240 for the isotropic model) with an unreliable isotropic thermal parameter for O4.

Scattering curves for ionized Li, O, Si, and V as well as $\Delta f'$, $\Delta f''$ coefficients were taken from Wilson and Prince (1999). The site occupancy factors were initially allowed to vary (Li^+ vs. V^{5+}) for the three independent M sites; M1 was found to be fully occupied by Li and fixed accordingly. Refinement of the anisotropic atomic displacement parameters was possible only for T1, T2 and M2 (nearly totally occupied by V), whereas for M1 and M3 (nearly totally occupied by Li) and the oxygen atoms an isotropic model was maintained. The final R_1 indices of 0.127 [for 1302 reflections with $F_o > 4\sigma(F_o)$] and 0.138 (for all 1587 independent reflections) were considered acceptable given the quality of the crystal. The refined Flack parameter (Parsons and Flack 2004) of 0.08(2) is consistent with a highly asymmetrical distribution of the enantiomorphic components and indicates that the acentric model is correct. Details of the data collection and refinement are given in Table 5.1, final atomic coordinates and isotropic displacement parameters are listed in Table 5.2. The diffraction rings from few grains of balestraite were collected with a CCD-equipped diffractometer Xcalibur PX Ultra using Cu$K\alpha$ radiation (50 kV and 40 mA) and then converted into a conventional XRD pattern. The crystal-to-detector distance was 7 cm. Data were processed using the *CrysAlis* software package version 1.171.31.2 (Oxford diffraction 2006) running on the Xcalibur PX control PC. Observed and calculated X-ray powder diffraction data are listed in Table 5.3. The unit-cell parameters from powder data are: a = 5.2087(2), b = 8.9991(3), c = 10.0304(4) Å, β = 100.354(3)° and V = 462.51(2) Å^3, in fair agreement with the values obtained from single-crystal data (Table 5.1).

5.2.3.2 Chemical analyses

A crystal of about 450 × 180 × 50 μm was embedded in epoxy and polished for electron microprobe analysis, which was obtained with a JEOL 8200 electron microprobe at the Dipartimento di Scienze della Terra of the University of Milan (Italy) in wavelength dispersion mode at 15 kV, 5 nA beam current, and 10 μm as the beam size. The following standards were used: wollastonite (Si$K\alpha$), K-feldspar (K$K\alpha$), pure vanadium (V$K\alpha$), and rhodonite (MnKα). Five point analyses on different spots were performed. Na, Mg, Ca, Ba, Al, Ti, F, and Cl were below 0.01 wt%. The crystal fragment was found to be homogeneous within analytical uncertainty.

In situ analysis of the content of Li was performed using laser-ablation inductively-coupled-plasma mass-spectrometry (LA-ICP-MS). The laser probe consists of a Q-switched Nd:YAG laser, model Quantel (Brilliant), whose fundamental emission in the near-IR region (1064 nm) was converted into 266 nm wavelength using two harmonic generators. Spot diameter was near 40-50 μm. The ablated material was analyzed by using an Elan DRC-e quadrupole mass spectrometer. Helium was used as the carrier gas and mixed with Ar downstream of the ablation cell. Data reduction was performed using the Glitter Software. NIST SRM 610 was analyzed as an external standard, whereas the SiO_2 was used as an internal standard. Precision and accuracy were assessed from repeated analyses of the BCR-2g, NIST SRM 612 and 610 standards and resulted in better than ± 3%. Full analytical details are reported in Tiepolo et al. (2005) and Miller et al. (2007).

Table 5.4 reports the chemical analyses (means and ranges in wt% of oxides), standard deviations and atomic ratios calculated on 12 oxygen atoms per formula unit (*pfu*) assuming balestraite as completely anhydrous and all vanadium at the pentavalent state, as indicated by the spectroscopic and structural analysis, respectively (see below).

5.2.3.3 Raman Spectroscopy

A Raman spectrum was obtained using a micro/macro Jobin Yvon LabRam HRVIS, equipped with a motorized x-y stage and an Olympus microscope. The backscattered Raman signal was collected with 50× objective and the Raman spectrum was obtained for a randomly oriented crystal. The 632.8 nm line of an He-Ne laser was used as excitation; laser power was controlled by a series of density filters. The lateral and depth resolution were about 2 and 5 μm, respectively. The system was calibrated using the 520.6 cm^{-1} Raman band of silicon before the experimental session. Spectra

were collected with multiple acquisitions (2 to 6) with single counting times ranging between 20 and 180 seconds. The spectrum was recorded using the LabSpec 5 program from 150 to 4000 cm^{-1}.

5.2.3.4 Electron Paramagnetic Resonance

The EPR measurement was carried out on a Bruker ER 200D-SRC spectrometer operating at X-Band (~9.5 GHz) interfaced with DS/EPR software to a PC for data acquisition and handling; the actual operating frequency value was determined by using DPPH radical [2,2-di(4-tert-octyl-phenyl)-1-picrylhydrazyl, g = 2.0037] as external standard. The spectrum was registered inserting the crystal into an amorphous silica tube, at room temperature. Under the adopted operating conditions (100 KHz modulation frequency, 4 db modulation amplitude), the minimum amount of detectable V can be estimated in $5 \cdot 10^{13}$ ions (Burns and Flockhart 1990). This value corresponds to ~0.01% of the total V content in the sample, given the experimental volume (about $19 \cdot 10^{6}$ μm^3, approximately) and the density of the investigated sample.

5.2.4 Results

The crystal structure of balestraite is topologically similar to that of the other trioctahedral micas belonging to the 1*M* polytype; however, the mineral is characterized by unusual geometrical features related to its Li,V - rich chemical composition. Consistently with many Li-rich micas (e.g., Brigatti et al. 2007 and references therein), balestraite crystallizes in the *C*2 space group.

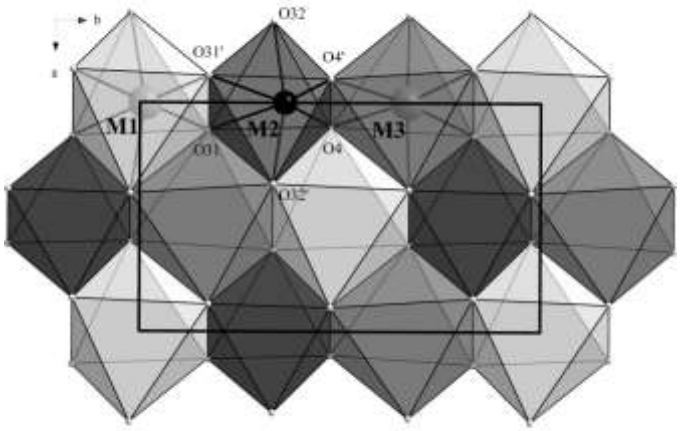

Figure 5.2. The octahedral sheet of balestraite viewed down the *c* axis. M1 and M3 octahedra host Li^{+}, V^{5+} occupies M2.

The reduction of symmetry from the ideal space group *C*2/*m* is related to the ordering of V at one (M2) of the two *cis*-octahedral sites (M2 and M3), whereas Li almost fully occupies the other two sites (Table 5.2, Fig. 5.2). This ordering scheme is consistent with the site scattering (21.6 e^- in M2 vs. 3.0 and 3.6 in M1 and M3, respectively) and the geometry of the three octahedra. The analysis of the Raman spectrum (Fig. 5.3) shows no peaks in the region of the O-H stretching band (3300-3800 cm^{-1}) thus suggesting balestraite to be anhydrous. In this light, charge balance would require all vanadium at the pentavalent state. This feature is indeed confirmed observing the geometry of the M2 polyhedron which exhibits a V-O bond-length distribution characteristic of the valence state +5 (Schindler et al. 2000), showing a [2+2+2] coordination with two short vanadyl bonds (1.66 Å) with O4 in a *cis* arrangement, two longer *equatorial* bonds (1.985 Å) with O32, and the two longest bonds (2.184 Å) with O31 *trans* to the vanadyl anions (Fig. 5.4). Furthermore, EPR spectrum shows no absorption signal due to V^{4+} (the only V species with odd number of unpaired electrons), thus allowing to exclude significant amounts of V^{4+} and making unlikely the presence of V^{3+}.

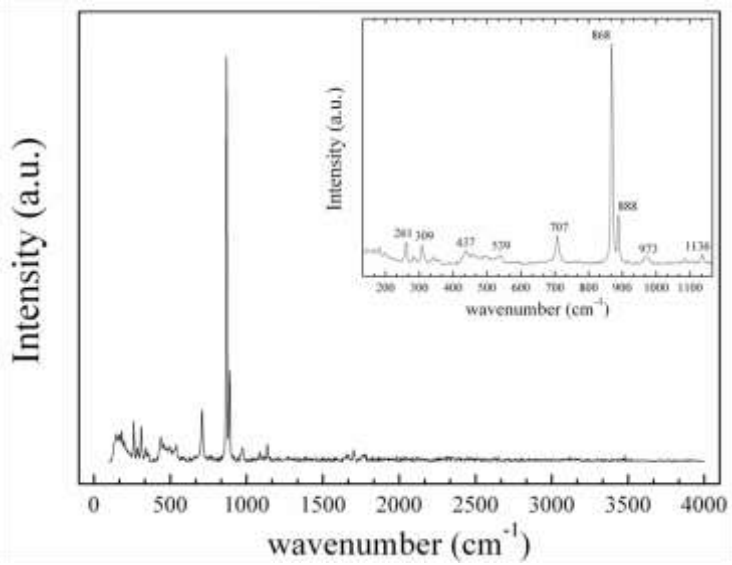

Figure 5.3. Raman spectrum of balestraite.

The octahedral V^{5+} is also supported by a high-wavenumber Raman band (973 cm^{-1}), consistent with what reported by Frost et al. (2005) for symmetric vibrational modes from $V^{5+}O_6$ units in decavanadate minerals, including pascoite (three bands at 991, 965, 958 cm^{-1}) and hummerite (two bands at 999 - 962 cm^{-1}).The empirical formula (based on V as V^{5+} and O4 occupied by O^{2-}) is

$K_{0.99}Li_{2.00}V^{5+}_{0.97}Si_{4.04}O_{12}$ and this result is consistent with the structure refinement and close to the simplified formula of $KLi_2V^{5+}[Si_4O_{10}O_2]$. The electron count calculated on the basis of the empirical formula for the octahedral sites (28.3) is in excellent accord with that obtained by the structure refinements (28.2).

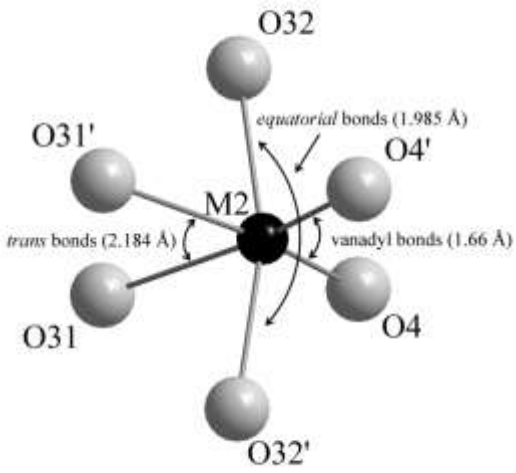

Figure 5.4. [2+2+2]-coordination of V^{5+} in the M2 octahedron.

5.2.5 Discussion

5.2.5.1 Octahedral sheet

<M1-O> and <M3-O> bond lengths (2.08 and 2.10 Å, respectively) are similar to those found for Li-rich octahedra (e.g., Tyrna and Guggenheim 1991; Brigatti et al. 2000, 2007). M1 and M3 octahedra are flattened and less distorted in comparison with M2, which is strongly influenced by the presence of V^{5+} (see Table 5.5 and 5.6 for details). The trioctahedral sheet in balestraite is affected by the ordering of cations with markedly different size and charge, whereas the *oxy* component only marginally affects the octahedral bond lengths. Divalent anions (O^{2-}) at O4 would be expected to increase the electrostatic attraction with all M cations, such as in oxybiotite (Ohta et al. 1982), thus inducing a shortening of all the M-O4 distances. However, this trend occurs only for M2, whereas M1-O4 and M3-O4 are longer than the others (Table 5.5). Thus a high and positive off-center shift value, usually indicating sensible amounts of *oxy* component in trioctahedral *C*2/*m*

micas (Cesare et al. 2003; Mesto et al. 2006; Gianfagna et al. 2007; Matarrese et al. 2008; Scordari et al. 2008, 2010), is only observed for M2 (0.316 Å) whereas a negative value is shown by M3 (-0.198 Å).

Bond valence sums (BVS) for O1, O21, O22, O31 and O32 are all slightly higher than 2.0 v.u. (Table 5.7), whereas the BVS for O4, despite the very short M2-O4 bonds, is 1.74 v.u.. A low value, however, does not require the presence of H, as documented for other anhydrous or partially anhydrous members of the mica group (norrishite, BVS_{O4} = 1.69 v.u., Tyrna and Guggenheim 1991; oxykinoshitalite, BVS_{O4} = 1.54 v.u., Kogarko et al. 2005; oxyphlogopite, BVS_{O4} = 1.61 v.u., Chukanov et al. 2011).

5.2.5.2 Tetrahedral sheet

The tetrahedral sheet of balestraite is characterized by nearly perfect hexagonal rings; the tetrahedral rotation angle α of 0.2° is the lowest value found in natural micas (Brigatti and Guggenheim 2002). This feature is probably related to the small lateral dimensions of the Si_4 tetrahedral sheet compared to the lateral dimensions of the octahedral sheet which, owing to the Li,V composition, is one of the most contracted among the trioctahedral micas leading to very short *a* and *b* cell edges.

Basal oxygen plane is corrugated in a similar manner to that observed in other Li-rich micas (Brigatti and Guggenheim 2002 and references therein) with O1 and O21 atoms drawn towards the octahedral sheet (Δz = 0.087).

Tetrahedra in balestraite are elongated parallel to $c\sin\beta$ with the mean pyramidal edges length longer than the basal edges (2.670 vs. 2.591 Å for T1 and 2.671 vs. 2.603 Å for T2). This difference in length reduces the basal surface and contributes to the decrease of the lateral dimensions of the sheet. Tetrahedra in balestraite are distorted, as indicated by the high values of BLD (bond length distortion) and τ (defined as the mean O_{basal}-T-O_{apical} angle) parameters (Table 5.6). The high BLD values are related to the short T-O_{apical} distances: whereas the mean Si-O bond lengths (1.61 and 1.62 Å for T1 and T2, respectively) are close to the expected tetrahedral Si-O bond length of 1.623 Å on the basis of predictive equation proposed by Baur (1978), the Si-O_{apical} are significantly shorter (1.560 and 1.586 Å for both T1 and T2, respectively). The displacement of Si towards the apical oxygens may be related to high Si content. The high BVS on O1, O21 and O22 (Table 5.7) is not capable of being directly balanced by any other substitutional mechanism. In

contrast, for the apical oxygen atoms, the presence of Si alone in the tetrahedra and V^{5+} in the adjacent octahedron is balanced by the concomitant entry of a monovalent cation (Li).

The magnitude of the tetrahedral distortion, τ, is among the highest ever found in natural micas (Brigatti and Guggenheim 2002): this observation, together with the displacement of Si towards the apical oxygen atom, describes the elongated shape of the tetrahedra. This feature is observed also in norrishite (Tyrna and Guggenheim 1991) and in synthetic polylithionite, $KLi_2AlSi_4O_{10}F_2$ (Takeda and Burnham 1969) and, although to a lesser extent, in tainiolite, $KLiMg_2Si_4O_{10}F_2$ (Toraya et al. 1977) and synthetic cesian tainiolites (Mariychuk et al. 2007; Baumgartner et al. 2009; Koch and Breu 2013).

5.2.5.3 Interlayer

The interlayer is occupied by very regular KO_{12} polyhedra with a short mean bond length of 3.066 Å. One of the most striking feature is the homogeneity of the K-O distances with $<K\text{-}O_{inner}>$ matching $<K\text{-}O_{outer}>$ (Table 5.6). This geometrical arrangement indicates nearly perfect hexagonal symmetry of the tetrahedral sheet and is also related to the small size of the tetrahedra. The interlayer thickness of only 3.26 Å, together with those observed in norrishite (3.27 Å; Tyrna and Guggenheim 1991) and oxykinoshitalite (3.221 Å; Kogarko et al. 2005), is among the lowest values found in trioctahedral micas (Brigatti and Guggenheim 2002) and contributes to the very short length of the *c* cell edge (9.997 Å). The small thickness is related to the absence of electrostatic repulsion usually occurring between the interlayer cation and the hydrogen bonded to O4 and here occupied by a divalent anion alone as first suggested by Cruciani and Zanazzi (1994) and then observed in hydrogen depleted micas of recent investigation (e.g. Schingaro et al. 2011; Scordari et al, 2013).

5.2.6 Constraints on petrogenesis

In terrestrial geological systems, vanadium exists as V^{3+}, V^{4+} and V^{5+}, with V^{5+} relative content increasing with oxygen activity (fO_2) (Canil 2002; Zanetti et al. 2004). The occurrence of 5+ as the dominant valence state of V in balestraite is thus consistent with strongly oxidizing conditions of crystallization, which are supported also by the complete $O^{2-} \rightarrow OH^-$ substitution at the O4 position and by the occurrence of balestraite at the boundary between carbonate-bearing veins and hematite bands. Oxidizing conditions of formation were also argued for mineral assemblages

containing the dehydrogenated end-member amphibole ungarettiite, $NaNa_2(Mn_2^{2+}Mn_3^{3+})Si_8O_{22}O_2$ (Hawthorne et al. 1995). The latter crystallized, like balestraite, during low-*T* metamorphic recrystallization of submarine Mn-rich deposits at the Hoskins mine (Grenfell, New South Wales, Australia). A further linking between the formation of balestraite and ungarettiite, besides the concomitant occurrence of calcite and quartz bands, is represented by their common Mn- and Li-rich mineral assemblage characterized by the presence of braunite, norrishite, and sugilite. As a whole, such a match suggests that both the composition of the manganese deposit and its hydrothermal alteration were similar in the Hoskin and Cerchiara occurrences.

Balestraite and ungarettiite may be assumed to form where host rocks enriched in transition elements reacted with alkaline fluids at low-*T* conditions, thus producing unusual alkali-rich amphiboles and micas completely dehydrogenated and containing highly oxidized transition elements (Mn and V). Further investigations are needed to determine whether the strongly oxidizing conditions controlling the crystallization of balestraite and ungarettiite were the result of a buffering effect exerted by the transition-element-rich host matrix or a primary feature of the flowing fluids, the latter possibly CO_2 rich.

5.2.7 Implications

Vanadium in minerals may be present in variable oxidation states forming polyhedra with different coordination number [e.g. tetrahedral (V^{5+}), trigonal bipyramidal (V^{4+}, V^{5+}) and octahedral (mainly V^{3+} and, to lesser extent, V^{4+} and V^{5+})], and therefore its presence in complex solid solutions adds difficulties in the determination of cation distribution. For the V-members of the mica group, i.e. chernykhite (Ankinovich et al. 1973) and roscoelite (Brigatti et al. 2003b), vanadium is nominally present as V^{3+} (i.r. = 0.64 Å, Shannon 1976). However, variable amounts of V^{4+} and V^{5+} cations, which are similar in radii size (0.58 and 0.54 Å, respectively) may coexist in octahedral sites. According to Ankinovich et al. (1973), in the Ba-bearing muscovites and chernykhite from the Karatau carbonaceous-siliceous schists, micas hosted in rocks enriched in organic matter contain V^{3+}, whereas V^{4+} occurs in micas from rocks poor in organic matter and may sometimes replace V^{3+}. Balestraite, a near V^{5+} end-member, allows the evaluation of the structural effect of V^{5+} within the octahedral sheet in micas.

Moreover, balestraite enlarges the number of dehydrogenated rock forming minerals (amphiboles and micas) containing highly oxidized transition elements. The incorporation in the mica structure of V^{5+} allows for a mechanism to charge balance the incorporation of the *oxy* component in micas.

Table 5.1 Crystallographic data and refinement parameters for balestraite

Crystal data	
a (Å)	5.2024(5)
b (Å)	8.9782(7)
c (Å)	9.997(2)
β (°)	100.40(2)
V (Å^3)	459.3(1)
Polytype	1*M*
Space Group	*C*2
Crystal size (μm^3)	30x220x250
Data collection	
θ_{max} (°)	31.99
total refl. collected	14541
unique refl.	1587
refl. with $I > 3\sigma(I)$	916
structure refinement	
refined parameters	56
R_1 [$F > 2\sigma(F)$] (%)	12.7
R_1 all (%)	13.8
Largest diff. peak and hole (e$^-$/Å^3)	1.09/-1.48

Table 5.2. Atoms, site occupancy factors (s.o.f.), fractional atom coordinates, and equivalent isotropic displacement parameters (Å^2) for balestraite.

Atom	s.o.f.	*x/a*	*y/b*	*z/c*	U_{iso}
K	$K_{1.00}$	0	0.5021(5)	0	0.043(1)
M1	$Li_{1.00}$	0	0.012(3)	½	0.019(4)
M2	$V_{0.93(2)}Li_{0.07}$	0	0.3612(3)	½	0.031(1)
M3	$Li_{0.97(2)}V_{0.03}$	0	0.681(2)	½	0.018(8)
T1	$Si_{1.00}$	0.0766(6)	0.1706(3)	0.2320(4)	0.030(1)
T2	$Si_{1.00}$	0.5820(6)	0.3354(3)	0.2290(3)	0.029(1)
O1	$O_{1.00}$	0.056(2)	0.003(1)	0.1682(8)	0.032(2)
O21	$O_{1.00}$	0.307(2)	0.2535(9)	0.1689(9)	0.029(2)
O22	$O_{1.00}$	0.806(2)	0.2524(9)	0.1601(9)	0.031(2)
O31	$O_{1.00}$	0.123(2)	0.1712(9)	0.3906(8)	0.024(2)
O32	$O_{1.00}$	0.646(2)	0.332(1)	0.3902(8)	0.030(2)
O4	$O_{1.00}$	0.106(2)	0.474(1)	0.3901(9)	0.041(2)

Table 5.3. Observed and calculated X-ray powder diffraction data for balestraite.

			(a)		(b)	
h	*k*	*l*	*d*(Å)	I_{obs}/I_{100}	*d*(Å)	I_{calc}/I_{100}
0	0	1	9.9	50	9.8328	41
0	0	2	4.96	20	4.9164	14
0	2	0	4.51	100	4.4891	40
1	1	0			4.4456	22
-1	1	1	4.34	40	4.3127	49
0	2	1	4.11	25	4.0836	29
1	1	1	3.85	10	3.8315	17
-1	1	2	3.60	40	3.5893	100
0	2	2	3.34	30	3.3151	66
0	0	3	3.30	30	3.2776	32
1	1	2	3.08	35	3.0668	93
-1	1	3	2.877	10	2.8611	26
0	2	3	2.662	15	2.6471	29
-2	0	1	2.592	70	2.5927	15
1	3	0			2.5833	39
2	0	0	2.574	70	2.5585	23
-1	3	1			2.5565	38
1	1	3			2.4602	4
0	0	4	2.460	10	2.4582	4
1	3	1			2.4444	8
-1	3	2	2.385	70	2.3778	39
2	0	1			2.3738	25
-1	1	4	-	-	2.3101	7
-2	2	1	2.251	10	2.2451	9
2	2	0	2.232	10	2.2228	12
0	4	1	2.198	20	2.1883	22
-2	2	2	2.167	10	2.1563	10
-1	3	3	2.133	15	2.1252	18
2	0	2	2.13	s	2.1183	11
2	2	1	2.10	s	2.0985	8
0	0	5	1.976	25	1.9666	15
-2	0	4	-	-	1.9579	5
1	3	3	1.957	10	1.9446	12
-2	2	4	1.817	5	1.7947	4
-3	1	1	1.703	<5	1.7026	4
0	4	4	1.657	<5	1.6575	6
1	5	1			1.6533	4
-1	3	5	1.642	15	1.6384	26
2	0	4	1.63	s	1.6315	12
2	4	1			1.6309	8
-3	1	3	1.614	5	1.6124	4

			(a)		(b)	
h	*k*	*l*	*d*(Å)	I_{obs}/I_{100}	*d*(Å)	I_{calc}/I_{100}
-2	4	3	1.583	5	1.5786	11
1	5	2			1.5732	4
-1	5	3	1.546	5	1.5432	6
-3	1	4	1.512	<5	1.5153	4
-2	0	6			1.5093	5
3	1	2			1.5066	6
-3	3	1	1.503	50	1.5004	23
1	3	5			1.5002	8
0	6	0	1.486	5	1.4964	10
2	2	5	-	-	1.3701	5
-2	0	7	1.338	5	1.3374	6
1	3	6			1.3301	12
-4	0	1	-	-	1.2989	4
-4	0	2	-	-	1.2964	4
-2	6	1	1.299	10	1.2960	10
2	6	0			1.2917	7
-3	3	5	1.284	5	1.2842	4

(a) = observed diffraction pattern obtained by converting the diffraction rings into a conventional XRD pattern; (b) = calculated diffraction pattern obtained from structural data (only reflections with $I_{calc}/I_{100} \geq 4$ are listed); s = shoulder of a peak.

Table 5.4. Electron microprobe analyses (means and ranges in wt% of oxides) and atomic ratios (on the basis of 12 oxygen atoms) of balestraite

	mean	range	atom	atomic ratios
K_2O	11.24	11.19 – 11.28	K	0.99
Li_2O*	7.20	7.04 – 7.46	Li	2.00
V_2O_5	21.15	21.03 – 21.28	V	0.97
SiO_2	58.46	58.06 – 58.76	Si	4.04
total	98.05		$\Sigma_{cations}$	8.00

Note: * Li determined by LA-ICP-MS (three point analyses on different spots); Mn_2O_3 up to 0.12 wt% corresponding to 0.006 atoms per formula units.

Table 5.5. Bond distances (Å) for balestraite

M1		**M2**		**M3**	
O31$^{i, ii}$	1.97(2)	O4$^{i, ii}$	1.66(1)	O32$^{v, vi}$	1.98(2)
O32$^{iii, iv}$	2.17(2)	O32$^{vii, xiii}$	1.985(9)	O31$^{v, vi}$	2.067(8)
O4$^{iii, iv}$	2.17(1)	O31$^{i, ii}$	2.184(8)	O4$^{i, ii}$	2.27(2)
mean	2.10	*mean*	1.943	*mean*	2.10
T1		**T2**		**K**	
O31^{i}	1.560(8)	O32^{i}	1.586(9)	O22$^{viii, xiv}$	3.031(9)
O22^{vii}	1.63(1)	O1^{xii}	1.620(9)	O22$^{vi, ix}$	3.038(9)
O1^{i}	1.63(1)	O21^{i}	1.624(9)	O21$^{i, x}$	3.068(9)
O21^{i}	1.632(9)	O22^{i}	1.637(9)	O1$^{ii, xi}$	3.074(8)
mean	1.613	*mean*	1.617	O21$^{ix, xv}$	3.092(9)
				O1$^{ix, xv}$	3.092(8)
				mean	3.066

Symmetry codes: (*i*) *x*, *y*, *z*, (*ii*) −*x*, *y*, −*z*+1; (*iii*) *x*−½, *y*−½, *z*, (*iv*) −*x*+½, *y*−½, −*z*+1; (*v*) −*x*+½, *y*+½, −*z*+1; (*vi*) *x*−½, *y*+½, *z*, (*vii*) *x*−1, *y*, *z*, (*viii*) −*x*+1, *y*, −*z*, (*ix*) −*x*+½, *y*+½, −*z*, (*x*) −*x*, *y*, −*z*, (*xi*) −*x*−½, *y*+½, −*z*, (*xii*) *x*+½, *y*+½, *z*, (*xiii*) −*x*+1, *y*, −*z*+1; (*xiv*) *x*+1, *y*, *z*, (*xv*) *x*+½, *y*−½, *z*.

Table 5.6. Selected structural parameters for balestraite

Whole layer		**Oct. sheet**	
Δ_{TM} (Å)	0.298	V_{M1} (Å^3)	12.03
β_{ideal}	99.989	V_{M2} (Å^3)	9.54
intralayer shift	-0.347*a*	V_{M3} (Å^3)	12.10
		ψ_{M1} (°)	59.147
Interlayer		ψ_{M2} (°)	56.279
$V(KO_{12})$ (Å^3)	57.76	ψ_{M3} (°)	59.185
t_{int} (Å)	3.259	OAV_{M1}	70.90
<K-O>$_{inner}$ (Å)	3.066	OAV_{M2}	58.76
<K-O>$_{outer}$ (Å)	3.066	OAV_{M3}	71.22
		OQE_{M1}	1.0229
Tet. sheet		OQE_{M2}	1.0295
α (°)	0.15	OQE_{M3}	1.0251
Δz (Å)	0.087	BLD_{M1}	4.227
τ_{T1} (°)	113.54	BLD_{M2}	9.712
τ_{T2} (°)	112.50	BLD_{M3}	5.204
TAV_{T1}	21.62	ELD_{M1}	5.187
TAV_{T2}	11.66	ELD_{M2}	1.671
TQE_{T1}	1.0047	ELD_{M3}	5.238
TQE_{T2}	1.0026	$Shift_{M2}$(Å)	+0.316
BLD_{T1}	1.643	$Shift_{M3}$(Å)	-0.198
BLD_{T2}	0.951	$t_{M(O3)}$ (Å)	2.155
V_{T1} (Å^3)	2.14	$t_{M(O4)}$ (Å)	2.161
V_{T2} (Å^3)	2.16	$t_{M(O3-O4)}$ (Å)	2.157
t_{tet} (Å)	2.221		

Notes: see Table 3.3

Table 5.7. Bond-valence (*v.u.*) arrangement for balestraite

	K	M1 (Li)	M2 (V^{5+})	M3 (Li)	T1	T2	Σ O
O1	$0.078^{\times 2\downarrow}$/$0.075^{\times 2\downarrow}$				1.027	1.056	2.24
O21	$0.080^{\times 2\downarrow}$/$0.075^{\times 2\downarrow}$				1.022	1.044	2.22
O22	$0.086^{\times 2\downarrow}$/$0.088^{\times 2\downarrow}$				1.016	1.008	2.20
O31		$0.256^{\times 2\downarrow}$	$0.357^{\times 2\downarrow}$	$0.197^{\times 2\downarrow}$	1.241		2.05
O32		$0.149^{\times 2\downarrow}$	$0.611^{\times 2\downarrow}$	$0.248^{\times 2\downarrow}$		1.157	2.17
O4		$0.148^{\times 2\downarrow}$	$1.476^{\times 2\downarrow}$	$0.114^{\times 2\downarrow}$			1.74
	0.96	1.11	4.89	1.12	4.31	4.27	

Note: calculated from the bond-valence curves of Brese and O'Keeffe (1991) assuming the ideal formula $KLi_2V^{5+}Si_4O_{10}O_2$.

5.3 A new Mn-rich dioctahedral mica

5.3.1 Introduction

Figure 5.5.Detail of the rock sample where the Mn-rich mica (orange-brown mineral) was found (L. Ceccantini photo); field of view is 40 mm.

An orange-brown mineral with a micaceous character was found in the metacherts of the ophiolitic sequences at Cerchiara mine, Eastern Liguria (Italy). The phase is constituted of thin and extremely elongated lamellae in radial aggregates. The mineral is associated with calcite, ematite and braunite (Fig.s 5.5 and 5.6).

Figure 5.6. Mn-rich mica associated with calcite and braunite (L. Ceccantini photo); field of view is 2 mm

The lamellae are so elongated to resemble, at a glance, acicular crystals. The mineral is transparent with silky luster and perfect {001} cleavage. Its color is darker in aggregates. It is moderately pleochroic, from orange to greenish yellow. Calculated density is 3.042 g/cm^3 on the base of empirical formula and unit-cell dimensions determined by powder X ray diffraction (see below).

Preliminary analyses obtained by energy-dispersive spectrometry (EDS) on a polished section indicated a very high Si, Mn and Mg content, a rather high concentration of F and low Al and Fe. High Mn concentrations in the mica group minerals are quite rare, although several Mn-bearing micas do actually exist. Shirozulite (Ishida et al., 2004) is the Mn analogue of annite, produced by the substitution of Mn^{2+} for Fe^{2+}; masutomilite (Harada et al., 1976) derives from the same Mn^{2+} for

Fe^{2+} substitution in "zinnwaldite"; norrishite (Eggleton and Ashley, 1989) is a trioctahedral mica with the M2 site mainly occupied by Mn^{3+} and M1 by Li. Kinoshitalite, polylithionite and hendricksite have been reported to bear significantly high Mn amounts (Tracy and Beard, 2003; Boggs et al., 1992; Guggenheim et al., 1983; respectively); montdorite (Robert and Maury, 1979) is an uncommon Mn-bearing, tetrasilicic transitional mica with Mn content up to ~0.7 apfu.

However, only in rare cases these minerals reach the ideal end-member composition (Tischendorf et al., 2007). Therefore the mineral was considered interesting enough to proceed with additional examinations.

5.3.2 Experimental Details

5.3.2.1 X-ray powder diffraction

Numerous attempts to perform single crystal X-ray analysis were unsuccesful. Therefore, several crystals of the orange-brown phase were handpicked from the rock sample and crushed under acetone to prevent oxidation of the mineral. Given the scarce amount of material, it was possible to retrieve only a small amount of powder. The resulting powder was not ideal since it was still possible to recognize small elongated fragments of the phase; however, given the scarcity of material, this product was considered suitable for the collection of an X-ray diffraction spectrum.

The diffraction spectrum was measured on a Bruker D8-Advance diffractometer with "Da Vinci" design equipped with Cu$K\alpha$ radiation, θ-θ goniometer and a multichannel fast detector in the range $8 < 2\theta < 70°$. The spectrum is shown in Figure 5.7. Background was removed from the spectrum by using standard polynomials through the software *Rex.Cell* (Bortolotti and Lonardelli, 2013). Determination of peaks position was initially carried out in *Rex.Cell* by means of an automated filtering/second-derivative approach based on the Savitzky–Golay method (Savitzky and Golay, 1964) and then carefully checked for incorrectly added peaks.

Finally, *d* values calculated from fitted peak positions were used to refine the unit-cell parameters using the software *UnitCell* (Holland and Redfern, 1997). The resulting monoclinic cell is: $a = 5.15(1)$, $b = 8.92(1)$, $c = 10.30(1)$, $\beta = 102.0(1)$. Table 5.8 lists measured and calculated *d* values.

Figure 5.7. X-ray powder diffraction pattern of the Mn-bearing mica

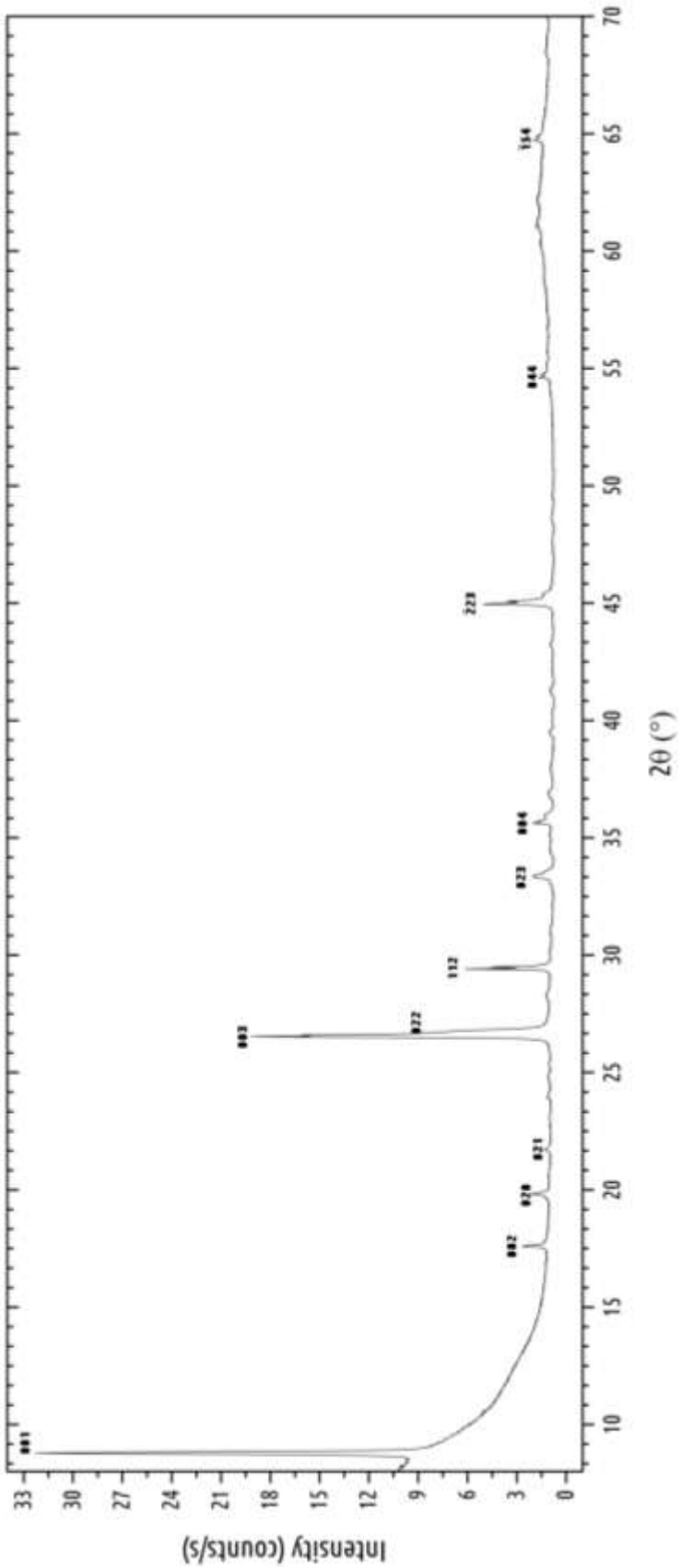

Table 5.8. observed and calculated *d* spacings

h k l	$d_{(obs)}$ (Å)	$d_{(calc)}$ (Å)	*I*
0 0 1	10.055	10.078	s
0 0 2	5.033	5.039	w
0 2 0	4.482	4.458	w
0 2 1	4.091	4.077	w
0 0 3	3.359	3.359	s
0 2 2	3.328	3.339	m
1 1 2	3.034	3.045	m
0 2 3	2.686	2.683	w
0 0 4	2.517	2.519	w
-2 2 3	2.015	2.011	m
0 4 4	1.679	1.669	w
-1 5 4	1.439	1.445	w

Notes: **w, m, and s stand for weak, medium and strong intensities, respectively.**

5.3.2.2 Transmission Electron Microscopy

TEM was performed with a JEOL 2010 microscope, working at 200kV and equipped with LaB_6 electron source, ultra-high resolution (UHR) pole pieces and Oxford ISIS energy dispersive X-ray (EDX) detector. Images and diffraction patterns were recorded with an Olympus Tengra camera (14 bit, 2048x2048 pixel) and analyzed by iTEM software. Powdered sample was dispersed on a Cu mesh. Electron diffraction tomographic data were acquired in a tilt range of +/-25° using a JEOL double tilt holder, using a SAED aperture of 20 µm (equivalent to an illuminated sample area of about 200 nm). Data analysis was performed using ADT3D software (Kolb et al., 2011).

5.3.2.3 Chemical analyses

A crystal of about 200 x 80 x 80 µm was embedded in epoxy and polished for electron microprobe analysis. EMPA analyses were performed using a JEOL JXA-8600 instrument in wavelength dispersion mode at 15 KV, 10 nA beam current and 5 µm beam size.

The following standards were used: albite (Si*K*α), plagioclase (Al*K*α), bustamite (Mn*K*α), olivine (Mg*K*α), ilmenite (Fe*K*α), sanidine (K*K*α), fluorite (F*K*α).

In situ analyses of the content of Li were carried out using laser-ablation inductively-coupled-plasma mass-spectrometry (LA-ICP-MS). The laser probe consists of a Q-switched Nd:YAG laser,

model Quantel (Brilliant), whose fundamental emission in the near-IR region (1064 nm) was converted into 266 nm wavelength using two harmonic generators. Spot diameter was in the range of 40-50 μm. The ablated material was analyzed by using an Elan DRC-e quadrupole mass spectrometer. Helium was used as carrier gas and mixed with Ar downstream of the ablation cell. Data reduction was carried out using the Glitter Software. NIST SRM 610 was analyzed as external standard, while the SiO_2 has been used as internal standard. Precision and accuracy were assessed from repeated analyses of the BCR-2g, NIST SRM 612 and 610 standards and resulted better than 3%. Full analytical details are reported in Tiepolo et al. (2005) and Miller et al. (2007). Chemical analyses of major elements are reported in Table 5.9 (means and ranges in wt% of oxides).

Table 5.9 – Chemical analyses (means and ranges, wt% oxides)

	wt %	Range
SiO_2	55.90	<54.34 - 56.84>
Al_2O_3	1.20	<0.37 – 2.66>
MnO	19.32	<15.97-23.78>
MgO	7.75	<5.56-9.10>
FeO	0.42	<0.22-0.65>
K_2O	9.37	<8.48-9.85>
Li_2O	0.71	<0.61-0.78>
F	0.35	<0.25-0.52>
Total	95.02	

5.3.3 Results and discussion

5.3.3.1 TEM study

The thin lamellae that characterize the mineral at a macroscopic scale are actually observed with the same features at a scale many orders of magnitude lower. Figures 5.8 a and b show the *HR*-TEM images; as we can see, the crystals of this phase tend to fray in bended lamellae that can reach thicknesses as thin as 20 nm. Figures 5.9 a, b and c show the electron diffraction pattern along a^*, b^*, and c^* respectively. The distinguishing feature of the pattern is the strong diffuse scattering of reflections along c^* , thus making unreliable the determination of the c parameter. Diffraction spots are compatible with a monoclinic C-centered lattice with unit-cell parameters as follows: a = 5.4(1), b = 9.1(2), c = 9.8(2), β = 101.5(10).

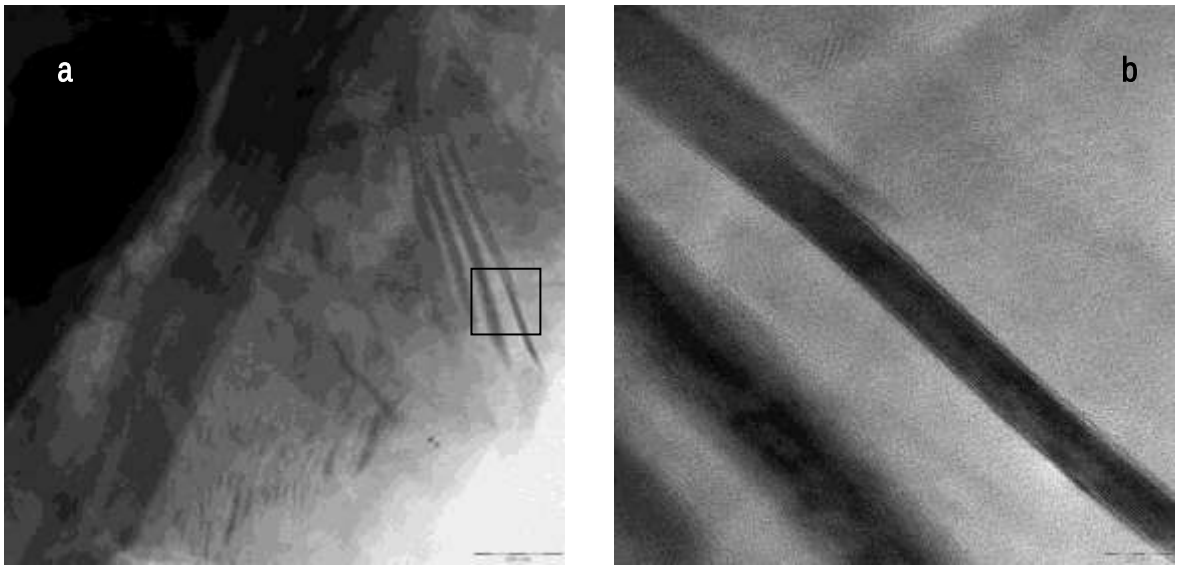

Figure 7.2.4 a) High Resolution-TEM images of the thin fringes formed by the new mineral and b) magnification of the box in a)

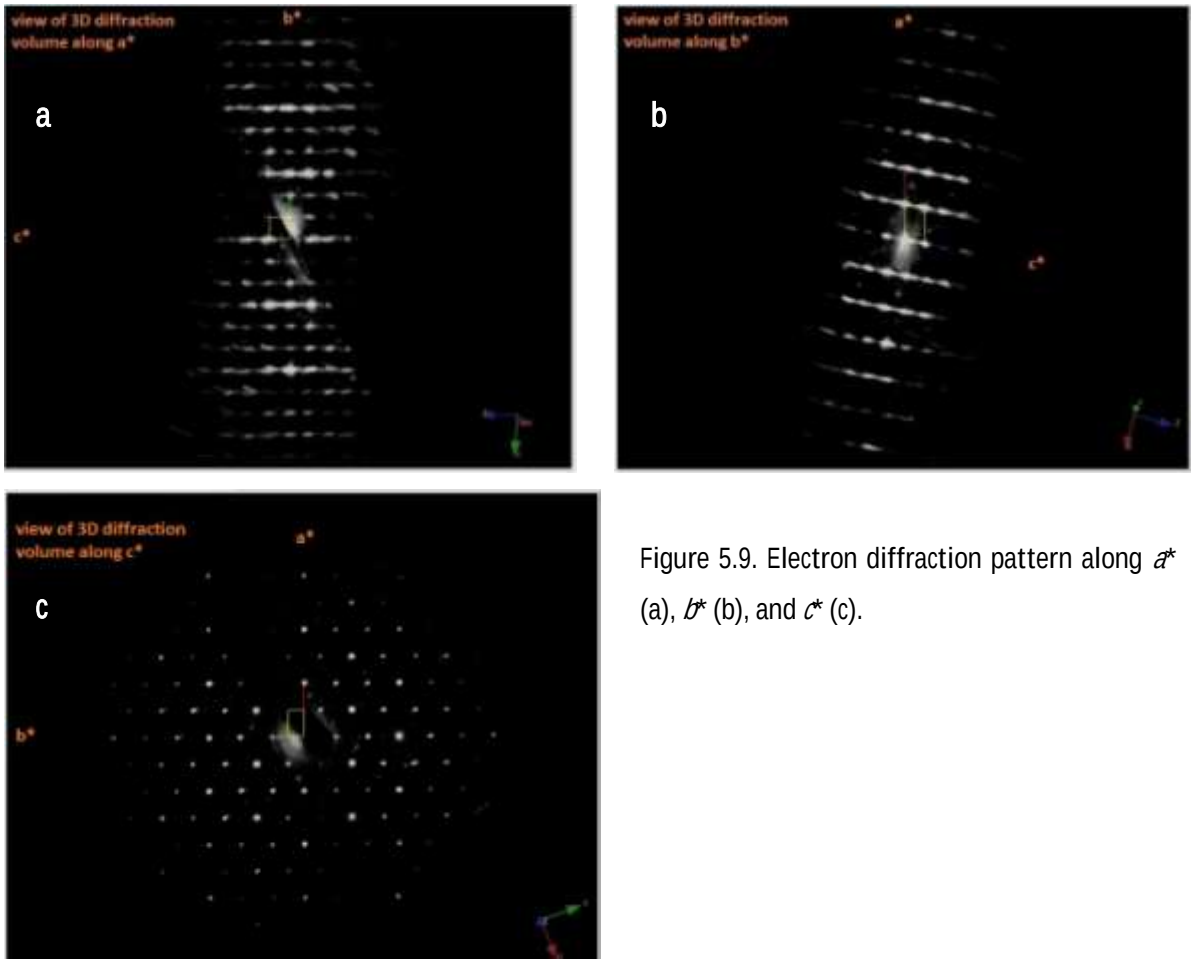

Figure 5.9. Electron diffraction pattern along *a** (a), *b** (b), and *c** (c).

No evidence of a *c* glide plane along *c** was found. Unit-cell parameters are in fair agreement with those derived from the powder pattern as regards *b* cell edges, while there is a stronger discrepancy between the length of *a* and *c* derived from the two techniques.

5.3.3.2 Chemistry

Formula calculation for this mineral is undoubtedly a difficult task. Chemical analyses highlight an elevated content of Mn, which can be present at different valence states (+2, +3, +4), other than a minimum amount of Fe. Mn in micas is commonly reported as Mn^{2+} although there are rare minerals, such as norrishite, with trivalent Mn; however, given the strongly oxidizing conditions assessed in Cerchiara mine (see paragraph 5.2), the presence of Mn^{4+} has to be taken into account. Moreover, the absence of a direct determination of the hydrogen content obviously adds uncertainties to our calculations. Furthermore, we can infer from diffraction data that, given the small value of *b*, this phase likely has a dioctahedral character. In consideration of the fact that it is very common for dioctahedral Li-rich micas to show a partial occupancy of the M1 *trans* site, It is not possible to normalize our data on the sum of tetrahedral and octahedral cations. Several normalization schemes were then used. First, data were normalized to a fixed negative charge, assuming different oxidation states for Mn; results are listed in Table 5.10.

Table 5.10. Formulae recalculations based on a fixed negative charge

	a	b	c	d	e
Si	4.11	3.89	3.7	3.87	4.03
Al	0.10	0.10	0.09	0.10	0.10
Mn	1.2	1.14	1.08	1.13	1.18
Mg	0.85	0.8	0.76	0.8	0.83
Fe	0.03	0.02	0.02	0.02	0.03
K	0.88	0.83	0.79	0.83	0.86
Li	0.21	0.20	0.19	0.20	0.21
F	0.08	0.08	0.07	0.08	0.08
OH	1.92	1.92	1.93	0.92	0.00

Notes: a) 22 negative charges and Mn^{2+}, b) 22 negative charges and Mn^{3+}, c) 22 negative charges and Mn^{4+}, d) 23 negative charges and Mn^{4+}, e) 23.92 negative charges and Mn^{4+}.

Normalizations based on 22 negative charges (columns a, b and c assuming Mn at di-,tri-, and tetravalent valence state, respectively) lead to good sums for tetrahedral and octahedral cations

sums only when Mn charge is fixed to 3+. Columns d and e show instead normalizations based on 23 and 23.92 negative charges and assuming all Mn as Mn^{4+}; we observe that these formulas, although with a slight deficiency or excess for tetrahedral cation sums for methods d and e respectively, lead to plausible results. Consequently, it seems reasonable to exclude Mn^{2+} from our hypotheses and a second normalization scheme is then introduced. H_2O content was estimated from EMPA data in both the cases of trivalent and tetravalent Mn and formulas were then calculated on the basis of 12 (O, OH, F, Cl) (Table 5.11). Both formulas result well balanced, with a discrepancy between positive and negative charges minor than 0.02 e^-. Tetrahedra are occupied mainly by Si with minor amounts of Al; octahedral cation sums are always higher than 2 while the interlayer site occupancy shows high deficiency.

Table 5.11 Oxydes (wt%) with estimated H_2O content and formulae recalculation based on 12 (O+F+OH)

	a	b		c	d
SiO_2	55.90	55.90	Si	3.99	3.97
Al_2O_3	1.20	1.20	^{IV}Al	0.01	0.03
Mn_2O_3/MnO_2	21.50	23.68	^{VI}Al	0.09	0.07
Fe_2O_3	0.47	0.47	$Mn^{3+/4+}$	1.17	1.16
MgO	7.75	7.75	Fe^{3+}	0.03	0.03
K_2O	9.37	9.37	Mg	0.82	0.82
Li_2O	0.71	0.71	K	0.85	0.85
F	0.35	0.35	Li	0.2	0.2
Total	97.10	99.28	F	0.08	0.08
H_2O*	2.90	0.72	OH	1.38	0.34
			O	10.54	11.58
			Σ (^{IV}Al+Si)	4.00	4.00
			Σ (^{VI}Al+Mn+Fe+Mg+Li)	2.31	2.28

Notes: a) values assuming all Mn as 3+, b) values assuming all Mn as 4+, c)and d) formulae calculated from data in a) and b) respectively.

It should be kept in mind, however, that values of octahedral sums "transitional" between dioctahedral and trioctahedral micas are common, especially for Li-bearing micas (*e.g.* Levinson, 1953; Foster, 1960; Černý et al., 1995; Roda-Robles et al., 2006; Van Lichtervelde et al. 2008; Vieira et al. 2011; Martins et al., 2012). The experimental work of Monier and Robert (1986) also showed how the gap between dioctahedral and trioctahedral micas reduces with the progressive increase of the content of Li. Du Bray (1994) and Foord et al. (1995) also suggested that the intermediate

occupancy of the octahedral sheet could be indicative of a mixed-layer form, involving both dioctahedral and trioctahedral structures, and could be a sign of disequilibrium crystallization. Moreover, the presence of a minor amount of Li in the interlayer cavity could also be hypothesized (Robert et al., 1983; Mesto et al., 2006).

OH contents as low as those indicated in column d have never been reported before in the literature for dioctahedral micas; furthermore the sum of oxides very close to 100% in the case of the presence of all Mn as 4+, does not allow us to exclude the complete absence of H_2O in the structure. No natural dehydroxylate dioctahedral micas have been reported in nature so far (to the author's knowledge); nonetheless, many studies of thermally dehydroxylated micas have been performed (e.g. Wardle and Brindley, 1972; Guggenheim et al., 1987; Guggenheim, 1990; Kogure and Drits; 2010; Derkowski et al., 2012). These studies demonstrate that the behavior upon loss of H_2O for trioctahedral and dioctahedral micas is very different. The most accepted model of dehydroxylation in dioctahedral micas involves indeed H_2O loss, and not H_2 loss only. This leads to a different "dioctahedral" structure where the "octahedral" cations are actually in a fivefold coordination.

Conclusively, based on our data, we can hypothesize that the crystal-chemical formula of this Mn-rich mica ranges between $KMn^{3+}MgSi_4O_{10}(OH)_2$ (i.e the Mn^{3+} analogue of celadonite with Mn^{3+} substituting for Fe^{3+}) and a partially dehydrogenated end-member mica with Mn^{4+} and a halved OH content, summarized by the ideal formula $KMn^{3+}_{(1-x)}\ Mn^{4+}_{x}\ Mg\ Si_4O_{10}O_{(x)}(OH)_{(2-x)}$.

Finally, in case of a completely dehydrogenated mica, a formula such as $KMn^{4+}\ Mg\ Si_4O_{10}O_{1.5}$ could be hypothesized.

In this light, we regret we could not get structural details on such a particular phase and more attempts will be made to get less ambiguous information at least regarding water content and Mn oxidation state.

6 Concluding remarks

Micas from lamproitic rocks from the western Mediterranean area have been studied by means of multiple techniques in order to reduce the number of unknown variables and, consequently, uncertainties in the interpretation of data.

All the studied crystals belong to the phlogopite-annite solid solution and crystallize in the 1*M* polytype, except for micas from Torre Alfina, where both 1*M* and $2M_1$ polytypes have been found. In micas from Torre Alfina, 1*M* and $2M_1$ crystals radically differ in chemical composition: $2M_1$ crystals have a Fe/Mg ratio close to ~ 0.8 and high contents of Ti and Al; 1*M* micas show a very different chemical composition with Mg being by far the most abundant octahedral cation. The two populations also show a marked difference in the *oxy* component: $2M_1$ samples are in fact *oxy*-phlogopites with a sum of OH and F of about 0.5 apfu while for 1*M* samples, this sum reaches ~1.3 apfu .Together with the extreme grade of dehydrogenation, the most peculiar aspect of $2M_1$ samples is the high Al content in both tetrahedral and octahedral sites. This yields to the structural distortions already pointed out in paragraph 4.6 and 4.7 where the structural characteristics of T1 and T2 were averaged. Averaging the parameters related to the two different sites was possible since the high amount of Al does not seem to lead to any ordering either at the octahedral site, or at the tetrahedral sites, with tetrahedra T1 and T2 showing very similar size and distortional parameters (Table 3.4). The remarkable differences in the structural characteristics of the two populations do not seem to be related in any case to the polytype they belong to. Their crystal chemical features are in fact substantially regulated only by their chemistry as we can infer from the crystal-chemical features discussed earlier. Thus $2M_1$ samples present the typical characteristics of heavily *oxy*-substituted micas of similar compositions belonging to the 1*M* polytype with the contribution of the effects induced by high contents of Al. Most likely, in the case of our samples, given the extremely different chemical composition, the finding of the different polytypes has to be ascribed to the crystallization of the latter in two different stages characterized by a substantially different physico-chemical environment. According to the data reported by Conticelli et al. (1998), $2M_1$ crystals from Torre Alfina represent the phenocrysts from these lavas, while 1*M* crystals represent the mica population of the groundmass.

The studied crystals show distinctive chemical and structural features. The entry of high charge cations, especially Ti, in the structure is mainly balanced via the *oxy* mechanism, which involves the

release of H_2. In particular, our data confirm that Ti preferentially partitions into the M2 site. Incorporation of Ti via the *oxy* mechanism is an important factor for two reasons: the presence of Ti is indeed known to extend the thermal stability of brown micas, increasing the melting temperature of up to 80 °C (Stevens et al., 1997); furthermore, H_2 released in the reaction can, as suggested by Feeley and Sharp (1996), react with the O_2 present in the magma, modifying its volatile content. Sassi et al. (2008) suggested that there could be a petrologic control on the type of mechanism of Ti incorporation in micas. Specifically, Sassi et al. (2008) proposed that the main controlling factor is the H_2O activity and that Ti-*oxy* substitution dominates in H_2O-free or H_2O-poor environment.

Finally, a stimulating topic emerged from this work is the study of the complex interactions occurring at the O4 site of micas, which result in a crystal-chemical environment able to reflect some of the most important variations in the whole mica structure. In this light, the study of micas characterized by peculiar substitutions in octahedral and tetrahedral sites and by extreme compositions of the anionic site, such as those described in chapter 5, is of particular interest.

7 References

Abrecht, J. and Hewitt, D.A. (1988) Experimental evidence on the substitution of Ti in biotite. American Mineralogist, 73, 1275–1284.

Ankinovich, S.G., Ankinovich, Ye.A., Rozdestvenskaya, I.V., and Frank-Kamenetsky, V.A. (1973) Chernykhite, a new barium-vanadium mica from northwestern Karatau. International Geology Review, 15, 641-647.

Ankinovich, E.A., Bekenova, G.K., Kompaneitsev, V.P., Kotelnikov, P.E., and Savostin, B.A. (2001) Vanadium and vanadium-bearing micas from the carbonaceous-siliceous formation of the Bolshoi Karatau Ridge (South Kazakhstan). 2. V^{4+}-Ba phengite. Vanadium-bearing muscovite and phengite. Geologia Kazakhstana, 2, 13-23 (in Russian).

Avanzinelli, R., Lustrino, M., Mattei, M., Melluso, L., and Conticelli, S. (2009). Potassic and ultrapotassic magmatism in the circum-Tyrrhenian region: significance of carbonated pelitic vs. pelitic sediment recycling at destructive plate margins. Lithos, 113, 213-227.

Babushkina, M.S., Lepekhina, E.N., Nikitina, L.P., Ovchinnikov, N.O., and Lokhov, K.I. (2000) Crystal structure defects of micas from lamproites (Mossbauer and infrared spectroscopy data). Doklady Akademii Nauk, **371**, 797-801. (in Russian)

Backhaus, K. O. (1983). Structure refinement of an 1*M* lepidolite. Crystal Research and Technology, 18, 1253-1260.

Bailey, S. W. (1984). Classification and structures of the micas. Reviews in Mineralogy and Geochemistry, 13, 1-12.

Baumgartner, A., Butterhof, C., Koch, S., Mariychuk, R., and Breu, J. (2009) Melt synthesis and characterization of synthetic Mn-rich tainiolite. Clays and Clay Minerals, 57, 271-277.

Baur, W. H. (1978) Variation of mean Si-O bond lengths in silicon-oxygen tetrahedra. Acta Crystallographica, B34, 1751-1756.

Benincasa E., Brigatti, M.F., Poppi, L., and Barredo, F.B. (2003) Crystal chemistry of dioctahedral micas from peraluminous granites: the Pedrobernardo pluton (Central Spain). European Journal of Mineralogy, 15, 543-550.

Benito, R., López-Ruiz, J., Cebriá, J. M., Hertogen, J., Doblas, M., Oyarzun, R., and Demaiffe, D. (1999). Sr and O isotope constraints on source and crustal contamination in the high-K calc-alkaline and shoshonitic Neogene volcanic rocks of SE Spain. Lithos, 46, 773-802.

Boggs, R.C. (1992) A manganese-rich miarolitic granite pegmatite assemblage from the Sawtooth batholith, South central Idaho, U.S.A. Abstracts: International Symposium "Lepidolite 200", Novè Město na Moravě/Czechoslovakia, 29.8.-3.9.1992, 15-16.

Bortolotti, M., and Lonardelli, I. (2012). ReX. Cell: a user-friendly program for powder diffraction indexing. Journal of Applied Crystallography, 46, 259-261.

Brese, N.E., and O'Keeffe, M. (1991) Bond-valence parameters for solids. Acta Crystallographica, B47, 192-197.

Brigatti, M. F., and Davoli, P. (1990). Crystal-structure refinements of 1*M* plutonic biotites. American Mineralogist, 75, 305-313.

Brigatti, M. F., Galli, E., and Poppi, L. (1991). Effect of Ti substitution in biotite-1*M* crystal chemistry. American Mineralogist, 76, 1174-1183.

Brigatti, M. F., and Poppi, L. (1993). Crystal chemistry of Ba-rich trioctahedral micas-1*M*. European Journal of Mineralogy, 5, 857-871.

Brigatti, M.F., Medici, L., and Poppi, L. (1996a) Refinement of the structure of natural ferriphlogopite. Clays and Clay Minerals, 44, 540–545.

Brigatti, M.F., Medici, L., Saccani, E., and Vaccaro, C. (1996b) Crystal chemistry and petrologic significance of Fe^{3+}-rich phlogopite from the Tapira carbonatite complex, Brazil. American Mineralogist, 81, 913–927.

Brigatti, M.F., Frigieri, P., Ghezzo, C., and Poppi, L. (2000a): Crystal chemistry of Al-rich biotites coexisting with muscovites in peraluminous granites. American Mineralogist., 85, 436-448.

Brigatti, M.F., Lugli, C., Poppi, L., Foord, E.E., and Kile, D.E. (2000b): Crystal chemical variations in Li- and Fe-rich micas from Pikes Peak Batholith (central Colorado). American Mineralogist., 85, 1275-1286.

Brigatti, M.F., Medici, L., Poppi, L., and Vaccaro, C. (2001) Crystal chemistry of trioctahedral micas-1*M* from the Alto Paranaíba Igneous Province, southeastern Brazil. Canadian Mineralogist, 39, 1333–1345.

Brigatti, M. F., and Guggenheim, S. (2002). Mica crystal chemistry and the influence of pressure, temperature, and solid solution on atomistic models. In A. Mottana, F.P. Sassi, J.B. Thompson Jr., and S. Guggenheim, Eds., Micas: crystal chemistry and metamorphic petrology. Reviews in Mineralogy and Geochemistry, 46, 1-97.

Brigatti, M. F., Guggenheim, S., and Poppi, M. (2003a). Crystal chemistry of the 1*M* mica polytype: The octahedral sheet. American Mineralogist, 88, 667-675.

Brigatti, M.F., Caprilli, E., Marchesini, M., and Poppi, L., (2003b) The crystal structure of roscoelite-1*M*. Clays and Clay Minerals, 51, 301-308.

Brigatti, M.F., Caprilli, E., Funiciello, R., Giordano, G., Mottana, A., and Poppi, L. (2005) Crystal chemistry of ferroan phlogopites from the Albano maar lake zone (Colli Albani volcano, central Italy). European Journal of Mineralogy, 17, 611–621.

Brigatti, M.F., Mottana, A., Malferrari, D., and Cibin, G. (2007) Crystal structure and chemical composition of Li-, Fe-, and Mn-rich micas. American Mineralogist, 92, 1395-1400. Burns, D.T., and Flockhart, B.D. (1990) Application of Quantitative EPR [and Discussion]. Philosophical Transactions of the Royal Society of London A, 333(1628), 37- 48.

Cabella, R., Lucchetti, G., and Palenzona A. (1990) Al-rich, Fe-poor manganoan sugilite in a pectolite-bearing assemblage from Cerchiara Mine (Northern Appennines, Italy). Neues Jahrbuch für Mineralogie Monatshefte, 1990, 443-448.

Cabella, R., Lucchetti, G., and Marescotti, P. (1998) Mn-ores from Eastern Ligurian ophioltic sequences ("Diaspri di Monte Aple" Formation, Northern Apennines, Italy). Trends in Mineralogy, 2, 1-17.

Canil, D. (2002) Vanadium in peridotites, mantle redox and tectonic environments: Archean to present. Earth and Planetary Science Letters, 195, 75-90.

Černý, P., Chapman, R., Staně, J., Nová, M., Baadsgaard, H., Rieder, M., Ottolini, L., Kavalová, M., and Chapman, R. (1995). Geochemical and structural evolution of micas in the Rožná and Dobrá Voda pegmatites, Czech Republic. Mineralogy and Petrology, 55, 177-201.

Cesare, B., Cruciani, G., and Russo, U. (2003) Hydrogen deficiency in Ti-rich biotite from anatectic metapelites (El Joyazo, SE Spain): Crystal-chemical aspects and implications for high-temperature petrogenesis. American Mineralogist, 88, 583–595.

Chukanov, N.V., Mukhanova, A.A., Rastsvetaeva, R.K., Belakovsky, D.I., Möckel, S., Karimova, O.V., Britvin, S.N., and Krivovichev, S.V. (2011) Oxyphlogopite $K(Mg,Ti,Fe)_3[(Si,Al)_4O_{10}](O,F)_2$: A new mineral species of the mica group. Geology of Ore Deposits, 53, 583-590.

Civetta, L., Orsi, G., Scandone, P., and Pece, R. (1978). Eastwards migration of the Tuscan anatectic magmatism due to anticlockwise rotation of the Apennines. Nature, 276, 604–606.

Conticelli, S., Manetti, P., and Menichetti, S. (1992). Mineralogy, geochemistry and Sr-isotopes in orendites from South Tuscany, Italy: constraints on their genesis and evolution. European journal of mineralogy, 4, 1359-1375.

Conticelli, S., and Peccerillo, A., (1992). Petrology and geochemistry of potassic and ultrapotassic volcanism in central Italy: petrogenesis and inferences on the evolution of the mantle sources. Lithos, 28, 221–240.

Conticelli, S. (1998). The effect of crustal contamination on ultrapotassic magmas with lamproitic affinity: mineralogical, geochemical and isotope data from the Torre Alfina lavas and xenoliths, Central Italy. Chemical Geology, 149, 51-81.

Conticelli, S., Bortolotti, V., Principi, G., Laurenzi, M. A., D'Antonio, M., and Vaggelli, G. (2001). Petrology, mineralogy and geochemistry of a mafic dyke from Monte Castello, Elba Island, Italy. Ofioliti, 26, 249-261.

Conticelli, S., Carlson, R. W., Widom, E., and Serri, G. (2007). Chemical and isotopic composition (Os, Pb, Nd, and Sr) of Neogene to Quaternary calc-alkalic, shoshonitic, and ultrapotassic mafic rocks from the Italian peninsula: inferences on the nature of their mantle sources. Geological Society of America Special Papers, 418, 171-202.

Conticelli, S., Guarnieri, L., Farinelli, A., Mattei, M., Avanzinelli, R., Bianchini, G., Boari, E., Tommasini, S., Tiepolo, M., Prelevic, D., and Venturelli, G. (2009). Trace elements and Sr–Nd–Pb isotopes of K-rich, shoshonitic, and calc-alkaline magmatism of the Western Mediterranean Region: genesis of ultrapotassic to calc-alkaline magmatic associations in a post-collisional geodynamic setting. Lithos, 107, 68-92.

Conticelli, S., Laurenzi, M. A., Giordano, G., Mattei, M., Avanzinelli, R., Melluso, L., Tommasini, S., Boari, E., Cifelli, F., and Perini, G. (2010). Leucite-bearing (kamafugitic/leucititic) and-free (lamproitic) ultrapotassic rocks and

associated shoshonites from Italy: constraints on petrogenesis and geodynamics. Journal of the Virtual Explorer, 36(20).

Cortesogno, L., Lucchetti, G., and Penco, A.M. (1979) Le mineralizzazioni a manganese nei diaspri delle ofioliti liguri: mineralogia e genesi. Rendiconti della Società Italiana di Mineralogia e Petrologia, 35, 151-197.

Cruciani, G., and Zanazzi, P. F. (1994). Cation partitioning and substitution mechanisms in 1*M* phlogopite; a crystal chemical study. American Mineralogist, 79, 289-301.

Cruciani, G., Zanazzi, P.F., and Quartieri, S. (1995) Tetrahedral ferric iron in phlogopite; XANES and Mössbauer compared to single-crystal X-ray data. European Journal of Mineralogy, 7, 255–265.

Dal Piaz, G. V., and Ernst, W. G. (1978). Areal geology and petrology of eclogites and associated metabasites of the Piemonte Ophiolite Nappe, Breuil—St. Jacques area, Italian Western Alps. Tectonophysics, 51, 99-126.

Davies, G. R., Stolz, A. J., Mahotkin, I. L., Nowell, G. M., and Pearson, D. G. (2006). Trace element and Sr–Pb–Nd–Hf isotope evidence for ancient, fluid-dominated enrichment of the source of Aldan Shield lamproites. Journal of Petrology, 47, 1119-1146.

Deloule E., France-Lanord C. and Albarède F, 1991, D/H Analysis of Mineral by Ion Probe, in "Stable Isotope geochemistry: A Tribute to Samuel Epstein", Special Publication N°3 of the Geochemical Society V.3, 53-62. Shimizu

Derkowski, A., Drits, V. A., and McCarty, D. K. (2012). Nature of rehydroxylation in dioctahedral 2: 1 layer clay minerals. American Mineralogist, 97, 610-629.

Doblas, M., and Oyarzun, R. (1989). Neogene extensional collapse in the western Mediterranean (Betic-Rif Alpine orogenic belt): Implications for the genesis of the Gilbraltar Arc and magmatic activity. Geology, 17, 430-433.

Doglioni, C., Harabaglia, P., Merlini, S., Mongelli, F., Peccerillo, A., and Piromallo, C. (1999). Orogens and slabs vs. their direction of subduction. Earth-Science Reviews, 45, 167-208.

Du Bray, E. A. (1994). Compositions of micas in peraluminous granitoids of the eastern Arabian Shield. Contributions to Mineralogy and Petrology, 116, 381-397.

Duggen, S., Hoernle, K., van den Bogaard, P., and Harris, C. (2004). Magmatic evolution of the Alboran region: the role of subduction in forming the western Mediterranean and causing the Messinian Salinity Crisis. Earth and Planetary Science Letters, 218, 91-108.

Duggen, S., Hoernle, K., van den Bogaard, P., and Garbe-Schönberg, D. (2005). Post-collisional transition from subduction-to intraplate-type magmatism in the westernmost Mediterranean: evidence for continental-edge delamination of subcontinental lithosphere. Journal of Petrology. 46, 1155–1201.

Duggen, S., Hoernle, K., Klügel, A., Geldmacher, J., Thirlwall, M., Hauff, F., Lowry, D., and Oates, N. (2008). Geochemical zonation of the Miocene Alborán Basin volcanism (westernmost Mediterranean): geodynamic implications. Contributions to Mineralogy and Petrology, 156, 577-593.

Durovic, S. (1994). Classification of phyllosilicates according to the symmetry of their octahedral sheets. Ceramics, 38, 81

Dyar, M.D., Guidotti, C.V., Holdaway, M.J., and Colucci, M. (1993) Nonstoichiometric hydrogen contents in common rock-forming hydroxyl silicates. Geochimica and Cosmochimica Acta, 57, 2913–2918.

Dymek, R.F. (1983) Titanium, aluminum and interlayer cation substitutions in biotite from high-grade gneisses, West Greenland. American Mineralogist, 68, 880–899.

Edgar, A. D., and Arima, M. (1983). Conditions of phlogopite crystallization in ultrapotassic volcanic rocks. Mineralogical Magazine, 47, 11-19.

Edgar, A. D., and Charbonneau, H. E. (1991). Fluorine-bearing phases in lamproites. Mineralogy and Petrology, 44, 125-149.

Edgar, A. D., Charbonneau, H. E., and Mitchell, R. H. (1992). Phase relations of an armalcolite-phlogopite lamproite from Smoky Butte, Montana: applications to lamproite genesis. Journal of Petrology, 33, 505-520.

Edgar, A. D., Pizzolato, L. A., and Sheen, J. (1996). Fluorine in igneous rocks and minerals with emphasis on ultrapotassic mafic and ultramafic magmas and their mantle source regions. Mineralogical Magazine, 60, 243-258.

Eggleton, R. A., and Ashley, P. M. (1989). Norrishite, a new manganese mica, K (Mn (super 3+) 2 Li) Si 4 O 12, from the Hoskins Mine, New South Wales, Australia. American Mineralogist, 74(11-12), 1360-1367.

Feeley, T.C. and Sharp, Z.D. (1996) Chemical and hydrogen isotope evidence for in situ dehydrogenation of biotite in silicic magma chambers. Geology, 24, 1021–1024.

Feldstein, S.N., Lange, R.A., Vennemann, T., and O'Neil, J.R. (1996) Ferric-ferrous ratios, H2O contents and D/H ratios of phlogopite and biotite from lavas of different tectonic regimes. Contributions to Mineralogy and Petrology, 126, 51–66.

Ferraris, G., and Ivaldi, G. (2002). Structural features of micas. Reviews in mineralogy and geochemistry, 46, 117-153.

Foley, S. F., Venturelli, G., Green, D. H., and Toscani, L. (1987). The ultrapotassic rocks: characteristics, classification, and constraints for petrogenetic models. Earth-Science Reviews, 24, 81-134.

Foley, S. F. (1989). Experimental constraints on phlogopite chemistry in lamproites: 1. The effect of water activity and oxygen fugacity. European Journal of Mineralogy, 1, 411-426.

Foley, S. F., and Venturelli, G. (1989). High K_2O rocks with high MgO, high SiO_2 affinities. Boninites. Unwin Hyman, London, 72-88.

Foley, S. F. (1990). Experimental constraints on phlogopite chemistry in lamproites: 2. Effect of pressure-temperature variations. European Journal of Mineralogy, 2, 327-342.

Foley, S.F., (1992). Vein-plus-wall-rock melting mechanisms in the lithosphere and the origin of potassic alkaline magmas. Lithos, 28, 435–453.

Foley, S.F., (1993). An experimental study of olivine lamproite—first results from the diamond stability field. Geochimica et Cosmochimica Acta, 57, 483–489.

Foley, S.F., (1994). Geochemische und experimentelle Untersuchungen zur genese der kalireichen Magmatite. Neues Jahrbuch fur Mineraleralogie Abathlung, 167, 1–55.

Foster, M. D. (1960). Interpretation of the composition of trioctahedral micas. Geological Survey Professional Paper, Volume 354.

Foord, E. E., Černý, P., Jackson, L. L., Sherman, D. M., and Eby, R. K. (1995). Mineralogical and geochemical evolution of micas from miarolitic pegmatites of the anorogenic Pikes Peak batholith, Colorado. Mineralogy and Petrology, 55, 1-26.

Fritschle, T., Prelević, D., Foley, S.F., and Jacob, D. E. (2013) Petrological characterization of the mantle source of Mediterranean lamproites: Indications from major and trace elements of phlogopite. Chemical Geology, 353, 267-279.

Frost, R.L., Erickson, K.L., Weier, M.L., and Carmody, O. (2005) Raman and infrared spectroscopy of selected vanadates. Spectrochimica Acta, Part A: Molecular and Biomolecular Spectroscopy, 61, 829-834.

Gasparon, M., Rosenbaum, G., Wijbrans, J., and Manetti, P. (2009). The transition from subduction arc to slab tearing: Evidence from Capraia Island, northern Tyrrhenian Sea. Journal of Geodynamics, 47, 30-38.

Gianfagna, A., Scordari, F., Mazziotti-Tagliani, S., Ventruti, G., and Ottolini, L. (2007). Fluorophlogopite from Biancavilla (Mt. Etna, Sicily, Italy): Crystal structure and crystal chemistry of a new F-dominant analog of phlogopite. American Mineralogist, 92, 1601-1609.

Giese, R. F. (1979). Hydroxyl orientations in 2: 1 phyllosilicates. Clays and Clay Minerals, 27, 213-223.

Giese, R.F., Jr (1984). Electrostatic energy models of micas. In Mineralogical Society of America Reviews in Mineralogy, 13, 105-144.

Giuliani, G., Ohnenstetter, D., Palhol, F., Feneyrol, J., Boutroy, E., De Boissezon, H. and Lhomme, T. (2008) Karelianite and vanadian phlogopite from the Merelani Hills gem zoisite deposits, Tanzania. Canadian Mineralogist, 46, 1183-1194.

Griffen, D. T., and Ribbe, P. H. (1979). Distortions in the tetrahedral oxyanions of crystalline substances. Neues Jahrbuch für Mineralogie. Abhandlungen, 137, 54-73.

Guggenheim, S., and Bailey, S. W. (1977). The refinement of zinnwaldite-1*M* in subgroup symmetry. American Mineralogist, 62, 1158-1167.

Guggenheim, S., Schulze, W.A., Harris, G.A. and Lin, J.-C. (1983) Concentric layer silicates: An optical second harmonic generation, chemical and X-ray study. Clays and Clay Minerals, 31, 251-260.

Guggenheim, S., Chang, Y.-H., and Koster van Groos, A.F. (1987) Muscovite dehydroxylation: High-temperature studies. American Mineralogist, 72, 537-550.

Guggenheim, S. (1990). The dynamics of thermal decomposition in aluminous dioctahedral 2: 1 layer silicates: A crystal chemical model. In Proceedings of the 9th International Clay Conference, pp. 99-107.

Guidotti, C. V. (1984). Micas in metamorphic rocks. Reviews in Mineralogy and Geochemistry, 13, 357-467.

Guo, Z., Wilson, M., Liu, J., and Mao, Q., (2006). Post-collisional, potassic and ultrapotassic magmatism of the northern Tibetan plateau: constraints on characteristics of the mantle source, geodynamic setting and uplift mechanisms. Journal of Petrology, 47, 1177–1220.

Guo, Z., Wilson, M., Zhang, M., Cheng, Z., and Zhang, L., (2013). Post-collisional, K-rich mafic magmatism in south Tibet: constraints on Indian slab-to-wedge transport processes and plateau uplift. Contributions to Mineralogy and Petrology 165, 1311–1340.

Guo, Z., Wilson, M., Zhang, L., Zhang, M., Cheng, Z., and Liu, J. (2014). The role of subduction channel mélanges and convergent subduction systems in the petrogenesis of post-collisional K-rich mafic magmatism in NW Tibet. Lithos, 198, 184-201.

Gutscher, M. A., Malod, J., Rehault, J. P., Contrucci, I., Klingelhoefer, F., Mendes-Victor, L., and Spakman, W. (2002). Evidence for active subduction beneath Gibraltar. Geology, 30, 1071-1074.

Güven, N. (1971) The crystal structure of *2M*$_1$ phengite and *2M*$_1$ muscovite. Zeitschrift für Kristallographie, 134, 195-212.

Harada, K., Honda, M., Nagashima, K., and Kanisawa, S. (1976). Masutomilite, manganese analogue of zinnwaldite, with special reference to masutomilite–lepidolite–zinnwaldite series. Mineralogical Journal, 8, 95-109.

Hawthorne, F.C., Oberti, R., Cannillo, E., Sardone, N., Zanetti, A., Grice, J.D., and Ashley, P.M. (1995) A new anhydrous amphibole from Hoskins mine, Grenfell, New South Wales, Australia: Description and crystal structure of ungarettiite, $NaNa_2(Mn_2^{2+}Mn_3^{3+})Si_8O_{22}O_2$. American Mineralogist, 80, 165-172.

Hazen, R. M., and Wones, D. R. (1972). Effect of cation substitutions on physical properties of trioctahedral micas. American Mineralogist, 57, 103.

Hazen, R.M., and Burnham, C.W. (1973) The crystal structure of one layer phlogopite and annite. American Mineralogist, 58, 889-900.

Holland, T. J. B., and Redfern, S. A. T. (1997). UNITCELL: a nonlinear least-squares program for cell-parameter refinement and implementing regression and deletion diagnostics. Journal of Applied Crystallography, 30, 84-84.

Ibers, J.A., and Hamilton, W.C. (editors) (1974) International Tables for X-ray Crystallography, vol. IV. Kynock Press, Birmingham, UK.

Ishida, K., Hawthorne, F. C., and Hirowatari, F. (2004). Shirozulite, $KMn^{2+}{}_3(Si_3Al)O_{10}(OH)_2$, a new manganese-dominant trioctahedral mica: Description and crystal structure. American Mineralogist, 89, 232-238.

Jaques, A.L., Lewis, J.D., and Smith, C.B., (1986). The kimberlites and lamproites of Western Australia. Western Australia Geological Survey Bulletin, 132, 269 pp.

Koch, S., and Breu, J. (2013) Transition metals in micas: synthesis and characterization of Co-rich Cs-tainiolite. European Journal of Mineralogy, 25, 487-494.

Kogarko, L.N., Uvarova, Yu.A., Sokolova, E., Hawthorne, F.C., Ottolini, L., and Grice J.D. (2005) Oxykinoshitalite, a new species of mica from Fernando de Noronha Island, Pernambuco, Brazil; occurrence and crystal structure. Canadian Mineralogist, 43, 1501-1510.

Kogure, T. and Drits, V.A. (2010) Structural change in celadonite and cis-vacant illite by electron radiation in TEM. Clays and Clay Minerals, 58, 522– 531.

Kolb, U., Mugnaioli, E., and Gorelik, T. E. (2011). Automated electron diffraction tomography–a new tool for nano crystal structure analysis. Crystal Research and Technology, 46, 542-554.

Kunz, M., Armbruster, T., Lager, G. A., Schultz, A. J., Goyette, R. J., Lottermoser, W., and Amthauer, G. (1991). Fe, Ti Ordering and Octahedral Distortions in Acentric Neptunite: temperature dependent X-ray and neutron structure refinements and Mössbauer spectroscopy. Physics and Chemistry of Minerals, 18, 199-213.

Lacalamita, M. (2009) Studio chimico-strutturale dei siti anionico e cationici in miche triottaedriche a temperatura ambiente e non, 228 p. Ph.D. thesis, University of Bari, Italy.

Lacalamita, M., Schingaro, E., Scordari, F., Ventruti, G., Fabbrizio, A., and Pedrazzi, G.,(2011). Substitution mechanisms and implications for the estimate of water fugacity for Ti-rich phlogopite from Mt. Vulture (Potenza, Italy). American Mineralogist, 96, 1381–1391.

Lagarec, K. and Rancourt, D.G. (1997) Extended Voigt-based analytic lineshape method for determining N-dimensional correlated hyperfine parameter distributions in Mössbauer spectroscopy. Nuclear Instruments and Methods in Physics Research B, 129, 266–280.

Lagarec, K. and Rancourt, D.G. (1998) RECOIL, Mössbauer Spectral Analysis Software for Windows (version 1.0). Department of Physics, University of Ottawa, Canada.

Lahti, S. I., and Saikkonen, R. (1985). Bityite 2M_1 from Eräjärvi compared with related Li-Be brittle micas. Bulletin of the Geological Society of Finland, 57, 207-215.

Laurora, A., Brigatti, M.F., Mottana, A., Malferrari, D., and Caprilli, E. (2007) Crystal chemistry of trioctahedral micas in alcaline and subalkaline volcanic rocks: A case study from Mt. Sassetto (Tolfa district, Latium, central Italy). American Mineralogist, 92, 468–480.

Laurora, A., Malferrari, D., Brigatti, M. F., Mottana, A., Caprilli, E., Giordano, G., and Funiciello, R. (2009). Crystal chemistry of trioctahedral micas in the top sequences of the Colli Albani volcano, Roman Region, central Italy. Lithos, 113(3), 507-520.

Lee, J. H., and Guggenheim, S. (1981). Single crystal X-ray refinement of pyrophyllite-1Tc. American Mineralogist, 66, 350-357.

Lepore, G. O., Bindi, L., Zanetti, A., Ciriotti, M., Medenbach, O., and Bonazzi, P. (2015) Balestraite, $KLi_2VSi4O_{10}O_2$, the first member of the mica group with octahedral V^{5+}. American Mineralogist, 100, 608-614.

Levinson, A. A. (1953). Studies in the mica group; relationship between polymorphism and composition in the muscovite-lepidolite series. American Mineralogist, 38, 88-107.

Lin, J. C., and Guggenheim, S. (1983). The crystal structure of a Li, Be-rich brittle mica; a dioctahedral-trioctahedral intermediate. American Mineralogist, 68, 130-142.

Lucchetti, G., Cortesogno, L., and Palenzona, A. (1988) Low-temperature metamorphic mineral assemblages in Mn-Fe ores from Cerchiara mine (northern Appennine, Italy). Neues Jahrbuch für Mineralogie. Monatshefte, 1988, 367-383.

Mariychuk, R., Baumgartner, A., Wagner, F.E., Lerf, A., Dubbe, A., and Breu, J. (2007) Synthesis, structure and electric conductivity of ferrous tainiolite and its oxidative conversion into coarse-grained swellable smectite. Chemistry of materials, 19, 5377-5387.

Martins, T., Roda-Robles,E., Lima, A., and de Parseval, P. (2012). Geochemistry and evolution of micas in the Barroso–Alvão pegmatite field, Northern Portugal. The Canadian Mineralogist, 50, 1117-1129.

Mascle, G. H., Tricart, P., Torelli, L., Bouillin, J. P., Rolfo, F., Lapierre, H., Monié, P., Depardon, S., Mascle, J., and Peis, D. (2001). Evolution of the Sardinia Channel (Western Mediterranean): new constraints from a diving survey on Cornacya seamount off SE Sardinia. Marine Geology, 179, 179-201.

Matarrese, S., Schingaro, E., Scordari, F., Stoppa, F., Rosatelli, G., Pedrazzi, G., and Ottolini, L. (2008) Crystal chemistry of phlogopite from Vulture-S.Michele Subsynthem volcanic rocks (Mt. Vulture, Italy) and volcanological implications. American Mineralogist, 93, 426–437.

Mattei, M., Riggs, N. R., Giordano, G., Guarnieri, L., Cifelli, F., Soriano, C. C., Jicha, B., Jasim, A., Marchionni, S., Franciosi, L., Tommasini, S, Porreca, M., and Conticelli, S. (2014). Geochronology, Geochemistry and Geodynamics of the Cabo de Gata volcanic zone, Southeastern Spain. Italian Journal of Geosciences, 133, 341-361.

McCauley, J.W., and Newnham, R.E. (1971). Origin and prediction of ditrigonal distortions in micas. American Mineralogist, 56, 1626-1637 .

McCauley, J.W., Newnham, R.E., and Gibbs, G.V. (1973) Crystal structure analysis of synthetic fluorophlogopite. American Mineralogist, 58, 249-254.

Mercier, P. H., Evans, R. J., and Rancourt, D. G. (2005). Geometric crystal chemical models for structural analysis of micas and their stacking polytypes. American Mineralogist, 90, 382-398.

Mesto, E., Schingaro, E., Scordari, F., and Ottolini, L. (2006) An electron microprobe analysis, secondary ion mass spectrometry, and single crystal X-ray diffraction study of phlogopites from Mt. Vulture, Potenza, Italy: Consideration of cation partitioning. American Mineralogist, 91, 182–190.

Miller, C., Zanetti, A., Thöni, M., and Konzett, J. (2007) Trace element mineral chemistry of the type locality (Koralpe, Saualpe) and Pohorje eclogites (Eastern Alps): implications for behaviour of fluid-mobile elements in a continental subduction zone, geochronology and geothermometry. Chemical Geology, 239, 96-123.

Mirnejad, H., and Bell, K. (2006). Origin and source evolution of the Leucite Hills lamproites: evidence from Sr–Nd–Pb–O isotopic compositions. Journal of Petrology, 47(12), 2463-2489.

Mitchell, R. H., and Bergman, S. C. (1991). Petrology of lamproites. Plenum Press, New York, 450 pp.

Monier, G., and Robert, J. L. (1986). Evolution of the miscibility gap between muscovite and biotite solid solutions with increasing lithium content: an experimental study in the system K_2O– Li_2O– MgO– FeO– Al_2O_3– SiO_2– H_2O– HF. Mineralogical Magazine, 50, 641-651.

Murphy, D.T., Collerson, K.D., and Kamber, B.S.,(2002). Lamproites from Gaussberg, Antarctica: possible transition zone melts of Archaean subducted sediments. Journal of Petrology 43, 981–1001.

Nazzareni, S., Comodi, P., Bindi, L., Safonov, O. G., Litvin, Y. A., and Perchuk, L. L. (2008). Synthetic hypersilicic Cl-bearing mica in the phlogopite-celadonite join: A multimethodical characterization of the missing link between di-and tri-octahedral micas at high pressures. American Mineralogist, 93, 1429-1436.

Nelson, D.R., 1992. Isotopic characteristics of potassic rocks: evidence for the involvement of subducted sediments in magma genesis. Lithos, 28, 403–420.

Nespolo, M., and Ďurovič, S. (2002). Crystallographic basis of polytypism and twinning in micas. Reviews in mineralogy and geochemistry, 46, 155-279.

Oberti, R., Ungaretti, L., Tlili, A., Smith, D.C., and Robert, J.L. (1993) The crystal structure of preiswerkite. American Mineralogist, 78, 1290–1298.

Ohta, T., Takeda, H., and Takeuchi, Y. (1982). Mica polytypism; similarities in the crystal structures of coexisting 1*M* and $2M_1$ oxybiotite. American Mineralogist, 67, 298-310.

Ottolini, L. P., Schingaro, E., Scordari, F., Mesto, E., and Lacalamita, M. (2010, February). The role of SIMS in the investigation of the complex crystal chemistry of mica minerals. In IOP Conference Series: Materials Science and Engineering (Vol. 7, No. 1, p. 012023). IOP Publishing.

Owen, J. P. (2008). Geochemistry of lamprophyres from the Western Alps, Italy: implications for the origin of an enriched isotopic component in the Italian mantle. Contributions to Mineralogy and Petrology, 155, 341-362.

Oxford Diffraction (2006) *CrysAlis* RED (Version 1.171.31.2) and ABSPACK in *CrysAlis* RED. Oxford Diffraction Ltd, Abingdon, Oxfordshire, England.

Oyarzun, R., Marquez, A., Ortega, L., and Lunar, R. (1995). A late Miocene metallogenic province in southeast Spain: atypical Andean-type processes on a smaller scale. Transactions of the Institution of Mining and Metallurgy. Section B. Applied Earth Science, 104.

Pan, Y., and Fleet, M. E. (1992) Mineral chemistry and geochemistry of vanadian silicates in the Hemlo gold deposit, Ontario, Canada. Contributions to Mineralogy and Petrology, 109, 511-525.

Parsons, S., and Flack, H. (2004) Precise absolute-structure determination in light-atom crystals. Acta Crystallographica, A60, 61-61.

Peccerillo, A. (1985). Roman comagmatic province (central Italy): evidence for subduction-related magma genesis. Geology, 13(2), 103-106.

Peccerillo, A., Conticelli, S., and Manetti, P. (1987). Petrological characteristics and the genesis of the recent magmatism of southern Tuscany and northern Latium. Periodico di Mineralogia, 56, 157-172.

Peccerillo, A., Poli, G., and Serri, G. (1988). Petrogenesis of orenditic and kamafugitic rocks from Central Italy. Canadian Mineralogist, 26, 45-65.

Peccerillo, A. (1999). Multiple mantle metasomatism in central-southern Italy: geochemical effects, timing and geodynamic implications. Geology, 27, 315–318.

Peccerillo, A. (2003). Plio-Quaternary magmatism in Italy. Episodes 26, 222–226.

Peccerillo, A. (2005). Plio-quaternary volcanism in Italy (p. 365). Springer-Verlag Berlin Heidelberg.

Peccerillo, A., and Martinotti, G. (2006). The Western Mediterranean lamproitic magmatism: origin and geodynamic significance. Terra Nova, 18, 109-117.

Poli, G., and Peccerillo, A. (2003). Lamproitic rocks from the Tuscan Magmatic Province. Periodico di Mineralogia, 72, 225-231.

Prelević, D., and Foley, S. F. (2007). Accretion of arc-oceanic lithospheric mantle in the Mediterranean: evidence from extremely high-Mg olivines and Cr-rich spinel inclusions in lamproites. Earth and Planetary Science Letters, 256, 120-135.

Prelević, D., Foley, S. F., and Cvetković, V. (2007). A review of petrogenesis of Mediterranean Tertiary lamproites: a perspective from the Serbian ultrapotassic province. Geological Society of America Special Papers, 418, 113-129.

Rancourt, D.G. and Ping, J.Y. (1991) Voigt-based methods for arbitrary-shape static hyperfine parameter distributions in Mössbauer spectroscopy. Nuclear Instruments and Methods in Physics Research B, 58, 85–97.

Rancourt, D.G., Dang, M.-Z., and Lalonde, A.E. (1992) Mössbauer spectroscopy of tetrahedral Fe3+ in trioctahedral micas. American Mineralogist, 77, 34–43.

Redhammer, G. J., and Roth, G. (2002). Single-crystal structure refinements and crystal chemistry of synthetic trioctahedral micas $KM_3(Al^{3+}, Si^{4+})_4O_{10}(OH)_2$, where M= Ni^{2+}, Mg^{2+}, Co^{2+}, Fe^{2+}, or Al^{2+}. American Mineralogist, 87, 1464-1476.

Rieder, M., Hybler, J., Smrcok, L., and Weiss, Z. (1996). Refinement of the crystal structure of zinnwaldite $2M_1$. European Journal of Mineralogy, 8, 1241-1248.

Righter, K., Dyar, M.D., Delaney, J.S., Vennemann, T.W., Hervig, R.L., and King, P.L. (2002) Correlation of octahedral cations with OH^-, O^{2-}, and F^- in biotite from volcanic rocks and xenoliths. American Mineralogist, 87, 142–153.

Robert, J.L. (1976) Titanium solubility in synthetic phlogopite solid solutions. Chemical Geology, 17, 213–227.

Robert, J.-L. and Maury, R.C. (1979) Natural occurrence of a (Fe, Mn, Mg) tetrasilicic potassium mica. Contributions to Mineralogy and Petrology, 68, 117-123.

Robert, J. L., Volfinger, M., Barrandon, J. N., and Basutçu, M. (1983). Lithium in the interlayer space of synthetic trioctahedral micas. Chemical geology, 40, 337-351.

Robinson, K., Gibbs, G. V., and Ribbe, P. H. (1971). Quadratic elongation: a quantitative measure of distortion in coordination polyhedra. Science, 172(3983), 567-570.

Roda-Robles, E., Pesquera, A., Gil-Crespo, P. P., Torres-Ruiz, J., and De Parseval, P. (2006). Mineralogy and geochemistry of micas from the Pinilla de Fermoselle pegmatite (Zamora, Spain). European journal of mineralogy, 18, 369-377.

Royden, L. L., and Karner, G. D. (1984). Flexure of lithosphere beneath Apennine and Carpathian foredeep basins: evidence for an insufficient topographic load. American Association of Petroleum Geologists (AAPG) Bulletin, 68, 704-712.

Sassi, R., Cruciani, G., Mazzoli, C., Nodari, L., and Craven, J. (2008). Multiple titanium substitutions in biotites from high-grade metapelitic xenoliths (Euganean Hills, Italy): Complete crystal chemistry and appraisal of petrologic control. American Mineralogist, 93, 339-350.

Sato, K., (1997). Melting experiments on a synthetic olivine lamproite composition up to 8 GPa; implication to its petrogenesis. Journal of Geophysical Research, 102 (B7),14751–14764.

Savitsky, A., and Golay, M. J. (1964). Smoothing and differentiation of data by simplified least squares procedures. Analytical Chemistry, 36, 1627-1639.

Schindler, M., Hawthorne, F.C., and Baur, W.H. (2000) Crystal chemical aspects of vanadium: polyhedral geometries, characteristic bond valences, and polymerization of (VO_n) polyhedral. Chemistry of Materials, 12, 1248-1259.

Schingaro, E., Scordari, F., and Ventruti, G. (2001). Trioctahedral micas-1*M* from Mt. Vulture (Italy) Structural disorder and crystal chemistry. European Journal of Mineralogy, 13, 1057-1069.

Schingaro, E., Mesto, E., Scordari, F., Brigatti, M.F., and Pedrazzi, G. (2005) Cation site partitioning in Ti-rich micas from Black Hill (Australia): A multi-technical approach. Clays and Clay Minerals, 53, 179–189.

Schingaro, E., Scordari, F., Matarrese, S., Mesto, E., Stoppa, F., Rosatelli, G., and Pedrazzi, G. (2007) Phlogopite from the Ventaruolo subsynthem volcanics (Mt Vulture, Italy): a multi-method study. Mineralogical Magazine, 71, 519–537.

Schingaro, E., Lacalamita, M., Scordari, F., Brigatti, M.F. and Pedrazzi, G. (2011) Crystal chemistry of Ti-rich fluorophlogopite from Presidente Olegario, Alto Paranaíba igneous province, Brazil. American Mineralogist, 96, 732-743.

Schingaro, E., Kullerud, K., Lacalamita, M., Mesto, E., Scordari, F., Zozulya, D., Erambert, M. and Ravna, E. J. (2014). Yangzhumingite and phlogopite from the Kvaløya lamproite (North Norway): Structure, composition and origin. Lithos, 210, 1-13.

Scordari, F., Ventruti, G., Sabato, A., Bellatreccia, F., Della Ventura, G., and Pedrazzi, G. (2006) Ti-rich phlogopite from Mt. Vulture (Potenza, Italy) investigated by a multianalytical approach: substitutional mechanisms and orientation of the OH dipoles. European Journal of Mineralogy, 18, 379–391.

Scordari, F., Schingaro, E., Ventruti, G., Lacalamita, M., and Ottolini, L. (2008) Red micas from basal ignimbrites of Mt. Vulture (Italy): interlayer content appraisal by a multi-methodic approach. Physics and Chemistry of Minerals, 35, 163–174.

Scordari, F., Dyar, M.D., Schingaro, E., Lacalamita, M., and Ottolini, L. (2010) XRD, micro-XANES, EMPA, and SIMS investigation on phlogopite single crystals from Mt. Vulture (Italy). American Mineralogist, 95, 1657–1670.

Scordari F, Schingaro E, Lacalamita M, Mesto E (2012a) Crystal chemistry of trioctahedral micas-2M_1 from Bunyaruguru (SW Uganda) kamafugite. American Mineralogist, 97, 430–439.

Scordari, F., Schingaro, E., Mesto, E., and Lacalamita, M. (2012b). 2M_1-phlogopite from Black Hills (South Australia): The first case of configurational polytype in micas. American Mineralogist, 97, 2016-2023.

Scordari, F., Schingaro, E., Ventruti, G., Nicotra, E., Viccaro, M., and Tagliani, S. M. (2013). Fluorophlogopite from Piano delle Concazze (Mt. Etna, Italy): Crystal chemistry and implications for the crystallization conditions. American Mineralogist, 98, 1017-1025.

Shannon, R.D. (1976) Revised effective ionic radii and systematic studies of interatomic distances in halides and chalcogenides. Acta Crystallographica, A32, 751-767.

Sheldrick, G.M. (2008) A short history of SHELX. Acta Crystallographica, A64, 112-122.

Slade, P.G., Schultz, P.K., and Dean, C. (1987) Refinement of the ephesite structure in $C1$ symmetry. Neues Jahrbuch für Mineralogie Monatshefte, 6, 275–287.

Smith, J. V., and Yoder, H. S. (1956). Experimental and theoretical studies of the mica polymorphs. Mineralogical Magazine, 31, 209-235.

Stevens, G., Clemens, J.C., and Droop, G.T.R. (1997) Melt production during granulite-facies anatexis: experimental data from "primitive" metasedimentary protoliths. Contributions to Mineralogy and Petrology, 128, 352–370.

Swanson, T. H., and Bailey, S. W. (1981). Redetermination of the lepidolite-2M_1 structure. Clays and Clay Minerals, 29, 81.

Takeda, H., and Burnham, C.W. (1969) Fluor-polylithionite: a lithium mica with nearly hexagonal $(Si_2O_5)^{2-}$ ring. Mineralogical Journal, 6, 102-109.

Takeda, H. and Ross, M. (1975). Mica polytypism: Dissimilarities in the crystal structures of coexisting 1M and 2M_1 biotite. American Mineralogist, 60, 1030–1040.

Tiepolo, M., Zanetti, A., and Vannucci, R. (2005) Determination of Li, Be and B at trace levels by LA-ICP-MS. Geostandards and Geoanalytical Research, 29, 211-224.

Tischendorf, G., Förster, H. J., Gottesmann, B., and Rieder, M. (2007). True and brittle micas: composition and solid-solution series. Mineralogical Magazine, 71, 285-320.

Tommasini, S., Avanzinelli, R., and Conticelli, S. (2011). The Th/La and Sm/La conundrum of the Tethyan realm lamproites. Earth and Planetary Science Letters, 301, 469-478.

Toraya, H., Iwai, S., Marumo, F., and Hirao, M. (1977) The crystal structure of taeniolite, $KLiMg_2Si_4O_{10}F_2$. Zeitschrift für Kristallographie, 146, 73-83.

Toraya, H. (1981). Distortions of octahedra and octahedral sheets in 1*M* micas and the relation to their stability. Zeitschrift für Kristallographie-Crystalline Materials, 157, 173-190.

Tracy, R.J. and Beard, J.S. (2003) Manganoan kinoshitalite in Mn-rich marble and skarn from Virginia. American Mineralogist, 88, 740-747.

Trønnes, R. G., Edgar, A. D., and Arima, M. (1985). A high pressure-high temperature study of TiO_2 solubility in Mg-rich phlogopite: implications to phlogopite chemistry. Geochimica et Cosmochimica Acta, 49, 2323-2329.

Turner, S. P., Platt, J. P., George, R. M. M., Kelley, S. P., Pearson, D. G., and Nowell, G. M. (1999). Magmatism associated with orogenic collapse of the Betic–Alboran domain, SE Spain. Journal of Petrology, 40, 1011-1036.

Tyrna, P.L., and Guggenheim, S. (1991) The crystal structure of norrishite, $KLiMn^{3+}{}_2Si_4O_{12}$: an oxygen-rich mica. American Mineralogist, 76, 266-271.

Van Lichtervelde, M., Grégoire, M., Linnen, R. L., Béziat, D., and Salvi, S. (2008). Trace element geochemistry by laser ablation ICP-MS of micas associated with Ta mineralization in the Tanco pegmatite, Manitoba, Canada. Contributions to Mineralogy and Petrology, 155, 791-806.

Ventruti, G., Zema, M., Scordari, F., and Pedrazzi, G. (2008) Thermal behavior of a Ti-rich phlogopite from Mt. Vulture (Potenza, Italy): An in situ X-ray single-crystal diffraction study. American Mineralogist, 93, 632–643.

Venturelli, G., Thorpe, R.S., Dal Piaz, G.V., Del Moro, A. and Potts, P.J., (1984a). Petrogenesis of calc-alkaline, shoshonitic and associated ultrapotassic Oligocene volcanic rocks from Northwestern Alps, Italy. Contributions to Mineralogy and Petrology, 86, 209–220.

Venturelli, G., Capedri, S., Di Battistini, G., Crawford, A.J., Kogarko, L.N. and Celestini, S., (1984b). The ultrapotassic rocks from southeastern Spain. Lithos, 17, 37–54.

Venturelli, G., Capedri, S., Barbieri, M., Toscani, L., Salvioli Mariani, E., and Zerbi, M. (1991). The Jumilla lamproite revisited: a petrological oddity. European Journal of Mineralogy, 123-146.

Vieira, R., Roda-Robles, E., Pesquera, A., and Lima, A. (2011). Chemical variation and significance of micas from the Fregeneda-Almendra pegmatitic field (Central-Iberian Zone, Spain and Portugal). American Mineralogist, 96, 637-645.

Virgo, D. and Popp, R.K. (2000) Hydrogen deficiency in mantle-derived phlogopites. American Mineralogist, 85, 753–759.

Vollmer, R. (1989). On the origin of the Italian potassic magmas: 1. A discussion contribution. Chemical Geology, 74, 229–239.

Wagner, C., Velde, D., (1986). The mineralogy of K-richterite bearing lamproite. American Mineralogist, 71, 17–37.

Wardle, R., and Brindley, G. W. (1972). Crystal-Structures of Pyrophyllite, 1*Tc*, and of its dehydroxylate. American Mineralogist, 57, 732.

Waters, D.J. and Charnley, N.R. (2002) Local equilibrium in polymetamorphic gneiss and the titanium substitution in biotite. American Mineralogist, 87, 383–396.

Weiss, Z., Rieder, M., and Chmielova, M. (1992). Deformation of coordination polyhedra and their sheets in phyllosilicates. European Journal of Mineralogy, 4, 665-682.

Wilson, A.J.C., and Prince, E., Eds. (1999) *International Tables for X-ray Crystallography*,

Zanetti, A., Tiepolo, M., Oberti, R., and Vannucci, R. (2004) Trace-element partitioning in olivine: modelling of a complete data set from a synthetic hydrous basanite melt. Lithos, 75, 39-54.

Zema, M., Ventruti, G., Lacalamita, M., and Scordari, F. (2010). Kinetics of Fe-oxidation/deprotonation process in Fe-rich phlogopite under isothermal conditions. American Mineralogist, 95, 1458-1466.

8 Acknowledgments

First of all I would like to thank Paola Bonazzi for the support she was always able to give me (sometimes even without knowing it) and for everything she taught me.

A big "thank you" to Luca Bindi, who was always ready to help and encourage me.

I thank Sandro Conticelli not only for providing the most part of the samples used in this study but also for his help in the review of the manuscript.

Thanks to Marco Ciriotti (AMI) for his kind and helpful collaboration in the characterization of new minerals.

Many thanks are also due to the people who collaborated with me in performing analyses with different techniques: Alberto Zanetti (CNR-IGG of Pavia), for his help with LA-ICP-MS, Giuseppe Pedrazzi (University of Parma) for Mössbauer spectroscopy, Cecilia Viti and Enrico Mugnaioli (University of Siena) for TEM investigations, Francesco Di Benedetto (University of Florence) for the EPR measurements, Andrea Risplendente (University of Milan) and Andrea Orlando (CNR-IGG of Florence) for their help with microprobe analyses.

Thanks to Tiziana Boffa Ballaran for having welcomed me in the Bayerisches Geoinstitut in Bayreuth and for having introduced me to the charming world of high-pressure crystallography.

Thanks also to Samuele Ciattini and the people at CRIST (University of Florence) for making a pleasure to work in the lab.

Thanks to Corrado Balestra, Fabrizio Castellaro and Massimo Batoni, for providing the interesting samples from Cerchiara mine, and to Roberto Bracco and Luca Ceccantini for the photos of the samples.

A warm "thank you" to my friends in the Department of Earth Science: Francesca, Matteo, Jacopo and, especially, Valentina, for being always able to stand me and for the fundamental psychological support.